

Steady and unsteady channel flow,
numerical models with applications
to the recorder flute and vocal folds modelling

Koen Goorman

August 15, 2000

Abstract

In this report we present a steady and an unsteady two-dimensional, laminar, incompressible channel flow model. The models are derived from the Navier Stokes equations on the basis of boundary layer theory. We also present the numerical method used for solution of these models by means of finite differences. Their accuracy has been tested by solving these flow models in particular geometries for which analytical or approximate solutions are known. In these cases, the models show rather good results with respect to the theoretical solutions.

Results of the steady flow model have also been compared with results of direct numerical simulation of the complete Navier Stokes equations, by a commercial code FLUENT, applied on a straight channel, which expands discontinuously. We find a discrepancy of 3% in the results for the velocity field.

The steady flow model has been used for simulation of the flow through a flue channel in the mouthpiece of a recorder flute. The results have been compared with experiments. The discrepancies are about 10%. They could at least partially be explained by measurement errors, and by effects of turbulence. We also give suggestions for methods which possibly will improve results.

The unsteady flow model has been used for simulation of the flow through the human glottis, in a coupled simulation of the flow and the vibration of the vocal folds. The vocal folds are described with a simple single mass-spring model. This model is solved numerically with an unconditionally stable method. Simulations have been carried out with a constant volume flux and a constant pressure drop over the channel.

The behaviour of the hydrodynamic force on the vocal folds has been examined qualitatively, for both constant volume flux and constant pressure drop. In case of volume flux imposition we observe a transfer of energy from the fluid to the vocal folds. In case of pressure drop imposition we observe transfer of energy in both directions, depending on the value of the pressure drop. The results are discussed qualitatively in reference with other vocal folds models and suggestions are made for future work.

Vocal fold oscillation is observed in these simulations, even with one mechanical degree of freedom. In contrast to other models which state that vocal folds oscillation requires at least two mechanical degrees of freedom (two masses and two springs).

Contents

1	General introduction	4
1.1	The flute	4
1.2	The larynx	5
1.3	Scope of the work	7
I	Steady channel flow	8
2	The flow model	10
2.1	Channel flow	11
2.1.1	Scaling quantities	12
2.1.2	Reduced Navier Stokes system	13
2.1.3	'Dynamic' scaling	14
2.1.4	Solutions	15
2.2	Plane jet	19
2.2.1	Solutions	20
3	Numerical method	22
3.1	Channel flow	23
3.1.1	Discrete RNS-p(x) equations	23
3.1.2	Solution	24
3.1.3	Accuracy and stability	26
3.2	Plane jet	26
3.2.1	Discretisation	26
3.2.2	Solution	27
3.2.3	Accuracy and stability	28
3.3	The coupled simulation	29
3.3.1	Comparison with FLUENT	29

4	Application: the flue channel	31
4.1	Experimental results	31
4.2	Applied geometry	32
4.3	Determination Reynolds-number	33
4.4	Comparison experimental and simulation results	33
5	Discussion	37
II	Unsteady channel flow	40
6	The model	42
6.1	Unsteady channel flow	42
6.1.1	'Dynamic' scaling	43
6.1.2	Solutions	44
6.2	Wall motion	46
7	Numerical method	48
7.1	Channel flow	48
7.1.1	Solution	49
7.1.2	Accuracy and stability	51
7.2	Wall motion	51
7.2.1	Discrete equations	52
7.2.2	Solution	52
8	Application: vocal folds	54
8.1	The applied geometry	55
8.2	Imposed flux	55
8.3	Imposed pressure difference	57
9	Discussion	60
10	General conclusions	62
A	The von Kármán equation	65
B	Numerical methods	68
B.1	Discretisation methods	68
B.1.1	Straightforward approximations	69
B.1.2	The Newmark approximation	75
B.2	Solving a system of linear equations	76

C	Stability of RNS-p(x) simulation	78
C.0.1	Channel flow	78
C.0.2	Plane jet	79
D	Solution of a membrane model	83
D.1	The membrane model	83
D.1.1	Solutions	84
D.2	Numerical method	85
D.2.1	Discretisation	85
D.2.2	Newmark's method	86
D.2.3	Solution	86
D.2.4	Accuracy	87
D.2.5	Stability	89
E	Flowcharts	90

Chapter 1

General introduction

In this report we present a steady and an unsteady two-dimensional, laminar, incompressible channel flow model. Channel flow simulations have a broad field of applications. For example, in the field of acoustical sound production. In flue wind instruments we encounter channel geometries which play a significant role in the sound production. In biomechanics the airflow through the glottis, where voiced sound is produced, is accurately described with channel flow models. In this introduction we will discuss these two possible applications for channel flow simulation, giving an overview of what research activities are and have been done for better understanding of the physics behind it.

1.1 The flute

In spite of their long existence, the physics of many acoustic musical instruments is not yet well understood. In particular the question why recorder flutes are built the way they are is not answered. The search for the geometry giving the best sound quality is based on centuries of expertise of the instrument builders.

Many aspects of the flute are important for the quality of its sound. In a joint research effort of the University of Pierre et Marie Curie (Paris VI) and the University of Technology in Eindhoven (TUE), these aspects are studied. The studies are concentrated in experiments and numerical simulations on the acoustic behaviour of the flute.

In a recorder type flute (see figure 1.1) the musician blows into the flue channel of the mouthpiece. At the end the flue channel diverges abruptly, causing the flow to separate. A jet emerges which hits a wedge called labium. The jet starts to oscillate because it is hydrodynamically unstable. This oscillation is amplified for the eigenfrequencies of the resonator tube, producing the sound. The production of sound as a result of the interaction of the jet and the labium has been studied by Fabre et al. [6]. Currently, Ségoufin is studying the influence of the length of the flue channel in the mouthpiece, as well as the stabilizing effect of using chamfers (cutting the wake end of the flue channel under an angle of less than 90 degrees) on the sound quality [20]. At the TUE experiments have been performed on several aspects of the geometry of the flue channel. The influence of chamfers on the frequency characteristic of the produced sound has been determined [2]. Velocity profiles of the jet emerging from the flue channel have been measured [23].

From those research activities the demand rose for numerical simulation models of the flow through the flue channel. These will serve to improve the understanding of the formation of the jet at the wake end of the channel. The behaviour of this jet is very important for sound production in the flute.

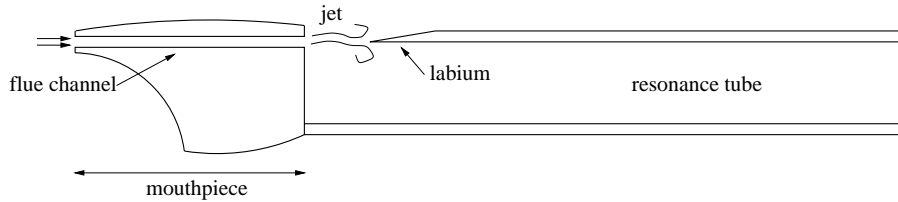


Figure 1.1: Schematic drawing of a recorder flute.

1.2 The larynx

Another interesting application of channel flow simulations is the process of human speech production in the larynx. Better understanding of the mechanical behaviour of the vocal folds will have many applications. For example in numerical synthesis of speech which could be applied in voice communication with computers, as a replacement for the keyboard and mouse. It can also be used for efficient encoding of speech for more efficient data transport in telecommunication.

In figure 1.2 a schematic drawing of the larynx is shown. Airflow coming from the lungs below is forced through the glottis, the opening between the vocal folds. Interaction of hydrodynamic forces with the elastic vocal folds induces vibration. In periodic oscillation the vocal folds produce a line spectrum with a fundamental frequency and higher harmonics. After passing the glottis, the airflow arrives in the epiglottis and the mouth, which play the role of resonators. They modulate the spectrum depending on their shape. The shape can be changed by changing the position of organs like the tongue. This process is called articulation. The oscillation of the vocal folds is in first order approximation independent of articulation, because the acoustical feedback is negligible.

Various research projects are running on the vocal folds behaviour. The Institute of Perception Research (IPO) is cooperating with several research laboratories, among which the group Gas Dynamics of the physics department of the TUE, in a project on voiced speech production. In a so-called STW project of the Rijksuniversiteit Groningen this university collaborates with the TUE on the development of artificial vocal folds (protheses). The Institute of Speech Communication (ICP) of the 'Intitut National Polytechnique' in Grenoble is working together with the TUE on the diagnostics of vocal folds pathology.

Most research activities are focused on developing numerical models for the simulation of vocal folds vibration. These models are two dimensional. The vocal folds pinch off the airway from the lungs like a pair of scissors cutting the pipe transversely (see figure 1.2), giving a rather two dimensional geometry to the opening in between, the so called glottis. This justifies the assumption of a two dimensional geometry. The two dimensional models study the flow through the glottis in the plane perpendicularly to the symmetry line between the vocal folds, in various degrees of simplification. Mostly such a model is combined with a lumped mechanical model for the vocal folds (a set of mass-spring systems), also in various degrees of complexity.

A fairly simple, two-mass model of the vocal folds, based on the classic model of Ishizaka and Flanagan is studied by Lous et al.[12], using a one dimensional quasi steady frictionless incompressible flow model. Pelorson et al.[17] have examined a similar model to this one, depicted in figure 1.3. They assume a quasi-steady incompressible frictionless flow within the glottis. The oscillation of the vocal folds is driven by the pressure in the fluid. A more complicated three-mass, body-cover model is studied by Story and Titze [22]. They use an unsteady incompressible frictionless model for the air flow. A different body-cover model is applied by Lucero [13]. In this paper the propagation of surface waves of the cover of the vocal folds in the flow direction is studied. Even in the most simple models the behaviour is very complicated.

At the Gas Dynamics laboratory of the TUE experiments have been carried out on a rigid model of the vocal folds with various shapes, including a study of flow separation [9].

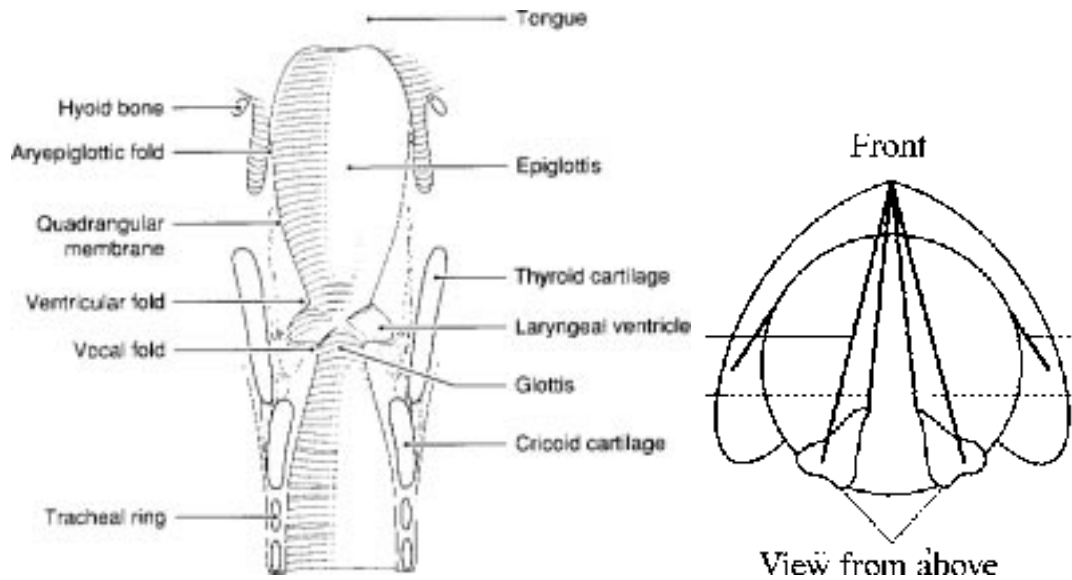


Figure 1.2: Section through the larynx showing the laryngeal airway (left) and a view of the vocal folds from above (right) (taken from [5]).

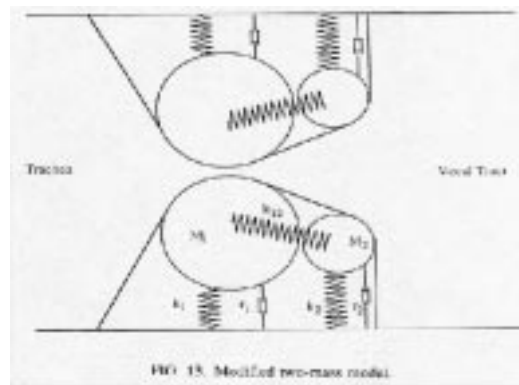


Figure 1.3: The two-mass model of the vocal folds, used by Pelorson et al.[17].

In the literature it is assumed that the most simple model predicting oscillation of the vocal folds without acoustical feedback of articulation is a mechanical model with two degrees of freedom. This is a so called two-mass model ([12],[17]). In this report we will investigate oscillation of a mechanical model for the vocal folds with only one degree of freedom (single mass model).

Interesting results have also been obtained in research on blood flow through arteries and veins. In this field models for flow in tubes and channels with deformable walls have been developed as well. Walsh [24] carried out numerical simulations on a two-dimensional incompressible, inviscid flow in an elastic tube. The tube-wall is assumed to be a membrane suspended with springs. Young and Tsai [25] have studied the behaviour of the pressure in a tube with a stenosis, and verified their model with experiments. A very accurate, but complicated model for flow through collapsible channels is used by Luo and Pedley [14]. They solve the full set of Navier Stokes equations for the flow with a finite element method, and use a general membrane model for the tube-wall.

Pedley has also performed experiments with collapsible tubes, studying pressure and flux characteristics [15].

1.3 Scope of the work

In this report we present models for steady and unsteady two-dimensional, laminar, incompressible channel flow together with the method used for numerical resolution. The report is divided into two parts, discussing two related models with different applications:

- Part I: Steady channel flow, applied on the flow in the channel in a mouthpiece of a recorder type flute.
- Part II: Unsteady channel flow, applied on the airflow induced vibration of the vocal folds.

The aim of this study was:

- to simulate the flow through the channel in a mouthpiece of a flute, with a simplified flow model and attempt to reproduce results obtained by experiments.
- to develop a coupled simulation model of the flow through the glottis and the vibration of the vocal folds using simplified models to enable real time simulation of the process of phonation.

Part I

Steady channel flow

Introduction

In the first part of this report we present a flow model which is used to calculate the jet which emerges from the flue channel in the mouthpiece of a recorder type flute. This simplified model, which is based on the Navier Stokes equations, consists of two parts. First the flow through the channel is simulated, followed by a jet flow simulation. This simulation is a lot faster than the simulation of the unsimplified Navier Stokes equations. The results of the flue channel simulation are compared with the results of experiments [23].

In chapter 2 the model of fluid flow which we used for simulation of the flue channel flow is presented. In section 2.1 we give the derivation of the channel flow model, based on the geometry of a two dimensional channel. After that we derive the model which describes the jet flow at the end of the channel, in section 2.2.

In chapter 3 the numerical method of both channel and jet flow simulation models are presented. The stability of the simulations is studied and we discuss the coupling between the two simulations for the complete flow simulation from the entrance of the flue channel to the jet behind.

In chapter 4 we present the results of the simulation of flue channel flow in comparison with experimental results.

We conclude with a discussion of the results in chapter 5.

Chapter 2

The flow model

In this chapter we present the flow models for channel flow and jet flow, respectively. Which are used to simulate the flow in a flue channel and the emerging jet. In figure 2.1 a picture of the flue channel is shown, on which the experiments from [23] are performed. When air is blown into the

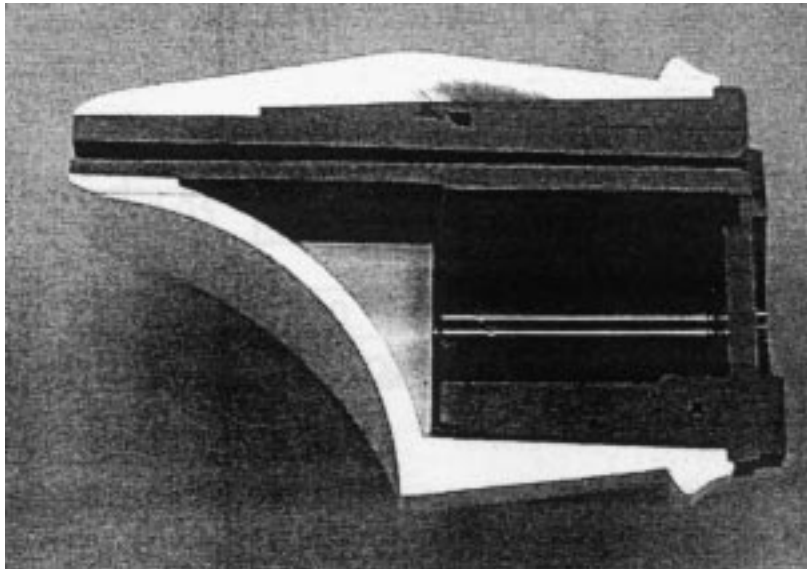


Figure 2.1: Photograph of a mouthpiece of a recorder flute (taken from [23]).

channel at the left side, boundary layers will develop in the channel. The sudden expansion of the channel just upstream of its downstream end will cause the flow to separate from the wall almost immediately. We will thus treat the flow in two coupled regimes, channel flow and an emerging jet, one after another.

We will derive a flow model which is generally applicable to incompressible, steady laminar channel flow. In section 2.1 the equations describing the fluid flow in a two-dimensional symmetric channel will be derived. This derivation is based on the Navier Stokes equations. In section 2.1.1 we simplify the equations based on estimations of magnitudes of all terms, which gives the set of equations (RNS-p(x) equations) with which we describe the fluid flow. The accuracy of this set of equations is studied in section 2.1.4 by comparing characteristics of the flow with the analytical solutions for boundary layer growth from Blasius, the fully developed Poiseuille flow and solutions of an approximate method solving boundary layer growth. The RNS-p(x) equations are applicable to two-dimensional symmetric channels with various geometries.

At the wake end of the flue channel the flow separates, caused by the rapid expansion of the channel. A two-dimensional jet will emerge from the channel into semi infinite space.

This jet flow is considered to be incompressible, steady and laminar. Jet flow is described by roughly the same equations as those for channel flow. The differences with channel flow will be discussed and we present the system of equations describing two-dimensional laminar jet flow in section 2.2. The accuracy of this set of equations is shown in section 2.2.1 by comparing its numerical solution to Bickley's analytical solution for jet flow.

2.1 Channel flow

The subject of study is the flow in a two dimensional channel of a general geometry, depicted in figure 2.2. The height of the channel may vary in the longitudinal direction x . The geometry is assumed to be symmetric with respect to middle line.

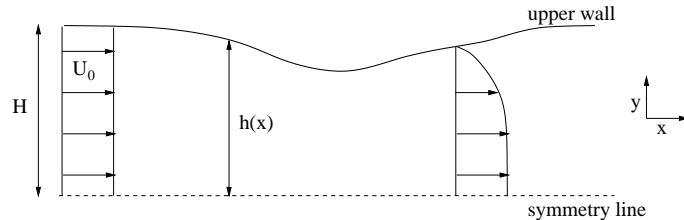


Figure 2.2: The channel geometry.

Generally, for the flow we have to solve the Navier Stokes equations

$$\frac{\partial \rho}{\partial t} + \vec{\nabla} \cdot \rho \vec{u} = 0 \quad (2.1)$$

$$\frac{\partial \rho \vec{u}}{\partial t} + \vec{\nabla} \cdot \rho \vec{u} \vec{u} = -\vec{\nabla} p + \vec{\nabla} \cdot \vec{\tau} + \vec{f} \quad (2.2)$$

in which ρ is the density of the fluid, \vec{u} is the velocity vector, p is the pressure, $\vec{\tau}$ the viscous stress tensor and \vec{f} an external body force. We like to simplify this set of equations by neglecting the least important terms based on estimation of orders of magnitude.

We consider the flue channel and the vocal cords, which are sound sources. The dimensions of the flow geometry are small with respect to the typical wavelengths of sound-waves; and velocities are low with respect to the speed of sound: $M \ll 1$. In this case mass conservation reduces locally to:

$$\vec{\nabla} \cdot \vec{u} = 0 \quad (2.3)$$

A more elaborate discussion on this approximation can be found in [9].

Furthermore, in this part we study steady flow, so we will not take time derivatives of the velocity into account. We consider laminar flow. The model will be applied to cases with Reynolds numbers ranging from order 10 up to about 1000, so it is reasonable not to consider turbulence. We also impose absence of external forces. The only force that would be a candidate is gravitation. And since the domain is vertically very small (some mm), we can neglect the influence. The momentum simplifies to:

$$\rho \left(\vec{u} \cdot \vec{\nabla} \right) \vec{u} = -\vec{\nabla} p + \mu \nabla^2 \vec{u} \quad (2.4)$$

A typical flue channel is several centimeters long, one centimeter wide, and a millimeter high. Since the height of the channel is ten times smaller than its width, we neglect the influence of the finite width. So a two dimensional geometry remains.

The coordinate system is placed with the x direction along the length of the channel and y in vertical direction. We thus consider two components of the velocity $\vec{u} = (u, v)$, and we state that the quantities are independent of z .

2.1.1 Scaling quantities

We choose suitable factors for scaling the variables and quantities, such that the scaled quantities and variables will all be of order 1. . Boundary layers will develop at the upper and lower wall of the channel. This means that the longitudinal component of the velocity will vary from 0 at the walls to its maximum value in the middle of the channel. In other words: the longitudinal velocity varies at scale U_0 on the scale H . This defines the values of two of the scaling parameters

$$x = L\bar{x} \quad y = H\bar{y} \quad u = U_0\bar{u} \quad v = V\bar{v} \quad (2.5)$$

For L we do not choose the value based on the geometry, but we will derive the scale based on fluid dynamical arguments. The same goes for the scale V for the transverse velocity.

Substituting the scaled quantities in the mass conservation gives

$$\frac{U_0}{L} \frac{\partial \bar{u}}{\partial \bar{x}} + \frac{V}{H} \frac{\partial \bar{v}}{\partial \bar{y}} = 0 \quad (2.6)$$

from which we can conclude that if we want to keep significance of both derivatives, we have to choose: $U_0/L = V/H$.

This way the momentum equation in the x -direction looks like:

$$\frac{U_0^2}{L} \left(\bar{u} \frac{\partial \bar{u}}{\partial \bar{x}} + \bar{v} \frac{\partial \bar{u}}{\partial \bar{y}} \right) = -\frac{P}{\rho L} \frac{\partial \bar{p}}{\partial \bar{x}} + \frac{\nu U_0}{H^2} \left(\frac{H^2}{L^2} \frac{\partial^2 \bar{u}}{\partial \bar{x}^2} + \frac{\partial^2 \bar{u}}{\partial \bar{y}^2} \right) \quad (2.7)$$

and in the y -direction we write

$$\frac{U_0 V}{L} \left(\bar{u} \frac{\partial \bar{v}}{\partial \bar{x}} + \bar{v} \frac{\partial \bar{v}}{\partial \bar{y}} \right) = -\frac{P}{\rho H} \frac{\partial \bar{p}}{\partial \bar{y}} + \frac{\nu V}{H^2} \left(\frac{H^2}{L^2} \frac{\partial^2 \bar{v}}{\partial \bar{x}^2} + \frac{\partial^2 \bar{v}}{\partial \bar{y}^2} \right) \quad (2.8)$$

For L we state that the viscous forces ($\nu U_0/H^2$) in the equation of momentum (2.7) must be of the same strength as the convective forces (U_0^2/L). This leads to the definition of the longitudinal scale:

$$L = \frac{U_0 H^2}{\nu} = H Re_H \quad (2.9)$$

This length can be interpreted as the scale on which a boundary layer of thickness H develops.

Since we only consider $Re_H \gg 1$, the longitudinal scale is much greater than the H and thus the $\partial^2 \bar{u}/\partial \bar{x}^2$ in equation (2.7) vanishes. Another consequence is that $V \ll U_0$. Since the momentum in y -direction is $V/U_0 = 1/Re_H$ times its x component and thus negligibly small. This yields:

$$\frac{\partial \bar{p}}{\partial \bar{y}} = 0 \quad (2.10)$$

For the magnitude of the pressure we choose $P = \rho U_0^2$ which is a scale for pressure differences when the Bernoulli equation can be applied.

2.1.2 Reduced Navier Stokes system

We rewrite equations (2.6), (2.7) and (2.10) substituting the chosen parameters and leave out the bars. The equations for conservation of mass, momentum in x and in y direction are, respectively:

$$\begin{aligned} \frac{\partial u}{\partial x} + \frac{\partial v}{\partial y} &= 0 \\ u \frac{\partial u}{\partial x} + v \frac{\partial u}{\partial y} &= -\frac{\partial p}{\partial x} + \frac{\partial^2 u}{\partial y^2} \\ \frac{\partial p}{\partial y} &= 0 \end{aligned} \tag{2.11}$$

we will refer to this set of equations as **RNS-p(x)**, the reduced set of Navier Stokes equations of which the pressure only depends on x . This in contrast to similarly reduced sets which keep both longitudinal and transverse momentum equations.

An important aspect of the channel geometry in study is symmetry. The model of the channel is symmetric with respect to the horizontal plane in the middle (see figure 2.2). The solutions of the Navier Stokes equations have this symmetry as well, provided that the entrance velocity profile is symmetric. These entrance profiles will be uniform and thus symmetric, so we solve for only one half of the flow. The origin of the coordinate system is placed in the middle of the channel, at the upstream end. The upper wall will be denoted by $y = h(x)$ (note that all is nondimensionalised with H , half the height of the channel). This restriction is not necessarily made, but all cases to which we will apply the model have this symmetry, so for these cases there is no need to keep it more general. Moreover, assuming this symmetry enables us to choose the boundary conditions unambiguously.

Boundary conditions

The equations are completed by the boundary conditions. In the precedent section we derived three equations in (2.11) for three unknowns (u , v and p). The third equation tells us the pressure is a function of x only. In the other two equations $p(x)$ remains a third unknown, whereas we now have only two equations left. Later on we will see that this is compensated for by an additional boundary condition.

In the equation of momentum the pressure gradient with respect to x appears, so we need one boundary condition for $p(x)$. For this condition we can choose the pressure value at the entrance of the channel $p(0)$.

For the longitudinal velocity u the first derivative with respect to x appears, and the second derivative in transverse direction. So for u three boundary conditions are needed. These are:

$$\begin{aligned} u &= 1 \quad \text{at} \quad x = 0 \\ u &= 0 \quad \text{at} \quad y = h(x) \\ \frac{\partial u}{\partial y} &= 0 \quad \text{at} \quad y = 0 \end{aligned} \tag{2.12}$$

The first condition corresponds to the uniform entrance velocity. No slip provides the second, and the third is implied by symmetry.

Only the first derivative of the transverse velocity with respect to y appears in the set (2.11). This means we only need one boundary condition to solve for v , but we have two conditions, namely:

$$\begin{aligned} v &= 0 & \text{at } y &= 0 \\ v &= 0 & \text{at } y &= h(x) \end{aligned} \quad (2.13)$$

the first coming from symmetry, the second from impermeability of the wall. One of these two conditions is not needed as a boundary condition. It will play the role of the third equation in order to close the formulation (note that we had only two equations to describe three unknowns).

For simplicity in numerical computation we prefer to make the wall equation disappear from the boundary conditions. This is achieved by a transformation of the transverse coordinate.

2.1.3 'Dynamic' scaling

The transformation of $\eta = y/h(x)$ achieves that throughout the channel $0 \leq \eta \leq 1$. We call this 'dynamic' scaling, since the transverse scale is a function of the position. The boundary conditions for the velocities can be expressed in $\eta = 0$ and $\eta = 1$. As a consequence of the transformation the RNS-p(x) equations will change. The derivatives with respect to x and y respond to a transformation $\xi = x$, $\eta = y/h(x)$:

$$\frac{\partial}{\partial x} = \frac{\partial \xi}{\partial x} \frac{\partial}{\partial \xi} + \frac{\partial \eta}{\partial x} \frac{\partial}{\partial \eta} = \frac{\partial}{\partial \xi} - \frac{\eta}{h} \frac{dh}{dx} \frac{\partial}{\partial \eta} \quad (2.14)$$

$$\frac{\partial}{\partial y} = \frac{\partial \xi}{\partial y} \frac{\partial}{\partial \xi} + \frac{\partial \eta}{\partial y} \frac{\partial}{\partial \eta} = \frac{1}{h} \frac{\partial}{\partial \eta} \quad (2.15)$$

The continuity and momentum equations to be solved in the channel in the new system of coordinates are given below. The derivatives above are substituted, and we rename ξ with x and η with y . This yields

$$\frac{\partial u}{\partial x} - \frac{y}{h} \frac{dh}{dx} \frac{\partial u}{\partial y} + \frac{1}{h} \frac{\partial v}{\partial y} = 0 \quad (2.16)$$

for continuity and the x momentum equation becomes:

$$u \frac{\partial u}{\partial x} - \frac{uy}{h} \frac{dh}{dx} \frac{\partial u}{\partial y} + \frac{v}{h} \frac{\partial u}{\partial y} = -\frac{\partial p}{\partial x} + \frac{1}{h^2} \frac{\partial^2 u}{\partial y^2} \quad (2.17)$$

As boundary conditions we apply no slip and an impermeable wall (no suction or injection).

$$\begin{aligned} u &= 1 & \text{at } x &= 0 \\ u &= v = 0 & \text{at } y &= 1 \\ \frac{\partial u}{\partial y} &= v = 0 & \text{at } y &= 0 \end{aligned} \quad (2.18)$$

where $y = 0$ thus corresponds with the central symmetry line, and $y = 1$ with the upper channel wall. At the entrance ($x = 0$) we prescribe the velocity profiles $u(x = 0, y)$ and $v(x = 0, y)$ (for example we give a uniform flow in longitudinal direction: $u(y) = 1$ and $v(y) = 0$).

The set of equations (2.16) through (2.17) are solved numerically. The method is discussed in chapter 3.1.

In order to show the accuracy and applicability of this set of equations we compare the numerical solution of this set applied on rather well known problems with analytical and famous approximate solutions.

2.1.4 Solutions

We present three solutions of the Navier Stokes equations applied on a very particular case. In this case we study the boundary layer growth in a channel with straight walls. The solutions to be discussed are Blasius' theory for boundary layers, the Poiseuille solutions for fully developed flow and the von Kármán method for solving boundary layer equations.

These solutions are used to test the numerical solution of the RNS-p(x) equations. In the analytically solved cases, several quantities are conserved or have a behaviour which is characteristic for the type of flow.

Before we discuss the solutions we have to introduce some quantities which we will use. These quantities are the displacement thickness and the momentum displacement thickness.

The displacement thickness is the distance over which the wall could be displaced in order to obtain the same volume flux in a frictionless (potential) flow as in the actual flow. In other words it is the thickness in which there is loss of volume flux with respect to frictionless flow. This thickness is denoted by δ_1 and is defined by:

$$\delta_1 = \int_0^1 \left(1 - \frac{u}{U}\right) dy \quad (2.19)$$

We used a slightly adapted version of the definition in order to make it applicable to channel flow, U is the velocity in the middle of the channel (scaled with U_0). We nondimensionalised the transverse coordinate by $yh(x)$ and integrate from the centre to the wall. The proper definition, though, of the transverse scale in boundary layer theory is $\sqrt{Re_x}$ (see for example [19]). The other difference is that in the definition is integrated up to infinity, while here is integrated from the centre to the wall. This is a consequence of our definition: since u varies from 0 at the wall(s) to U in the middle.

Another thickness we will need is the momentum displacement thickness. This thickness is associated with the loss of momentum in the boundary layer. The total loss of momentum in the boundary layer, compared with potential flow of velocity U , is $\rho \int_0^1 u(U - u)dy$. The momentum thickness δ_2 is defined such that:

$$\rho U^2 \delta_2 = \rho \int_0^1 u(U - u) dy \quad (2.20)$$

or,

$$\delta_2 = \int_0^1 \frac{u}{U} \left(1 - \frac{u}{U}\right) dy \quad (2.21)$$

First we consider a straight channel, in which $h(x) = \text{constant}$. Here we encounter two regimes for which analytical solutions exist: entrance flow and developed channel flow. Near the entrance the thickness of the boundary layers will be much smaller than the height of the channel, and in fact we can regard the problem as a boundary layer developing above a flat plate placed in flow. This case has the famous Blasius' solution [19, VII e]. This solution describes the development of the boundary layer on a flat plate, with a so-called self-similar profile.

On the other hand the development of flow in a straight channel has been solved by means of an integral method: the method of von Kármán.

Further downstream, where the flow is fully developed, we encounter Poiseuille's solution. The simulation results of the development of the flow in a straight channel is depicted in figure 2.3, from which it can be seen that the parabolic Poiseuille profile appears downstream.

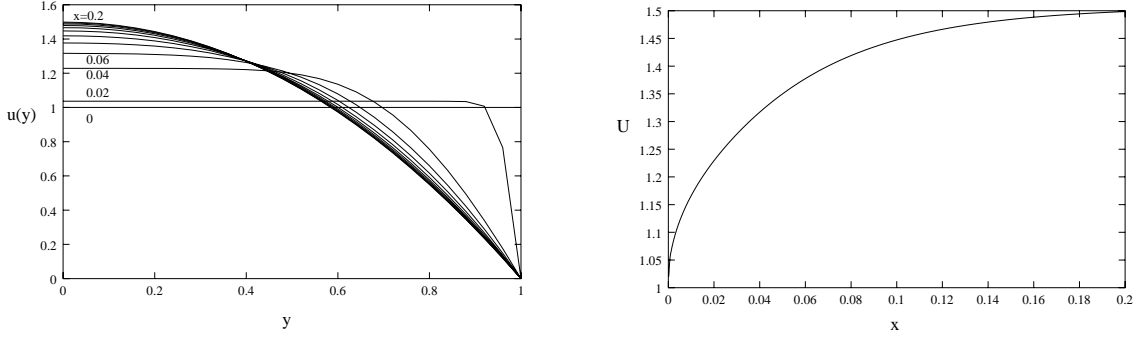


Figure 2.3: Velocity profiles $u(y)$ at several of the longitudinal coordinate x (left) and the development of the central velocity (right). The parabolic Poiseuille profile is attained at $x \approx 0.2$.

Blasius

Very close to the entrance we can regard the flow close to one wall, neglecting the existence of the opposite wall, as if it were infinitely far away. In this case Blasius' theory can be applied. We will not go into detail on this theory (for that, see e.g. [19, IX h]), but we give only the main idea and the important properties of the solution.

The key is that Blasius' solution is self-similar. The longitudinal component u of a self-similar solution has the property that two profiles $u(x, y)$ located at different x -coordinates differ only by a factor in u and y , having the same shape. By choosing an appropriate transformation of the transverse coordinate these profiles can all be made congruent.

This transformation of the transverse coordinate is $y = \eta\sqrt{U_0x/\nu} = \eta\sqrt{Re_x}$. The factor $\sqrt{Re_x}$ which is among others the factor of growth for all physical thicknesses (of the boundary layer δ , displacement δ_1 , momentum δ_2 , etc.) in a boundary layer on a flat plate.

The displacement thickness develops according to this theory:

$$\delta_1 \simeq 1.72\sqrt{Re_x} \quad (2.22)$$

With this we can derive some typical features of channel entrance flow.

From the definition of the displacement thickness we can derive a relation between the velocity of the main flow U , in the middle of the channel, and the displacement thickness δ_1 . If we that assume the main flow is uniform (not yet disturbed by the boundary layers) and a flux conservation in x direction, this relation will be given by:

$$U(x) = \frac{\Phi}{2(1 - \delta_1(x))} \quad (2.23)$$

where the flux is given by:

$$\Phi = 2 \int_0^1 u dy = 2 \quad (2.24)$$

recalling that at the entrance we introduce a flat profile of velocity 1. With dimensions we would find a volume flux equal to $2HU_0$.

For uniform flow we can apply Bernoulli's formula to calculate the pressure:

$$\frac{dp}{dx} = -U \frac{dU}{dx} \quad (2.25)$$

Substituting relation (2.23) for the velocity U and integrating, this becomes:

$$\begin{aligned} p(x) &= -\frac{1}{2} (1 - \delta_1)^{-2} + \frac{1}{2} \\ &\simeq -\delta_1 \simeq -1.72\sqrt{Re_x} \end{aligned} \quad (2.26)$$

For the second equality we used a Taylor development of $(1 - \delta_1)^{-2}$, assuming that $\delta_1 \ll 1$.

Summarizing we find that near the entrance of the channel all thicknesses and the pressure function are proportional to \sqrt{x} . This can be seen from figure 2.5 where these solutions of the growth of δ_1 are plotted as a function of x , among others. The pressure is plotted in figure 2.4.

Poiseuille

Further downstream the flow develops a steady profile: the Poiseuille profile. Poiseuille flow is parallel and fully developed. The velocity profile does not change in the flow direction. When we substitute for these properties in the equation of momentum (2.17), we can derive the velocity profile. In this case ($v = 0$ and also $\partial u/\partial x = 0$) the momentum equation becomes:

$$\frac{\partial^2 u}{\partial y^2} = \frac{\partial p}{\partial x} \quad (2.27)$$

the solution is a parabola:

$$u(y) = -\frac{1}{2} \frac{\partial p}{\partial x} (1 - y^2) \quad (2.28)$$

which attains its maximum value at $y = 0$ (the centre of the channel) and is zero at both walls. The negative sign relates a decreasing pressure to a flow in positive x direction.

Directly from the Poiseuille profile (2.28) with the definition of the displacement thickness (2.19), we obtain the displacement thickness in Poiseuille flow:

$$\delta_1 = \frac{1}{3} \quad (2.29)$$

This is also plotted in figure 2.5.

Integrating equation (2.28) over y gives the flux. If the entrance profile is uniform with velocity U_0 (=1 without dimension), we obtain from conservation of flux:

$$\frac{\partial p}{\partial x} = -3 \quad (2.30)$$

Substituting this into (2.28) gives that the velocity on the centre line of the Poiseuille profile is 3/2 times the entrance velocity. In the left graph of figure 2.3 the maximum velocity on the middle line of the channel is plotted as a function of x solved with the RNS-p(x) simulation, which reaches the value of 3/2. In figure 2.4 the pressure curve is given as a function of x . It can be seen that the pressure follows Blasius' solution at the entrance and Poiseuille's curve further downstream.

von Kármán

An approximate method of solving the boundary layer problem is the von Kármán method. This method is an integral method, it is based on integration of the equation of motion over the boundary layer. This way the solution will satisfy only the mean differential equation within the boundary layer, and the boundary conditions. It is applied when we are not interested in satisfaction of the differential equations at every point. An integral method for solution of the

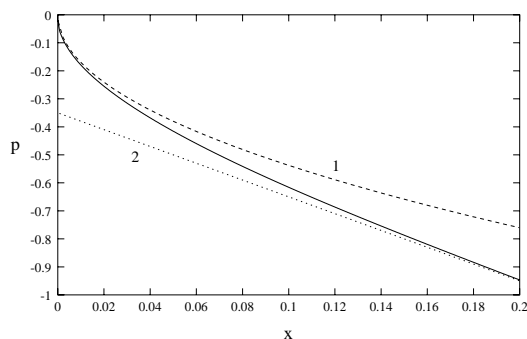


Figure 2.4: Development of the pressure $p(x)$ in a straight channel. The dashed curve (1) depicts the pressure behaviour at the entrance (Blasius) and the dotted (2) in Poiseuille flow.

boundary layer problem is desirable if an analytical solution is too complicated or does not exist. The reason why we give this method here is because it is a very popular and well known method.

By integrating the momentum equation in x -direction, from (2.11) over y (from 0 to 1, using continuity (the first equation in (2.11)) and substituting the definitions of δ_1 and δ_2 , we obtain the famous von Kármán equation:

$$\frac{d}{dx} (\delta_2 U^2) + \delta_1 U \frac{dU}{dx} = \left. \frac{\partial u}{\partial y} \right|_{y=0} \quad (2.31)$$

This equation can be solved if we provide additional equations: the closure. In appendix A two types of closures are discussed: the Falkner Skan closure and polynomial closures. The polynomial closures provide expressions for the longitudinal velocity profile $u(y)$, being a polynome of y of some degree which satisfies the boundary conditions, containing a free parameter associated with the boundary layer thickness. In this case we can calculate the thicknesses with their definitions and the shear stress term (the right hand side of equation (2.31)), in terms of this parameter. Substituting these quantities in (2.31) and integrate this equation, we can solve for the unknown parameter.

The Falkner Skan closure provides numerical expressions for the dependence of the thicknesses and stress term as a function of the boundary layer thickness. This closure requires numerical integration of the von Kármán equation, which is explained in [11].

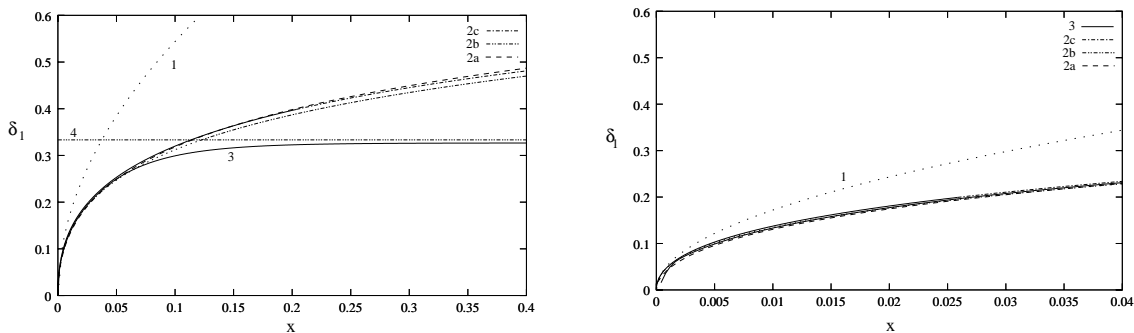


Figure 2.5: The development of the displacement thickness δ_1 in the straight channel, calculated with four different methods: (1) Blasius' solution, von Kármán with (2a) FS closure, (2b) polynomial closure of the first and (2c) fourth degree and (3) RNS-p(x) channel flow simulation. Line (4) represents δ_1 in Poiseuille flow. The right figure is a close look at the entrance of the channel.

The growth of the displacement thickness, calculated with these methods are depicted in figure

2.5, together with the solutions by Blasius and Poiseuille, in order to test the accuracy of the RNS-p(x) equations. From these graphs it can be seen that the growth of the displacement thickness calculated by the RNS-p(x) simulation is close to Blasius' solution at the entrance, and approaches the value of Poiseuille flow downstream. It is also in accordance with the solution of the integral method. Though the integral solution does not restrict the growth of the displacement thickness to an upper limit like the value in fully developed flow.

2.2 Plane jet

For the jet flow model we roughly make the same assumptions as for channel flow. We consider two dimensional, steady, incompressible and laminar flow. The jet emerges from the end of the channel into a semi infinite space. In the transverse direction there is no border (mathematically spoken). The jet has a transverse dimension of the height of the channel at its end, and the coordinate y will thus be scaled with this factor, which is a constant throughout the domain. Since we assume symmetric solutions in the channel, with respect to the horizontal plain in the middle, only symmetric solutions are regarded for the jet as well.

Assuming again equilibrium between viscous and convective forces, like in section 2.1, the longitudinal scale from equation (2.9) is applied. Again we use the scales:

$$x = L\bar{x} \quad y = H\bar{y} \quad u = U_0\bar{u} \quad v = V\bar{v} \quad (2.32)$$

but here H corresponds with half the height of the channel at its open end where the jet emerges.

There are some important differences with the equations we use to solve channel flow. One is that we assume a constant pressure everywhere in the domain of the jet. This is a very common assumption (see [19]), since the surrounding fluid is at rest. The absence of a pressure gradient there impresses itself on the jet. The second difference between channel flow and jet flow is the infiniteness of the domain in transverse direction of jet flow.

The set of equations describing this jet flow are thus the same as for the channel flow from section 2.1.2. But we assume the absence of a pressure gradient. The set of equations describing a two dimensional laminar jet is written:

$$\boxed{\begin{aligned} \frac{\partial u}{\partial x} + \frac{\partial v}{\partial y} &= 0 \\ u \frac{\partial u}{\partial x} + v \frac{\partial u}{\partial y} &= \frac{\partial^2 u}{\partial y^2} \\ p &= \text{constant} \end{aligned}} \quad (2.33)$$

For conservation of mass, momentum in longitudinal and in transverse direction, respectively. The boundary conditions are straightforward. Essentially we have two (the third equation gives trivial solutions) equations for two unknowns. Two conditions for u are needed and one for v , which are rather straightforward:

$$\begin{aligned} u &= 0 \quad \text{for} \quad y \rightarrow \infty \\ \frac{\partial u}{\partial y} &= v = 0 \quad \text{at} \quad y = 0 \end{aligned} \quad (2.34)$$

The latter are because we regard symmetric solutions. Again $y = 0$ corresponds to the plain of symmetry.

2.2.1 Solutions

Like in Blasius' theory for the boundary layer flow, the jet has also self-similar solutions, described by Bickley's theory. In this section we will just highlight some features of the Bickley solution, for explanation, the reader is referred to Schlichting [19].

Bickley's solution

The self-similar Bickley profile for the longitudinal velocity is a rather simple function:

$$u(y) = \frac{1}{\cosh^2(y)} \quad (2.35)$$

As the jet moves forward the profile expands, because it drags the surrounding fluid as a consequence of friction (see figure 2.6). The jet also slows down, the Bickley solution has the property

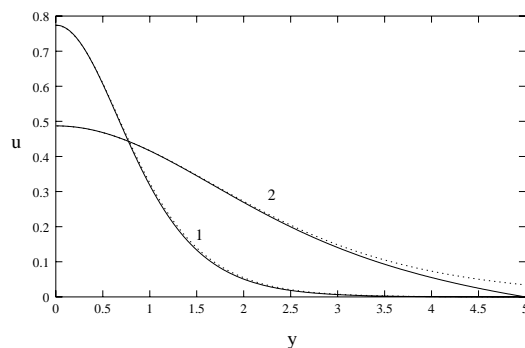


Figure 2.6: Two calculated profiles of u and their corresponding Bickley profiles (dotted curves). Profile 1 is recorded close to the slit and 2 further downstream. From curve 2 it can be seen that the simulation loses accuracy if the transversal domain is limited where the u is nonzero.

that the velocity in the centre of the jet decreases according to: $U \sim x^{-1/3}$. This means that the ratio $U/(dU/dx)$ for a jet has the following property:

$$\frac{U}{dU/dx} \sim -3x \quad (2.36)$$

There is a special feature of the RNS-p(x) in the model for the jet, (2.33). The absence of a pressure gradient causes that the total flux of momentum is conserved in the flow direction. This can be obtained by integrating the momentum equation over y , which results in:

$$\frac{\partial}{\partial x} \int_0^{\infty} u^2 dy = 0 \quad (2.37)$$

In figures 2.7 and 2.8 the above discussed quantities, calculated by the numerical solution of equations (2.33) are plotted. In each figure four curves are shown, corresponding to four different profiles exerting from the slit. The curves in figure 2.7 show that all entrance profiles develop similar profiles downstream. The development of the quantity in equation (2.36) and the momentum flux in longitudinal direction are traced in figure 2.8. From which one can see that all different profiles behave as expected from Bickley's theory.

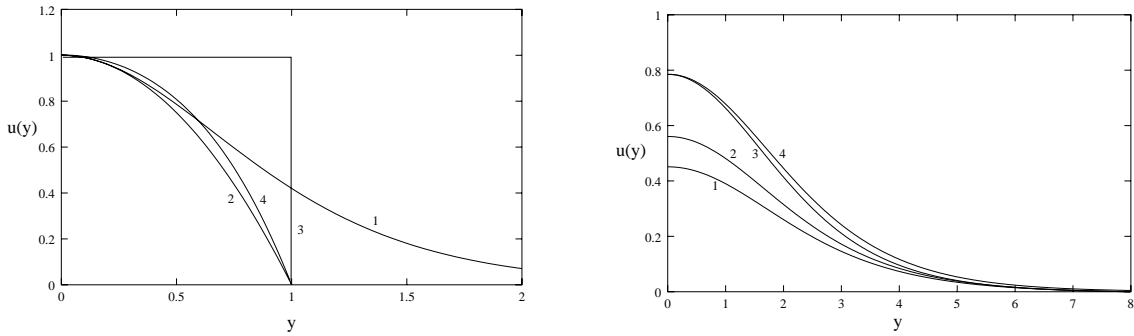


Figure 2.7: The four entrance profiles (left) and their calculated shape at $x = 0.5$ (right). The numbers correspond with the profiles: (1) self similar (Bickley); (2) parabolic (Poiseuille); (3) flat profile; (4) calculated with the channel flow simulation at the exit of the flue channel ($Re_H = 300$).

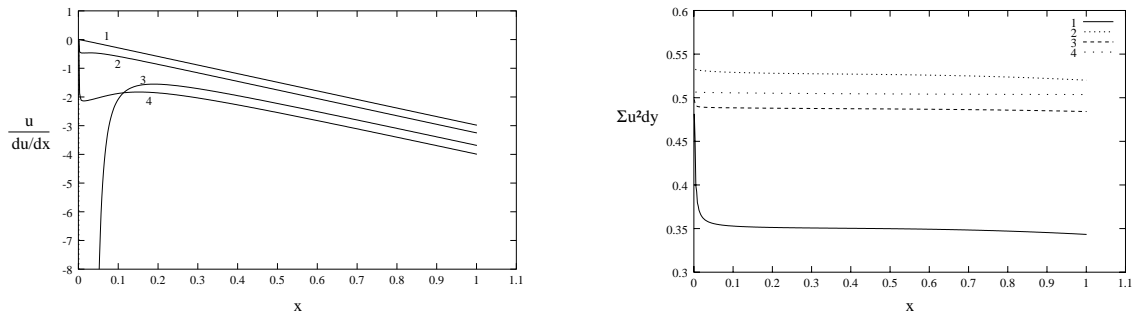


Figure 2.8: The ratio $U/(dU/dx)$ (left) and the momentum flux as a function of x for four different entrance profiles. The numbers correspond to those in figure 2.7. Line number 1 in the left figure coincides exactly with $-3x$, predicted by Bickley.

Chapter 3

Numerical method

In this chapter the numerical method for solution of the RNS-p(x) equations is presented, based on the method of finite differences.

In section 3.1 we discuss channel flow. First we present the grid used for the discretisation of the domain of channel flow. Then the RNS-p(x) equations (2.11) are given in the discrete form, with explanation on the method of approximations of derivatives in section 3.1.1. After that, the numerical solution of these discrete equations is written out step by step in section 3.1.2. The accuracy of this solution, which has already been presented in chapter 2, and the stability are briefly discussed in section 3.1.3.

The model for jet flow is discussed in section 3.2. The discrete form of the equations (2.33) is presented in section 3.2.1. The numerical solution of those equation is explained in section 3.2.2. And the accuracy and stability of the numerical solution is discussed in section 3.2.3.

At the end of this chapter we explain how the two models are coupled to obtain the complete simulation of channel and jet flow. This is done in section 3.3, and an example of such a simulation is discussed and compared with the results of a commercial code FLUENT, which solves the complete set of Navier Stokes equations.

There are a lot of different ways to write the discrete form of the differential equations of this problem. In general the freedom lies in the choice of the approximation of each differential term and the location of each term in the domain. Shortly, the difficulty comes down to the choice of indices associated to the quantities in play.

For example the equation describing an undamped mass spring system can be approximated in many ways. In appendix B a short introduction to discrete approximation of derivatives is given, applied on the mass spring problem. It will discuss three simple methods of approximation, which only differ in the choice of indices, and one more elaborate method which is unconditionally stable. For the three simple methods the effect of this choice of indices on the accuracy and stability of the numerical solution is shown.

For further reading one is referred to Cousteix [3, Chapter 8] and Peyret & Taylor [18, Chapter 2].

3.1 Channel flow

The two dimensional domain in the channel is divided into a grid $n_x \times n_y$, see figure 3.1 Discretisation of the quantities defined on this domain:

$$u_{i,j} = u(x_i, y_j) \quad (3.1)$$

$$v_{i,j} = v(x_i, y_j) \quad (3.2)$$

$$p_i = p(x_i) \quad (3.3)$$

for $0 \leq i \leq n_x$ and $0 \leq j \leq n_y$. The height of the channel is written as $h_i = h(x_i)$

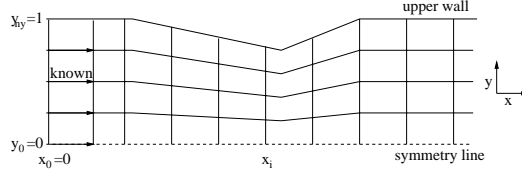


Figure 3.1: The numerical representation of the the channel geometry.

As mentioned before we prefer to restrict y between 0 and 1, instead of 0 and $h(x)$ (see section 2.1.3). This means we adjust the transverse pace $dy = h_i/n_y$ in order to fit the grid into the channel. The advantage of this is that the boundary conditions remain the same all over the domain, and that the number of calculation points is conserved throughout the domain. Only a rather simple coordinate transformation is required, given in section 2.1.3.

The main idea of the solution is that we start at $x = x_0$, where we know u and v for all y , and advance in x . At every step in x we solve the velocities for all y using the RNS-p(x) equations.

3.1.1 Discrete RNS-p(x) equations

We present the discrete form of the RNS-p(x) equations and discuss the approximations of the derivatives in it briefly. Here the terms with index i are known and we want to calculate those with index $i + 1$. Except for the geometry function h which is given for all x_i at forehand.

For the x momentum equation (2.17) the following discrete form is chosen:

$$\begin{aligned} u_{i,j} \frac{u_{i+1,j} - u_{i,j}}{\Delta x} + \frac{1}{h_{i+1}} \left(v_{i,j} - u_{i,j} y_j \frac{h_{i+1} - h_i}{\Delta x} \right) \frac{u_{i,j+1} - u_{i,j-1}}{2\Delta y} \\ = - \frac{p_{i+1} - p_i}{\Delta x} + \frac{u_{i+1,j+1} - 2u_{i+1,j} + u_{i+1,j-1}}{h_{i+1}^2 \Delta y^2} \end{aligned} \quad (3.4)$$

The terms with index i are known for all j , those with $i + 1$ are to be solved.

For the first term in the left member we chose a straightforward discrete form, which is very close to the definition of the derivative of a function f :

$$\frac{df(x)}{dx} \equiv \lim_{\Delta x \rightarrow 0} \frac{f(x + \Delta x) - f(x)}{\Delta x} \quad (3.5)$$

The second term contains the derivative $\partial u / \partial y$ which we have centered in y_j . Appendix B argues that the error of this approximation is of order Δy^2 . This in contrast to the error Δx of the simple 'forward' form applied in the first term, which we cannot centre in the same way, because we can only take one step at the time in x .

The pressure gradient appears in the simple 'forward' form.

The friction term is centered about y_j which is the most standard form of approximating a second order derivative. The error made is conform equation (B.24) of appendix B of the order of Δy^2 .

The boundary conditions for the longitudinal velocity are conform (2.12):

$$\begin{aligned} u_{i+1,1} - u_{i+1,0} &= 0 \\ u_{i+1,n_y} &= 0 \end{aligned} \quad (3.6)$$

the former due to the fact that we assume symmetric solutions; the latter because we apply the no-slip condition.

In equation (3.1.1) we encounter two unknowns, namely the longitudinal velocity ¹ \mathbf{u}_{i+1} and the pressure p_{i+1} . Once we have \mathbf{u}_{i+1} we can solve for \mathbf{v}_{i+1} by integrating the continuity equation, of which the discrete form looks like:

$$\frac{v_{i+1,j+1} - v_{i+1,j}}{\Delta y} = -h_{i+1} \frac{u_{i+1,j+1} - u_{i+1,j}}{\Delta x} + y_j \frac{h_{i+1} - h_i}{\Delta x} \frac{u_{i+1,j+1} - u_{i+1,j}}{\Delta y} \quad (3.7)$$

Here the boundary conditions are, conform (2.1.2):

$$v_{i+1,0} = v_{i+1,n_y} = 0 \quad (3.8)$$

by symmetry and impermeability, respectively.

The following section will explain the procedure which is followed for the solution of this system of equations.

3.1.2 Solution

In the momentum equation (3.1.1) we can arrange all terms containing \mathbf{u}_{i+1} to the left hand side, and all known terms to the other. The equation can be written in the form:

$$\mathbf{A} \mathbf{u}_{i+1} = \mathbf{b}_i + \left. \frac{dp}{dx} \right|_{i+1} \quad (3.9)$$

where \mathbf{A} is a matrix and \mathbf{u}_{i+1} is a column vector $u_{i+1,j}$. In fact \mathbf{A} is a matrix with values different from zero on three diagonals, a tridiagonal matrix. On the main diagonal there are the quantities in y_j and the lower and upper diagonals contain quantities in y_{j-1} and y_{j+1} , respectively. The vector \mathbf{b}_i contains all terms with index i , so they are all known. The pressure gradient is exactly the one appearing in the right hand side of (3.1.1). The solution goes as follows.

At the entrance of the channel we give the velocity profiles for u and v . For example a uniform entrance flow in longitudinal direction will be given by $u_{0,j} = 1$, $v_{0,j} = 0$. The value of the pressure at the entrance will be chosen equal to zero.

Estimation of p_{i+1}

First, a value for the pressure p_{i+1} is estimated. For p_0 we will take 0 as value, while for larger i we estimate roughly:

$$p_{i+1} = \left. \frac{dp}{dx} \right|_i dx + p_i = 2p_i - p_{i-1} \quad (3.10)$$

which is just extrapolation of the pressure gradient. This first approximation is further improved in an iterative process, described in the following paragraphs.

¹For convenience we denote the y dependence of the velocities by writing \mathbf{u}_{i+1} which represents the vector $u_{i+1,j}$. Note that the pressure is independent of y .

Calculation of \mathbf{u}_{i+1}

Next, we solve for \mathbf{u}_{i+1} by inversion of the matrix \mathbf{A} from equation (3.9). Since the matrix is tridiagonal, a very quick method for inversion can be applied. This method is called the method of factorization. It is briefly explained in appendix B.

Calculation of \mathbf{v}_{i+1}

The transverse velocity is calculated by integration of the continuity equation (3.7) over y . We begin at $j = 0$ where $v = 0$ and go up to the upper wall, where we end up with a certain value of v_{i+1,n_y} which will probably not be equal to zero (because we do not yet know the exact value for the pressure p_{i+1})!

The whole solution \mathbf{u}_{i+1} and \mathbf{v}_{i+1} depend on the pressure p_{i+1} , especially the value v_{i+1,n_y} . We write this dependence as a function $v_{ny}(p)$. The boundary condition (3.8) tells us it has to be equal to zero. If the deviation from zero is greater than 10^{-9} , we try another value of p_{i+1} , calculated by means of a Newton iteration.

Newton iteration on the pressure

In this iteration we calculate the derivative of $v_{ny}(p)$, at the estimated value of p_{i+1} . This derivative $\delta v / \delta p$ is calculated by rerunning the solution of \mathbf{u}_{i+1} and \mathbf{v}_{i+1} twice, with a pressure $p_{i+1} + \epsilon$ and $p_{i+1} - \epsilon$.

$$\delta v / \delta p = \frac{v_{ny}(p + \epsilon) - v_{ny}(p - \epsilon)}{2\epsilon} \quad (3.11)$$

where we chose $\epsilon = 5 \times 10^{-9}$

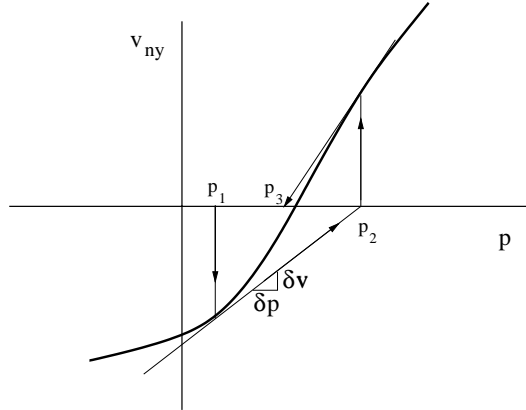


Figure 3.2: Three steps of a Newton iteration process to obtain the zero of the function $v_{ny}(p)$.

For the next value of the pressure we extrapolate the derivative $\delta v / \delta p$ from the 'old' value until it hits $v_{ny}(p) = 0$.

$$p_{new} = p_{old} - \frac{v_{ny}(p_{old})}{\delta v / \delta p} \quad (3.12)$$

And we start all over again from 'Calculation of \mathbf{u}_{i+1} ' using the value p_{new} as p_{i+1} . The Newton iteration is visualized in figure 3.2. The iteration stops when the transverse velocity at the wall is sufficiently small: $v_{ny}(p) < 10^{-9}$.

When this condition is satisfied, the profiles \mathbf{u}_{i+1} and \mathbf{v}_{i+1} have been found, and we can pass on to the next step in x . We start the calculation again from 'Estimation of p_{i+1} '. The whole program is visualized in a flow chart in figure E.1.

Briefly, the RNS-p(x) simulation could be summarized as a black box which solves the velocity field in and the pressure drop Δp over the channel, for a given entrance velocity (flux Φ).

3.1.3 Accuracy and stability

To test the accuracy of the numerical method used for resolution of channel flow, we compare several results with theoretical solutions. In section 2.1.4 the simulation results of flow through a straight channel are presented. They are compared with three other methods of solving this type of problem. Two of those methods are analytic: Blasius' and Poiseuille's theory and the third is an approximate method: von Kármán method.

In that section we have seen that the longitudinal velocity develops a parabolic profile (figure 2.3) with its maximum value according to Poiseuille. The pressure curve follows Blasius' solution near the entrance of the channel, and further downstream the gradient becomes constant with value -3 from Poiseuille (figure 2.4). The development of the displacement thickness has been compared with Blasius' and Poiseuille's solutions also, and with the solution of von Kármán as well. In figure 2.5 the curves of δ_1 of the RNS-p(x) simulation and the solutions from section 2.1.4 are plotted. From this figure it can be seen that the solution of the RNS-p(x) model run off as Blasius, like the von Kármán solution, and it reaches Poiseuille's value downstream. The displacement thickness from Blasius' and von Kármán's theory grow infinitely large. This is because they are essentially developed for boundary layer growth in a non-confined flow, which does not limit the growth of boundary layers.

The stability of the numerical solution of the RNS-p(x) equation is studied by rerunning the calculation taking different step-sizes in both x and y directions. In the study the basis geometry used is that of the flue channel. We focused our attention on the diverging part of the flue channel, where the flow tends to separate. Appendix C contains the full text examination of stability. As can be seen in this appendix, flow separation may cause instabilities in the simulation, the solution is not convergent. Flow separation is a consequence of rapid expansion of the channel geometry. By choosing a grid which is dense enough we can in general obtain convergent solutions. For example in appendix C we have shown that for the channel geometry which resembles the flue channel (which expands 35 faster than it converges) maximum step-sizes dx and dy can be found for which calculation results show smooth curves. For the chosen geometry we have to use at least 50 points in transverse direction, in order to obtain convergence of the solution. If the channel expands less rapidly we need fewer points. In the geometry with the same angle convergence as the flue channel, but which expands twice as fast as it converges, instead of 35 times as fast, we only needed 20 points transversally for convergence.

We can conclude qualitatively that the more rapidly the geometry changes the denser the grid has to be to obtain convergent results.

3.2 Plane jet

In the next section the numerical solution of the equations describing jet flow (2.33) is explained. In general the same method is used as for channel flow simulation. Though the absence of a pressure gradient forces us to use a slightly different technique.

3.2.1 Discretisation

The solution method for channel flow (section 3.1.2) applied to a free moving jet described by (2.33) is not convergent. The absence of the pressure gradient forces us to 'smoothen' the calculation in another way. This can be achieved by mediating the implicit (with index $i + 1$) and explicit value

(the known value at x_i) of some terms. This leads to the following possible discrete form of the momentum equation:

$$\begin{aligned} u_{i+1/2,j} \frac{u_{i+1,j} - u_{i,j}}{\Delta x} + v_{i+1/2,j} \frac{u_{i+1,j+1} - u_{i+1,j-1}}{2\Delta y} \\ = \frac{u_{i+1/2,j+1} - 2u_{i+1/2,j} + u_{i+1/2,j-1}}{\Delta y^2} \end{aligned} \quad (3.13)$$

where we defined the the halfway terms:

$$u_{i+1/2,j} = \frac{1}{2} (u_{i+1,j} + u_{i,j}) \quad (3.14)$$

and idem for $v_{i+1/2,j}$. Again we state that all terms with index i are known (implicit terms) and we solve for the explicit terms which have index $i + 1$.

We cannot solve this equation directly for \mathbf{u}_{i+1} , since it is not linear. The exact way involves iteration on \mathbf{u}_{i+1} and \mathbf{v}_{i+1} . In this iteration process we will solve for the transverse velocity which is defined implicitly in equation 3.2.1. The iteration process is explained in the next section.

In equation (3.2.1) the derivative $\partial u / \partial x$ appears in the simple 'forward' manner, giving an error in the order of Δx . The derivative $\partial v \partial y$ is centered in y_j , as well as the viscous term on the right hand side, both giving an error in the order of Δy^2 . Globally we approximated the momentum equation in the same way as that for channel flow.

The discrete boundary conditions for the longitudinal velocity in the jet are:

$$\begin{aligned} u_{i+1,n_y} &= 0 \\ u_{i+1,0} - u_{i+1,1} &= 0 \end{aligned} \quad (3.15)$$

The profile of the transverse velocity, \mathbf{v}_{i+1} , is calculated via the flux (or stream function) ψ , unlike the channel flow solution, but it comes down to the same thing. In fact first we integrate the longitudinal velocity over y :

$$\psi_{i+1,j+1} = \psi_{i+1,j} + \frac{u_{i+1,j+1} + u_{i+1,j}}{2} \Delta y \quad (3.16)$$

with boundary condition:

$$\psi_{i+1,0} = u_{i+1,0} \frac{\Delta y}{2} \quad (3.17)$$

Next, the transverse velocity is the derivative of the flux with respect to x :

$$v_{i+1,j} = - \frac{\psi_{i+1,j} - \psi_{i,j}}{dx} \quad (3.18)$$

In the former two equations only direct straightforward discrete forms appear. For the transverse velocity we have boundary condition $v_{i+1,0} = 0$ from (2.34). The following section deals with the exact procedure followed for solution.

3.2.2 Solution

Iterating on the unknown velocities enables us to linearize equation (3.2.1) in terms of the unknowns. For the momentum equation the following form is chosen, where N is the index of iteration:

$$\begin{aligned} \frac{1}{2} (u_{i+1,j}^N + u_{i,j}^N) \frac{u_{i+1,j}^{N+1} - u_{i,j}^N}{\Delta x} + \frac{1}{2} (v_{i+1,j}^N + v_{i,j}^N) \frac{u_{i+1,j+1}^{N+1} - u_{i+1,j-1}^{N+1}}{2\Delta y} \\ = \frac{1}{2} \left(\frac{u_{i+1,j+1}^{N+1} - 2u_{i+1,j}^{N+1} + u_{i+1,j-1}^{N+1}}{\Delta y^2} + \frac{u_{i,j+1} - 2u_{i,j} + u_{i,j-1}}{\Delta y^2} \right) \end{aligned} \quad (3.19)$$

In the first step of iteration all terms with index N are equal to the terms from the precedent position $x = x_i$.

We bring all terms which have index $N + 1$ to the left hand side and obtain a form like in (3.9):

$$\mathbf{A} \mathbf{u}_{i+1}^{N+1} = \mathbf{b}_i^N \quad (3.20)$$

Note that in this equation the terms with index N are known (they are calculated in the precedent iteration step). In \mathbf{A} as well as in \mathbf{b} terms with index i and iteration index N appear. In the following the solution is laid out step by step.

Calculation of \mathbf{u}_{i+1}^{N+1}

First, the equation is solved for \mathbf{u}_{i+1}^{N+1} from equation (3.20). The matrix \mathbf{A} is inverted using the method of factorization.

Calculation of \mathbf{v}_{i+1}^{N+1}

We solve for \mathbf{v}_{i+1} , by differentiation of the flux, which is calculated according:

$$\psi_{i+1,j+1}^{N+1} = \psi_{i+1,j}^{N+1} + \frac{u_{i+1,j+1}^{N+1} + u_{i+1,j}^{N+1}}{2} \Delta y \quad (3.21)$$

where we depart from $\psi_{i+1,0}^{N+1} = u_{i+1,0}^{N+1} dy/2$. Next, the transverse velocity will be calculated by

$$v_{i+1,j}^{N+1} = -\frac{\psi_{i+1,j}^{N+1} - \psi_{i,j}}{\Delta x} \quad (3.22)$$

where we depart from $v_{i+1,0}^{N+1} = 0$.

Once we have calculated the transverse velocity profile, we rename all indices $N + 1$ by N and begin at 'Calculation of \mathbf{u}_{i+1}^{N+1} '. This is done until the difference between u^{N+1} and u^N for all j is less than 10^{-9} . Once this condition is satisfied, we advance in x .

This procedure is visualized by aid of a flowchart in figure E.2.

3.2.3 Accuracy and stability

In order to test the accuracy of the the numerical solution of the RNS-p(x) equations some results are compared with properties of the analytical Bickley solution. The first test is the self similarity of the Bickley profile. We introduce a Bickley profile from equation (2.35) at the slit, and watch its development. In figure 2.6 two calculated jet profiles are plotted along with their corresponding Bickley-shaped profiles. We see a fairly good accordance between the two. A difference appears, though, when the jet has enlarged as much as the transverse domain. In the figure the transverse domain is running from 0 to 5. The boundary condition for u at the upper end causes the profile to differ from the Bickley solution. Secondly the development of several different entrance profiles and the ratio $U/(dU/dx)$ and the momentum flux are traced as a function of x (figures 2.7 and 2.8). These are compared with the behaviour predicted by Bickley's theory. From that figure it can be seen that all profiles adapt to the Bickley solution, with its features.

The stability of the jet flow simulation is studied by varying the number of points in the domain. The results are given in appendix C. From that we can conclude that near the slit (small values of x) where the jet emerges into space the longitudinal step-size dx plays a dominant role in convergence. Further downstream, where the jet has expanded transversally, the size of the transverse domain becomes important. This is a consequence of the boundary conditions: we require u to go to zero at position n_y . Due to this choice the numeric solutions will differ from Bickley's solution

when the jet has expanded so much that longitudinal Bickley profile differs significantly from zero at that point.

The channel and jet flow simulations have now been discussed separately. In order to apply it on the flue channel flow, the two simulations have to be coupled. This coupling is discussed in the next section. We describe the actual acts of coupling and the compare the results of such a simulation, ran on a simple channel-jet geometry, with the same simulation performed by a commercial code FLUENT which solves the complete set of Navier Stokes equations.

3.3 The coupled simulation

With an eye on the goal of simulation of flue channel flow, we discuss here the coupling of the simulations of channel flow and jet flow, respectively.

This coupling is very simple. The channel simulation is run throughout the channel. The velocity profiles that emerge from the channel, where the flow separates, both longitudinal and transverse velocities, are taken as input profiles for the jet simulation.

In both models the same numbers are used to nondimensionalise the quantities, so no conversion has to be done. The only thing that has to be accounted for is that the transverse domain in the jet simulation has to be much larger than that from the channel. In practice we take a transverse domain in the channel of $n_y \times dy = 250 \times 0.04$, and in the jet 500×0.16 (the factor four in dy is taken for convenience, no particular other reason). The transverse domain is the 80 times as large as that from the channel.

In order to see if the coupling works, we have compared our simulations results of the RNS equations, with a commercial code called FLUENT. This program solves the complete set of Navier Stokes equations.

3.3.1 Comparison with FLUENT

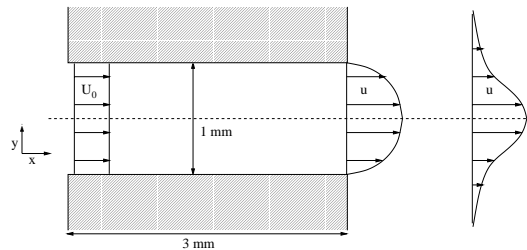


Figure 3.3: schematic drawing of the situation used to compare our model with FLUENT

For this comparison, we have simulated the flow in a short, straight channel (length: 3mm). At the end of this channel, the fluid emerges in a jet (see figure 3.3). At the inlet of the channel, the flow has a flat velocity profile of $U_0 = 10m/s$. The Reynolds number based on half the height of the channel is taken to be $Re = 666$. We present some curves calculated with the two programs in figures 3.4 and 3.5

From these four figures it can be seen the velocity profiles and the pressure drop in the channel are very much alike for the two programs. The values of the central velocity, computed by the two simulations differ only by 2% at the end of the channel, and 3% at $x = 0.025m$. This obviously justifies the assumptions and approximations which we made in order to simplify the flow model. From the pressure curve in figure 3.5 it can be seen that there are two small regions where the RNS-p(x) model is less accurate. These regions are the upstream and downstream ends of the channel. Here the pressure calculated by the RNS-p(x) simulation has a discontinuity in its gradient.

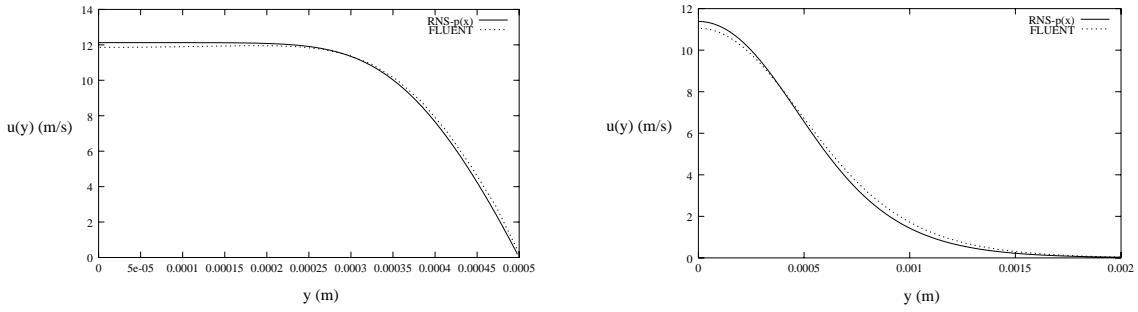


Figure 3.4: Velocity profiles $u(y)$ at the end of the short channel (left) and at 22 mm distance from the end of the channel, computed with FLUENT and the simulation of RNS-p(x) models. Vertically the longitudinal velocity is displayed in m/s , and horizontally the transversal coordinate in mm .

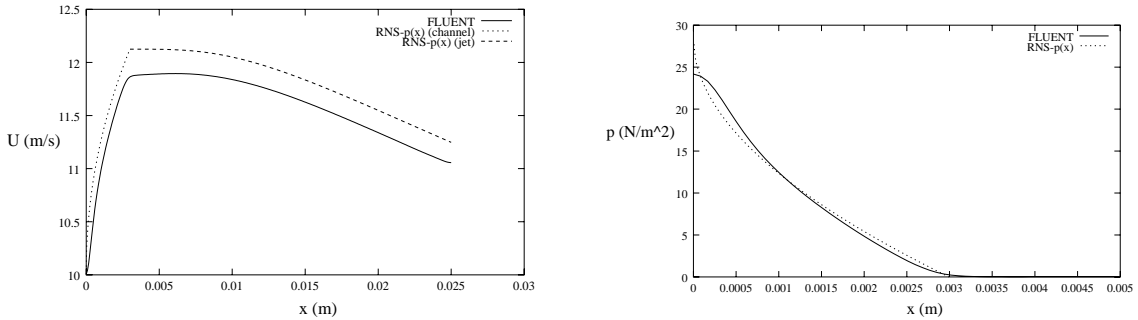


Figure 3.5: The central velocity (left) and the pressure (right) as a function of x , computed with FLUENT and the simulation of RNS-p(x) models.

But in general can be concluded that the accuracy of the model is quite reasonable compared with full Navier Stokes simulation, for the considered problem.

The great advantage of the simplified flow model presented in the report and the solution of the complete set of Navier Stokes equation is the gain of time. Typically a simulation such as discussed above, took several hours of calculation time for FLUENT, whereas the simulation of the RNS-p(x) model, only needed some minutes to obtain very close results.

Chapter 4

Application: the flue channel

The combined simulation of channel-jet flow, discussed in section 3.3, is applied on a flue channel in a mouthpiece of a recorder type flute. In figure 2.1 a picture of the flue channel that is studied is shown. At the TUE velocity profiles have been measured at various distances from the end of the channel, for several Reynolds-numbers [23]. The measurements are carried out with a hot wire. With the RNS-p(x) model simulation, we calculated velocity profiles at the same positions for those Reynolds-numbers.

In this chapter we present results of these calculations and compare those with the results of the experiments. In section 4.1 we discuss the experiments in some detail, and present an example of measured velocity profiles. After that, in section 4.2 we present the geometry which has been applied in the flue channel flow simulation. In section 4.3 we discuss the method we used in order to find the right Reynolds-number in the simulation. This number is measured with the entrance velocity, whereas in the experiments this velocity has not been measured. From the profiles, some quantities have been deduced, which are characteristic for the behaviour of the flow. In section 4.4 we present these quantities, being the pressure difference over the channel, the volume flux and the momentum flux, calculated from both experimental and simulation profiles.

We discuss the comparison of results in the next chapter 5.

4.1 Experimental results

The air which is blown into the channel is coming from a high pressure source, with a Dantec nozzle attached to it to obtain a uniform flow. This way the velocity at the entrance of the channel is constant over the transverse section of the channel within 7%. The velocity profiles have been measured at 1 mm, 1.5 mm and 2 mm downstream of the end of the channel. The measurements are carried out for various Reynolds numbers, by varying the entrance velocity ($Re_H = HU_0/\nu$). Two examples of those measurements are given in figure 4.1. Both profiles are measured at 1.5 mm downstream of the channel end, for two different Reynolds numbers. The measured velocity u_{exp} is the actual velocity, divided by the measured maximum velocity $U_{max,exp}$.

One can see in comparison of the two that the profile with the highest Reynolds number is steeper than the one with a lower Reynolds-number. This is not very surprising when we keep in mind that for lower Reynolds numbers viscous forces become more important and boundary layers will be more developed.

We remark also that at both sides the profiles have an off-set velocity. This is an effect of jet flow. The jet 'drags' surrounding air in longitudinal direction due to viscosity, and it 'draws' air towards it in transverse direction. Far from the centre of the jet there is a transport of air towards

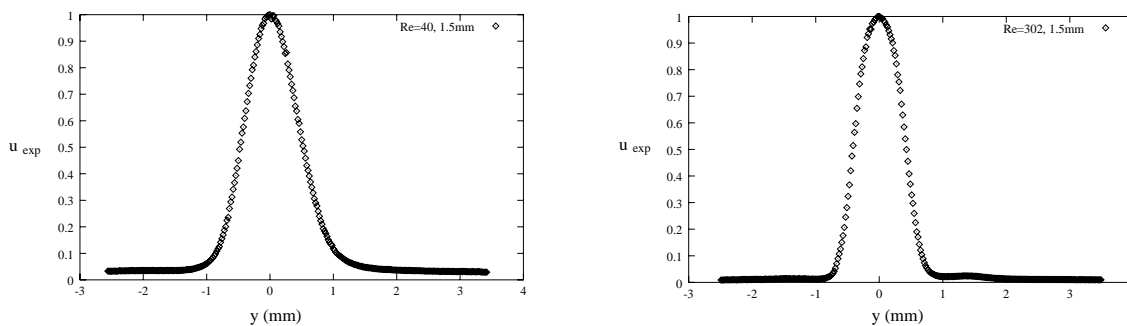


Figure 4.1: Two profiles measured in the experiments, both at 1.5 mm behind the channel. The left profile was measured with $Re_H = 40$ and the right with $Re_H = 302$. The velocities are scaled with the maximum value.

it. In velocity measurements with a hot wire one cannot distinguish between longitudinal and transverse velocity-components. So the measured velocity u_{exp} represents the quantity $\sqrt{u^2 + v^2}$, rather than only the longitudinal component. In section 4.4 we will show that the the calculated transverse velocity is in accordance with this effect.

In the right graph of figure 4.1 a 'bump' in the right part of the profile appears. This is because the hot wire itself is coming into flow and affects the measurements (see [23]). Since it seems that only the right half of the profile is affected, we will only use the left half of it. The part of the measured profiles that we will use is that for which y is inferior to the coordinate where the maximum velocity is measured.

4.2 Applied geometry

For simulation of the flue channel flow, we applied a geometry in two segments: the channel and the jet. The geometry of the flue channel has been measured by v.d. Tillaart [23]. The height of the channel at the front end is 2.2 mm (the Reynolds numbers Re_H are measured with half this height). The total length of the channel is 70.5 mm. From front to rear, the channel slowly converges to about half its height at the entrance and then it diverges quickly to about 2 mm in the last 1.25 mm. The flow separates in the divergent part of the channel. Once the flow is separated it can be treated as a freely moving jet. In appendix C it is shown that the flow separates very quickly once the channel is diverging (within about 0.5 mm). For simplicity we say the flow separates where the channel is the narrowest, at a position of 69.25 mm. From there on we apply the jet simulation. This way we neglect the effects of the flow still being attached in the divergent part.

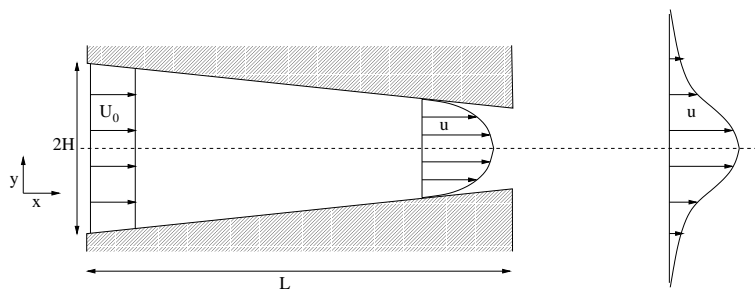


Figure 4.2: The geometry used for the flue channel flow simulation.

The geometry of the flue channel model used in the simulations is as follows: a slowly, symmetri-

cally converging channel, of which half the height decreases linearly with the longitudinal position. Without dimensions this is written as

$$h(x) = 1 - \frac{1}{2}\alpha Re_H x \quad \text{for } 0 \leq x \leq \frac{L}{H Re_H} \equiv x_{end} \quad (4.1)$$

where $H = 1.1$ mm, half the channel height at the entrance, $L = 69.25$ mm and α is given by 0.01778. This geometry is depicted in figure 4.2. From the wake end of this channel a jet emerges. The positions at which the profiles are measured in the experiments (at 1, 1.5 and 2 mm from the end of the channel) correspond to distances of 2.25, 2.75 and 3.25 mm from the wake end of the simulation model. The extra 1.25 mm is the depth of the divergent part of the channel.

Because the inlet velocity in the experiments is not known a priori, it is not obvious to determine the Reynolds number which corresponds with the different measurements.

4.3 Determination Reynolds-number

The longitudinal scale in the numerical simulation is $H Re_H$ which is a scale based on fluid dynamical behaviour: the scale on which a boundary layer of thickness H develops. The real length of the channel is thus a certain factor times this scale, to be precise, the end of the channel has the nondimensionalised coordinate: $L/H Re_H$. This proportion (thus the Reynolds-number) determines to what state the boundary layers are developed. The higher Re_H , the shorter the length of the channel appears in the nondimensionalised form and thus the less boundary layers have had the chance to develop.

In order to find the Reynolds-numbers corresponding to the measurements we first choose a more or less arbitrary Re_H (corresponding to an arbitrary inlet velocity). This gives a certain value of the central (=maximum) velocity at the places where the profiles have been measured. In comparison with the measured velocities $U_{max,exp}$, Re_H can be adjusted to obtain the same value for the central velocity (within 1%) as the experiments in an iterative process.

4.4 Comparison experimental and simulation results

In table 4.1 the results are shown of the experiments and simulation. We present quantities calculated from the velocity profiles from both experiments and simulation. The table is divided into four segments, which are explained in the following text.

I Orders of magnitude

- $U_{max,exp}$: the maximum velocity measured at the exit of the channel, at 2 mm distance,
- Re_H : the Reynolds number found in accordance with the velocity above
- $U_{0,calc}$: the entrance velocity corresponding with Re_H (flat profile),
- $\rho U_{0,calc}^2$: the normalization factor for the pressure ¹.

II The pressure difference

- Δp_{exp} : the pressure difference over the channel (front-end), measured in the experiments ²,

¹For the mass density of air we used $\rho = 1.2$ kg/m³

²The pressure difference in [23] has been measured in mm water-pressure. The conversion factor to N/mm² is $\rho_{water}g \cdot 10^{-3} = 9.8$

I							
$U_{max,exp}$ (m/s)		1.49	5.25	8.97	12.77	27.07	36.08
Re_H		40	125	212	302	667	909
$U_{0,calc}$ (m/s)		0.545	1.70	2.89	4.11	9.09	12.4
$\rho U_{0,calc}^2$ (N/m ²)		0.357	3.48	10.0	20.3	99.4	185
II							
Δp_{exp} (N/m ²)		7.8	34	75	135	541	990
Δp_{calc} (N/m ²)		7.55	31.7	67.1	115	417	709
$\left(1 - \frac{\Delta \bar{p}_{calc}}{\Delta \bar{p}_{exp}}\right) \cdot 100\%$		4	7	11	15	23	28
III							
Φ_{exp} (10 ⁻³ m ² /s)	at 1mm	1.74	4.94	7.83	11.5	25.0	33.3
	1.5mm	1.68	5.01	8.02	11.2	24.7	
	2mm	1.83	4.98	8.16	21.2	24.4	
Φ_{calc} (10 ⁻³ m ² /s)	at 1mm	1.69	4.60	7.42	10.4	21.9	29.6
	1.5mm	1.78	4.71	7.55	10.5	22.1	
	2mm	1.87	4.84	7.68	10.63	22.2	
$\left(1 - \frac{\Phi_{calc}}{\Phi_{exp}}\right) \cdot 100\%$	at 1mm	2	7	5	10	12	11
	1.5mm	7	6	6	6	11	
	2mm	2	3	6	13	9	
IV							
$\Delta_{2,exp}$ (10 ⁻³ kg/s ²)	at 1mm	2.09	21.9	60.4	131	667	1120
	1.5mm	1.96	22.4	63.0	127	643	
	2mm	2.19	21.8	64.1	123	633	
$\Delta_{2,calc}$ (10 ⁻³ kg/s ²)	at 1mm	1.91	19.8	57.0	117	561	1037
	1.5mm	2.03	20.2	57.6	117	562	
	2mm	2.14	20.6	58.2	118	563	
$\left(1 - \frac{\Delta_{2,calc}}{\Delta_{2,exp}}\right) \cdot 100\%$	at 1mm	9	9	6	11	16	8
	1.5mm	4	10	9	8	13	
	2mm	2	6	9	18	11	

Table 4.1: Experimental and calculated properties of the flow through the flue channel

- Δp_{exp} : the same quantity calculated in the simulation times its dimension factor $\rho U_{0,calc}^2$,
- the relative difference between the experimental and calculated pressure differences.

III The 'volume flux'

- Φ_{exp} : the 'volume flux' calculated from the measured velocity profiles at various distances from the rear end of the channel (indicated in the first column). The flux is calculated from the data by:

$$\Phi_{exp} = 2 \sum_j u_{exp,j} U_{max,exp} dy$$

where we integrated over half the profile up to where it reaches its maximum velocity (see below for explanation),

- Φ_{calc} : the 'volume flux' calculated from the flue channel simulation profiles:

$$\Phi_{calc} = 2 \sum_j \sqrt{u_j^2 + \frac{v_j^2}{Re_H^2}} U_{0,calc} H dy$$

where we also integrated over half the profile,

- the relative difference between the experimental and calculated flux.

The volume flux derived from the experimental results is the integration of the measured velocity profile. The measured u_{exp} represents the quantity $\sqrt{u^2 + v^2}$, rather than only the longitudinal component. In figure 4.3 a measured jet profile is shown, together with the corresponding, calculated profiles of longitudinal velocity and the absolute value of both longitudinal and transverse components ($\sqrt{u^2 + v^2}$). For the measured profile an off-set velocity appears, which is about 3%

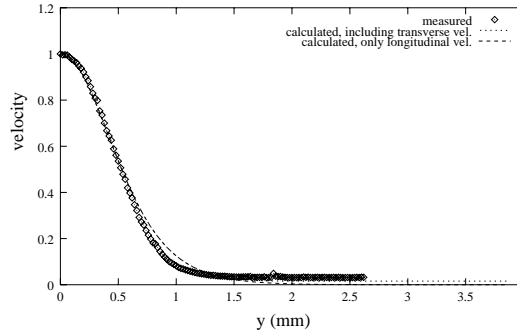


Figure 4.3: The used half of the measured velocity profile (flipped horizontally) and the corresponding calculated profile of only the longitudinal component, and the total velocity $\sqrt{u^2 + v^2}$. The profiles are measured/calculated at 2mm downstream of the channel end, at $Re_H = 40$

of its maximum value, which means 5×10^{-2} m/s. In the figure it can be seen that the longitudinal component of the calculated velocity alone does not have an off-set. Inclusion of the transverse velocity improves approximation of the measured profile. The calculated transverse velocity at the right limit of the profile is about 2×10^{-2} m/s.

Therefore in the integration of the calculated 'volume flux' we added the squared transverse velocity in the integration. Note that the calculated longitudinal velocity is scaled with $U_{0,calc}$, the transverse velocity is scaled with $U_{0,calc}/Re_H$.

In order to obtain the experimental 'volume flux' we integrated one half of the experimental profiles up to the maximum, using all data-points for which the y coordinates are inferior to this one. If we look at the measured profile in figure 4.3 we see that the off-set velocity is more or less constant over about one mm. There is no reason a priori why we should not integrate the profile up to $y = 1.5$ mm, for instance, instead of the last data point. The choice of the integration limit will affect the results. If we integrate to $y = 2$ mm we find a volume flux which is 2% smaller than the one by integration over the total domain.

We integrated the calculated profiles up to the last data point as well. This corresponds in figure 4.3 with the limit $y = 3.8$ mm. Integration up to $y = 3$ mm decreases the calculated volume flux by 2%. Taking the same integration limits for both measured and calculated results would be a lot more elaborate, for we have to determine it for every profile separately. Moreover this will not improve the results given in table 4.1 because we would have to shorten the limits for the calculated profiles. This will cause the calculated 'volume flux' to decrease, while they are already inferior to the experimental results.

IV The 'momentum flux'

- $\Delta_{2,exp}$: the 'momentum flux' calculated from the measured velocity profiles at various distances from the rear end of the channel (indicated in the first column), according to:

$$\Delta_{2,exp} = 2\rho \sum_j u^2 U_{max,exp}^2 dy$$

where we integrated over half the profile up to where it reaches its maximum velocity,

- $\Delta_{2,calc}$: the momentum flux calculated from the flue channel simulation profiles:

$$\Delta_{2,calc} = 2\rho \sum_j \left(u_j^2 + \frac{v_j^2}{Re_H^2} \right) U_{0,calc}^2 H dy$$

where we also integrated over half the profile,

- the relative difference between the calculated and measured momentum flux.

Generally, the sum of the longitudinal velocity times the density would give the momentum flux in the x direction. Since in the experiments $\sqrt{u^2 + v^2}$ is measured, rather than the separate components, we added the transverse velocity in the sum of the momentum flux as well.

For the 'momentum flux' the choice of the integration domain has less influence on the results than for the 'volume flux'. Integration of the experimental profile up to $y = 2$ mm would decrease this flux only by 0.1%. The 'momentum flux' decreases also by 0.1% if we integrate the calculated profile up to $y = 3$ mm. So here the integration limits are not at all important, as long as they lie in the region where the velocity profile is constant.

Chapter 5

Discussion

We have shown that the channel flow simulation (see section 3.1.3), and the jet flow simulation (see section 3.2.3) are quite accurate when compared with analytical and approximate solutions of the boundary layer theory in specific cases.

In the section 3.3.1 we have shown that the simulation of the flow in a straight channel with an emerging jet, using our simplified RNS-p(x) model, predicts within 3% the results of the commercial code FLUENT which solves the complete two dimensional Navier Stokes equations. The regions where the RNS simulation is less accurate are those close to the entrance and exit of the channel. Here a discontinuity appears in the pressure gradient. This discontinuity is due to the simplifications, which are not justified in those regions. At the entrance of the channel, for example, where the boundary layer is very thin, we cannot neglect the transverse pressure gradient in the boundary layer. Very close to the wall at the entrance the full set of Navier Stokes equations should be solved.

At the end of the channel, the discontinuity of the pressure gradient could be due to the absence of downstream information in the simulation. Normally in sub-sonic flows, which is here the case, information of perturbations, abrupt changes in geometry etc. are carried upstream because these perturbations travel with the speed of sound. The numerical solution of the RNS-p(x) model only takes upstream information into account, so logically no effects of the abrupt end of the channel are sensed in the channel itself.

The great advantage of simulation of the RNS-p(x) flow model instead of full Navier Stokes simulation is the gain of calculation time. For the problem discussed in section 3.3.1 FLUENT took several hours of calculation, while the RNS-p(x) simulation took only several minutes. The exact difference has not been measured and depends of course on the number of points in the domain, the desired precision of results of FLUENT.

In chapter 4 we presented the results of the flow simulation in a flue channel in comparison with experimental results. In figure 5.1 the relative difference between the measured and the calculated pressure difference over the channel is plotted against the Reynolds-number. The difference increases with the Reynolds-number, which is possibly caused by turbulence. One of the effects of turbulence is flattening of the velocity profile, causing a decrease of the maximum velocity with respect to laminar flow. Since we fitted the maximum velocity in the jet, we would underestimate the Reynolds number of the flow and thus the pressure difference.

In figure 5.2 the relative difference between simulation and experimental results for both the 'volume flux' and the 'momentum flux' are given for different Reynolds-numbers. As mentioned in the previous section, in the experiments the quantity $\sqrt{u^2 + v^2}$ is measured, rather than u and v separately. For the simulation results, we thus calculated the 'volume' and 'momentum' fluxes based on $\sqrt{u^2 + v^2}$, instead of the exact definition based on u only. So we did not calculate the

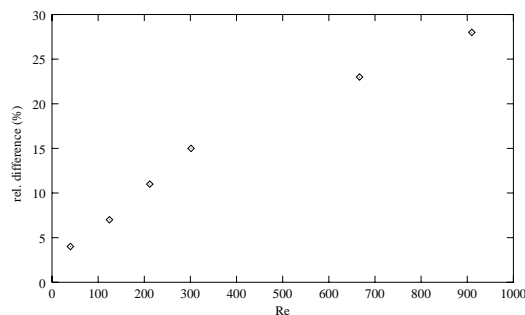


Figure 5.1: The relative difference between the calculated and measured pressure difference over the flue channel.

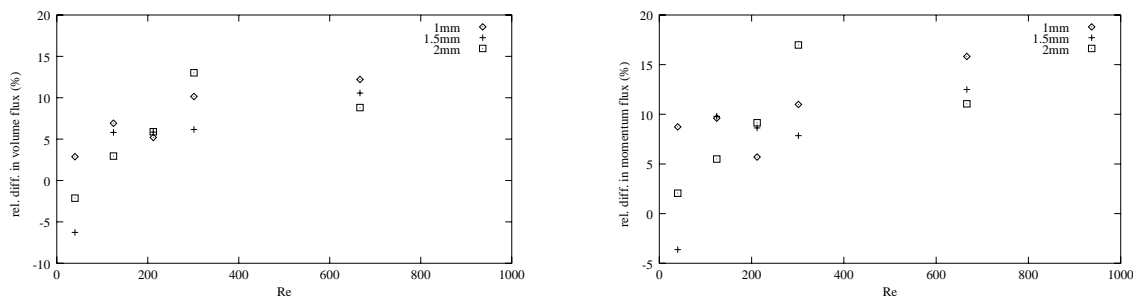


Figure 5.2: The relative difference between the calculated and the experimental 'volume flux' (left) and the momentum flux (right) for different Reynolds-numbers, at three distances from the wake end of the flue channel, indicated in the upper right corner.

real volume and momentum flux, rather a related quantity. We note that in general the relative difference is positive, which means that the experimental results are greater than the calculated results, which is also the case for the pressure difference. The increase of the difference in the volume flux as a function of Re_H (figure 5.2) could also be caused by underestimation of the Reynolds number. This logically implicates an underestimation of the volume flux.

The difference between the calculated and measured 'momentum flux' has more or less the same tendency as a function of Re_H as the difference for the 'volume flux'. Though we the discrepancy in the differences calculated at 1 mm, 1.5 mm and 2 mm is larger than that for the 'volume flux'. Probably this is due to squaring the velocities to obtain the 'momentum flux', which increases systematic errors made in the value of the velocity.

As we already explained in the previous section the choice of the domain used for integration of the profiles in order to obtain the 'volume' and 'momentum' fluxes, affects the results. We have quantified this for the case of $Re_H = 40$ at 2 mm downstream the wake end of the channel. If we shorten the domain by one fifth, at the edge of the profile where the velocity is the constant 'off-set velocity', we decrease both experimental and calculated 'volume fluxes' with 2%. This reduction of the domain decreases the 'momentum flux' by only 0.1%. This is logically smaller than the 'volume flux' reduction because we squared the velocities, suppressing the smallest values, those at the edges of the profile.

Generally the transverse domains of the calculated profiles are 3.8 mm wide, whereas the measured profiles have a domain of roughly 2.5 mm, which vary for every profile within 1 mm. Choosing exactly the same domain for each profile would be very elaborate which could make a difference of about 3% for the 'volume flux' (shortening the domain by 30% will decrease the value with 3%). Moreover, for the 'momentum flux' the difference will be much less (about 0.2%). For this reason we did not adjust the integration domains.

We conclude that the model for simulation of channel and jet flow that there is a rather good match with analytical models and full Navier Stokes simulation in particular cases. There is about 10% difference between quantities calculated by simulation and experiments.

Part II

Unsteady channel flow

Introduction

In part 2 of this report we present our model of the flow through and the motion of the vocal folds. The flow is described with a two-dimensional unsteady channel flow model, which is based on the steady channel flow model in part 1 of this report. This flow model is combined with a very simple single-mass-spring model describing the motion of the channel wall, which represents the vocal folds. The behaviour of the hydrodynamic pressure on the vocal fold oscillation is studied.

In chapter 6 we present the unsteady channel flow model which is based in the Navier Stokes equations. The accuracy of this model is shown by applying the model on two known problems. After that we present the numerical method which is used to solve the flow model, in chapter 7.

In chapter 8 we use this flow model to simulate vibration of the vocal folds, which are represented by a simple one-mass spring model. Lastly we discuss the results of the simulation model for unsteady flow.

Chapter 6

The model

In this chapter we present the model for unsteady channel flow. The goal is to describe the mechanics of an unsteady fluid flow through a channel of which the geometry is changing in time. At the same time we want to describe the motion of the channel wall. These models will be combined in an autonomous simulation of the vocal folds oscillation.

The derivation of the equations describing the unsteady fluid flow is analogous to the one in the first part of this report for the RNS-p(x) model. The unsteady model is presented in section 6.1. We show its accuracy by comparing its solution with analytical solutions of two particular problems: the Rayleigh problem and a periodic perturbation of Poiseuille flow, in section 6.1.2.

The geometry of the channel is, like in the first part, two dimensional and symmetric with respect to the centre line. In the unsteady flow model we allow (a part of) the wall of the channel to deform in vertical direction only, see figure 6.1. In the simulation of the vocal folds, which is explained in chapter 8, the mechanics of the mobile part is described with a mass-spring equation. In section 6.2 we discuss to some detail the mechanical model which we used to describe the mechanics of the wall.

6.1 Unsteady channel flow

For this model we reduce the full Navier Stokes equations (2.1) in practically the same way as in section 2.1. Again we constrict our view to small scales and small velocities in comparison with acoustics. So we can assume incompressible flow. We study the flow in a two-dimensional channel with a movable wall, as depicted in figure 6.1

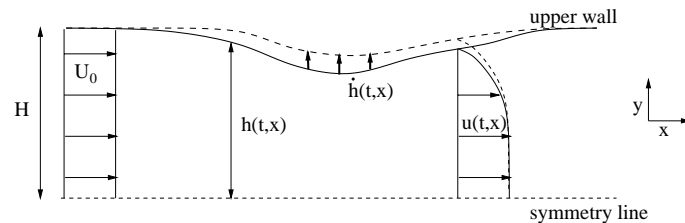


Figure 6.1: The channel geometry for the unsteady flow model.

Now we permit the velocities to change in time, so we want to keep the unsteady term $\partial u/\partial t$. Since the geometry is still a channel we will apply the same scales for x , y , u and v (equations (2.5) through (2.9)). Again we assume the pressure to be constant across the section of the channel.

So, mass conservation is still the same:

$$\frac{\partial u}{\partial x} + \frac{\partial v}{\partial y} = 0 \quad (6.1)$$

Conservation of momentum in the x direction gives:

$$\frac{\partial u}{\partial t} + u \frac{\partial u}{\partial x} + v \frac{\partial u}{\partial y} = -\frac{\partial p}{\partial x} + \frac{\partial^2 u}{\partial y^2} \quad (6.2)$$

and we still have

$$\frac{\partial p}{\partial y} = 0 \quad (6.3)$$

from conservation of momentum in y direction. The three equations given above are also known as the Prandtl boundary layer equations [19, Ch 7].

Note that in equation (6.2) we implicitly applied a time scale to nondimensionalise the equation. The time derivative of u is as important as all other terms in that equation (order 1). In order to keep this term we are forced to choose $U_0 f = U_0^2 / HRe_H$, where f is the frequency (we assume, of course, harmonic perturbations). This gives the order of magnitude of the frequency:

$$f = \frac{\nu}{H^2} \quad (6.4)$$

When we take H in the order of mm, the frequencies are in the order of 10^1 Hz. The frequency of audible sound is:

$$20Hz < f < 20kHz \quad (6.5)$$

For these frequencies the term $\partial u / \partial t$ will be at least of order 1.

The boundary conditions are again straightforward. Again we regard only symmetric solutions. We apply the no slip condition and thus demand that the fluid moves with the same velocity as the wall. Since the wall motion is only in the transverse direction, the boundary conditions are simply:

$$\begin{aligned} u &= 0 \quad \text{at} \quad y = h(t, x) \\ v &= \frac{\partial h}{\partial t} \quad \text{at} \quad y = h(t, x) \\ v &= \frac{\partial u}{\partial y} = 0 \quad \text{at} \quad y = 0 \end{aligned} \quad (6.6)$$

For simplicity in numerical solution we will again transform the transverse coordinate in order to obtain that y varies between 0 and 1.

6.1.1 'Dynamic' scaling

We thus transform the coordinates: $\tau = t$, $\xi = x$ and $\eta = y/h(x)$:

$$\frac{\partial}{\partial t} = \frac{\partial \tau}{\partial t} \frac{\partial}{\partial \tau} + \frac{\partial \xi}{\partial t} \frac{\partial}{\partial \xi} + \frac{\partial \eta}{\partial t} \frac{\partial}{\partial \eta} = \frac{\partial}{\partial \tau} - \frac{\eta}{h} \frac{\partial h}{\partial t} \frac{\partial}{\partial \eta} \quad (6.7)$$

$$\frac{\partial}{\partial x} = \frac{\partial \tau}{\partial x} \frac{\partial}{\partial \tau} + \frac{\partial \xi}{\partial x} \frac{\partial}{\partial \xi} + \frac{\partial \eta}{\partial x} \frac{\partial}{\partial \eta} = \frac{\partial}{\partial \xi} - \frac{\eta}{h} \frac{\partial h}{\partial x} \frac{\partial}{\partial \eta} \quad (6.8)$$

$$\frac{\partial}{\partial y} = \frac{\partial \tau}{\partial y} \frac{\partial}{\partial \tau} + \frac{\partial \xi}{\partial y} \frac{\partial}{\partial \xi} + \frac{\partial \eta}{\partial y} \frac{\partial}{\partial \eta} = + \frac{1}{h} \frac{\partial}{\partial \eta} \quad (6.9)$$

Substituting these equations (6.1) and (6.2) and rename τ with t , ξ with x and η with y , we obtain:

$$\frac{\partial u}{\partial x} - \frac{y}{h} \frac{\partial h}{\partial x} \frac{\partial u}{\partial y} + \frac{1}{h} \frac{\partial v}{\partial y} = 0 \quad (6.10)$$

for continuity, which is still the same as in the steady case. The x momentum equation becomes:

$$\frac{\partial u}{\partial t} - \frac{y}{h} \frac{\partial h}{\partial t} \frac{\partial u}{\partial y} + u \frac{\partial u}{\partial x} - \frac{uy}{h} \frac{\partial h}{\partial x} \frac{\partial u}{\partial y} + \frac{v}{h} \frac{\partial u}{\partial y} = -\frac{\partial p}{\partial x} + \frac{1}{h^2} \frac{\partial^2 u}{\partial y^2} \quad (6.11)$$

As boundary conditions we apply no slip and an impermeable wall (no suction or injection).

$$\begin{aligned} u &= 0 \quad \text{at} \quad y = 1 \\ v &= \frac{\partial h}{\partial t} \quad \text{at} \quad y = 1 \\ v &= \frac{\partial u}{\partial y} = 0 \quad \text{at} \quad y = 0 \end{aligned} \quad (6.12)$$

where $y = 0$ thus corresponds with the central symmetry line, and $y = 1$ with the upper channel wall.

To show the accuracy of this set of equations we will apply them to two rather well known problems which have analytical solutions.

6.1.2 Solutions

One problem that can be studied with this set of equations is the Rayleigh problem.

The Rayleigh problem

In this problem the growth of boundary layers is studied in a channel which is set to motion abruptly, or viewed another way: initially the channel is filled with fluid, having a uniform longitudinal velocity. If we apply this problem to a flat plate, which is put into a uniform flow field of velocity U_0 , we have to solve the equation:

$$\frac{\partial u}{\partial t} = \frac{\partial^2 u}{\partial y^2} \quad (6.13)$$

The boundary conditions of this problem are:

$$\begin{aligned} u &= 0 \quad \text{at the wall} \\ u &= 1 \quad \text{infinitely far from the wall} \end{aligned} \quad (6.14)$$

Initially, we put the velocity $u = 1$ everywhere. The solution of this problem is (see Schlichting [19, Ch 5]):

$$u = \operatorname{erf} \left(\frac{y}{2\sqrt{t}} \right) \quad (6.15)$$

This profile is self-similar, like the Blasius solutions for steady boundary layers. The factor \sqrt{t} is the rate of growth for the boundary layer, displacement and other thicknesses.

Every point which has coordinate $x < t$ the information from the entrance of the channel has arrived in flow. At the entrance the flow remains uniform and of constant velocity, so from there a steady boundary layer will develop as in Blasius' theory. For those points the boundary layer thus relaxes to the value given by the steady solution in section 2.1.4.

In figure 6.2 a plot is shown of the growth of the displacement thickness in the channel as a function of time. We see that the displacement thickness grows, as predicted in the analytical solution, with factor \sqrt{t} : $\delta_1(t = 0.01) \simeq 0.1$, $\delta_1(t = 0.04) \simeq 0.2$ and at $t = 0.1$ we have $\delta_1 \simeq 0.3$. When t increases the displacement thickness approaches the steady solution (see section 2.1.4).

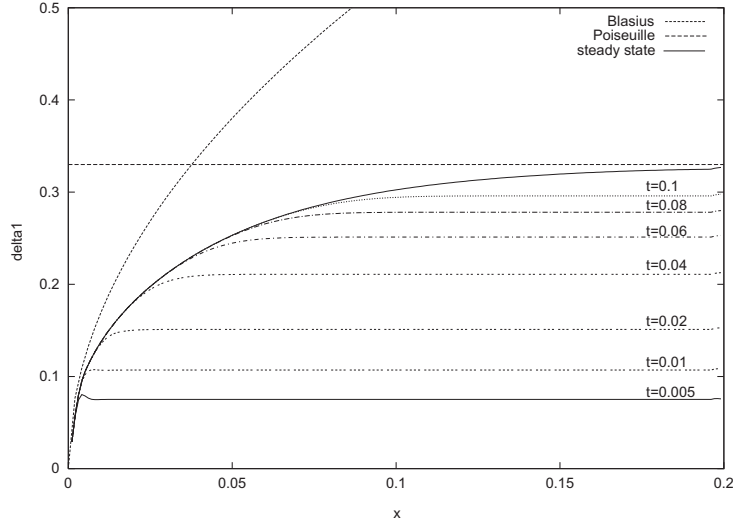


Figure 6.2: The solution of the Rayleigh problem. The growth of the displacement thickness δ_1 is plotted against x for several time steps. The solution tends to the steady channel flow.

Periodically perturbed Poiseuille flow

Another problem which can be solved with the model above is a periodical perturbation of Poiseuille flow. We study solutions of the equation:

$$\frac{\partial u}{\partial t} = -\frac{\partial p}{\partial x} + \frac{\partial^2 u}{\partial y^2} \quad (6.16)$$

with boundary conditions $u(t, -1) = u(t, 1) = 0$. We impose oscillation of the pressure gradient:

$$\frac{\partial p}{\partial x} = K e^{i\omega t} \quad (6.17)$$

We look for solutions in the form $u(y, t) = u(y) \exp(i\omega t)$. Substituting this into the equation, it becomes:

$$i\omega u - K - \frac{\partial^2 u}{\partial y^2} = 0 \quad (6.18)$$

The general solution is:

$$u(y) = \frac{iK}{\omega} \left(1 - \frac{2e^{\sqrt{i\omega}} \cosh(\sqrt{i\omega}y)}{e^{2\sqrt{i\omega}} + 1} \right) \quad (6.19)$$

from which it can be seen that the ratio of amplitude of u and the pressure decreases proportional to ω^{-1} .

This behaviour is visualized in figure 6.4. The geometry of the channel is straight (length= 0.3) with a small, oscillating bump near the entrance. This bump is Gaussian shaped, centered at $x = 0.025$, width $1/120$ and a height of 0.3. In figure 6.3 the situation is captured at a certain moment. The position of the upper wall of the channel, the wall shear stress and the velocity on the centre line are displayed, as well as some longitudinal velocity profiles throughout the channel. The restriction causes an acceleration in the flow, and right after the bump there is a region of separation, as can be seen from the wall shear stress curve, and the velocity profile at $x = 0.03$ in the right figure.

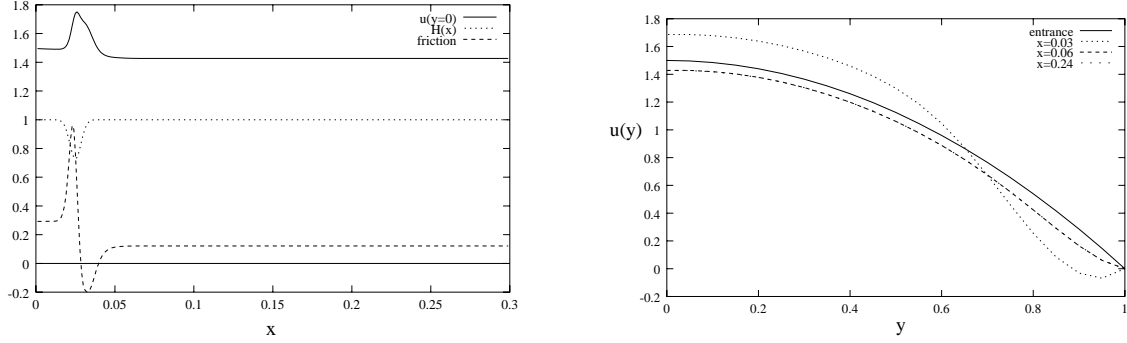


Figure 6.3: The geometry of the channel, the central velocity and the wall shear stress (divided by 10) in the channel at a given moment (left) and longitudinal velocity profiles at four different places in the channel (right).

This bump oscillates with $\omega = 100$ and 200 , generating the oscillations in the Poiseuille profile and the pressure gradient. In figure 6.4 the velocity on the centre line and the pressure gradient at the end of the channel are traced as a function of time. The amplitude of dp/dx is roughly a factor ω times the amplitude of U . From equation 6.19 we can calculate the phase difference between the pressure gradient and the maximum velocity. For both frequencies we obtain a phase difference of about 0.4π , which is in accordance with the curves in the figure.

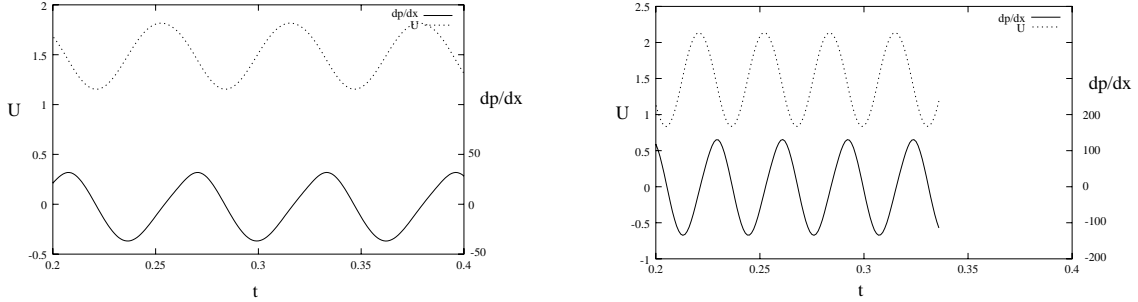


Figure 6.4: The velocity on the centre line U (left scale) and the pressure gradient (right scale) at the end of the channel as a function of time, in response to an oscillating small bump in the wall. In the left figure the bump oscillates with frequency 100, in the right 200.

For very low frequencies $\omega \rightarrow 0$ we find the steady Poiseuille flow. By writing out a Taylor development of all exponentials (N.B. $\cosh(x) = 1/2(e^x + e^{-x})$) up to order ω , we find:

$$\lim_{\omega \rightarrow 0} u(y) = \frac{K}{2} (1 - y^2) \quad (6.20)$$

where K is the steady pressure gradient, in comparison with equation (2.28).

6.2 Wall motion

In the discussion of the flow model we already mentioned that we allow the wall to move. For the sake of simplicity, this motion is restricted to the transverse sense only. The mobile part of the channel wall will represent the vocal folds. In our model we will describe the mechanical behaviour of the vocal folds with a simple one-mass-spring system. In figure 6.5 this model is visualized.

A mass m is positioned in an envelope representing the channel wall, which has the shape of a cosine. It is suspended with a spring of stiffness k in a rigid frame and a damper with damping

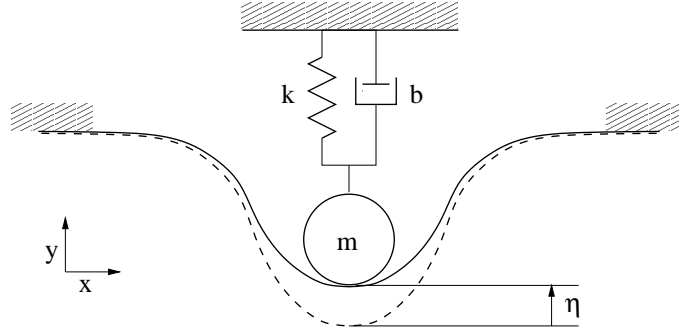


Figure 6.5: The mass-spring model for wall motion.

constant b . When applied on the vocal folds, m represents its inertia, the spring represents the stiffness of the surrounding tissue, and the damper the internal dissipation. We define the function $\eta(t)$ which represents the displacement of the mass at a certain time t with respect to the initial position η_0 , the dashed curve in figure 6.5.

The equation of mechanical equilibrium is:

$$m \frac{\partial^2}{\partial t^2} \eta(t) + b \frac{\partial}{\partial t} \eta(t) + k \eta(t) = f(t) \quad (6.21)$$

where $f(t)$ is an external force which is applied on the mass in the positive y direction. This force will be the hydrodynamic force on the wall, when we apply this model on the vocal folds.

This mass-spring model is undoubtedly a far too simple representation of the vocal folds. But we will see that this model already has an interesting behaviour. And since the hydrodynamic behaviour is our main point of interest, we would better keep the vocal folds model as simple as possible. However, the wall model can easily be generalized to a model of a one dimensional membrane with a longitudinal tension, suspended by springs of stiffness k per unit length. In appendix D we present the general wall model which could be applied in future work.

The mechanical behaviour of our model is solved numerically by a method which is called the Newmark method. The special advantage of this method is that it is unconditionally stable, independent of the value of the parameters. We will discuss this method briefly in the next chapter. More details are given in appendix D.

Chapter 7

Numerical method

In this chapter we present the numerical method used for solution of the unsteady flow model, as well as the mass-spring model for wall motion.

First, in section 7.1 we present the discrete approximation of the unsteady RNS-p(x) equations from section 6.1. And write out its solution step by step. The accuracy and stability are briefly discussed in section 7.1.2.

In section 7.2 we present the discrete equation of motion of the mass-spring wall model which is the Newmark approximation. It is solved by a prediction-correction technique, explained in 7.2.2.

Presenting the solution of the steady channel flow model in chapter 3, we mentioned that in the simulation we start with a given velocity profile (volume flux) at the entrance. The channel flow simulation calculates the velocity field and the pressure difference over the channel. We thus impose a constant flux as a flow source. In simulation of the airflow through the larynx we assume this way the lungs, from which the air arrives at the larynx, to be a source of volume flux. This does not seem to be very realistic. We also implemented a pressure source model for the lungs in our simulation. In stead of imposing a flux we then impose a pressure drop over the length of the channel. The numerical realization of both 'lung' models will be discussed in the next section.

7.1 Channel flow

The time derivative of the longitudinal velocity will be included in the straightforward way:

$$\frac{\partial u_{i,j}}{\partial t} = \frac{u_{i,j}^{n+1} - u_{i,j}^n}{\Delta t} \quad (7.1)$$

where n denotes the instant $t = t_n$. This term, together with a term from the time derivative of the wall position function $h(t, x)$ will be added to the steady momentum equation (3.1.1). All terms appearing in the equation will be defined implicitly, thus at $t = t_{n+1}$, except for the old velocity term in the time derivative, of course. The main idea of solving the unsteady channel flow model is that for every instant t_n , we solve for the flow on the whole domain in the channel in the same way as we did in steady channel flow, after which we pass on to the next instant t_{n+1} .

The approximation of the time dependent equation of momentum in x -direction, equation (6.11),

has the form:

$$\begin{aligned}
& \frac{u_{i+1,j}^{n+1} - u_{i+1,j}^n}{\Delta t} - \frac{y_j}{h_{i+1}^{n+1}} \dot{h}_{i+1}^{n+1} \frac{u_{i,j+1}^{n+1} - u_{i,j-1}^{n+1}}{2\Delta y} \\
& + u_{i,j}^{n+1} \frac{u_{i+1,j}^{n+1} - u_{i,j}^{n+1}}{\Delta x} + \frac{1}{h_{i+1}^{n+1}} \left(v_{i,j}^{n+1} - u_{i,j}^{n+1} y_j \frac{h_{i+1}^{n+1} - h_i^{n+1}}{\Delta x} \right) \frac{u_{i,j+1}^{n+1} - u_{i,j-1}^{n+1}}{2\Delta y} \\
& = -\frac{p_{i+1}^{n+1} - p_i^{n+1}}{\Delta x} + \frac{u_{i+1,j+1}^{n+1} - 2u_{i+1,j}^{n+1} + u_{i+1,j-1}^{n+1}}{(h_{i+1}^{n+1} \Delta y)^2}
\end{aligned} \tag{7.2}$$

where \dot{h}_i^n is the vertical velocity of the wall at $t = t_n$ and $x = x_i$. In this equation the unknowns are the ones with both high index $n + 1$ and low index $i + 1$, the rest is from the precedent step in x or in t which are known. However, the height of the channel h_{i+1}^{n+1} is a known function at time t_{n+1} for all x_i . We do not solve it in the channel flow simulation, it is given externally. In case we impose the wall motion (like in the solution of the perturbed Poiseuille flow, section 6.1.2) it is given for all t_n and x_i . In the combined simulation as applied for simulation of the vocal folds it is calculated by the wall motion simulation. The exact coupling will be explained in chapter 8.

In comparison with equation (3.1.1), the discrete form of the momentum equation in steady flow, one can see that nothing has changed when it comes to approximation of derivatives.

The boundary conditions for the longitudinal velocity are conform (6.12):

$$\begin{aligned}
u_{i+1,1}^{n+1} - u_{i+1,0}^{n+1} &= 0 \\
u_{i+1,ny}^{n+1} &= 0
\end{aligned} \tag{7.3}$$

Once we have solved for \mathbf{u}_{i+1}^{n+1} we integrate the continuity equation to obtain \mathbf{v}_{i+1}^{n+1} . This equation has not changed with respect to the steady flow model, it is exactly equal to (3.7) at time t_{n+1} :

$$\frac{v_{i+1,j+1}^{n+1} - v_{i+1,j}^{n+1}}{\Delta y} = -h_{i+1}^{n+1} \frac{u_{i+1,j+1}^{n+1} - u_{i,j+1}^{n+1}}{\Delta x} + y_j \frac{h_{i+1}^{n+1} - h_i^{n+1}}{\Delta x} \frac{u_{i+1,j+1}^{n+1} - u_{i+1,j}^{n+1}}{\Delta y} \tag{7.4}$$

The discrete form of the boundary conditions for v , from equation (6.12), are:

$$\begin{aligned}
v_{i+1,0}^{n+1} &= 0 \\
v_{i+1,ny}^{n+1} &= \dot{h}_{i+1}^{n+1}
\end{aligned} \tag{7.5}$$

So far, there is no difference in the method between an imposed volume flux and imposed pressure drop. This difference will come forward in the exact path followed for solution of the set.

7.1.1 Solution

The solution of the set of equations presented above is to the solution of that in the model of steady channel flow. For both the imposed flux and the imposed pressure difference we follow the schedule described below.

At $t = 0$ we fill the channel with a certain velocity field. This may be a uniform flow or Poiseuille flow or something like that, for we need an initial condition for the whole velocity field. At the channel entrance we keep $p_0 = 0$ for all t_n .

Estimation of p_{i+1}^{n+1}

The solution starts with an estimation of the new pressure. Unlike the steady flow model, however, here we choose just the precedent pressure instead of extrapolate it from the curve. For some unknown reason, the extrapolation gives awkward results in the calculated, new pressure function.

Calculation of \mathbf{u}_{i+1}^{n+1}

Next, we solve equation (7.1) for \mathbf{u}_{i+1}^{n+1} . All terms having both indices $n + 1$ and $i + 1$ are moved to the left hand side, in order to put the equation in the form

$$\mathbf{A}\mathbf{u}_{i+1}^{n+1} = \mathbf{b} + \left. \frac{dp}{dx} \right|_{i+1}^{n+1} \quad (7.6)$$

where \mathbf{A} is a tridiagonal matrix and \mathbf{b} contains terms from precedent calculation steps. This matrix is inverted using the method of factorization.

Calculation of \mathbf{v}_{i+1}^{n+1}

After that, we solve for the new transverse velocity by integrating the equation of continuity exactly analogous to the steady model (see section 3.1.2). At the upper wall, we have to find v equal to the transverse velocity of the wall. Like in the steady model, this will generally not be the case with the estimated pressure from above. In a Newton iteration on the pressure value, the discrepancy between the transverse velocity of the wall and of the fluid are decreased to 10^{-9} .

Newton iteration on the pressure

This iteration process is analogous to the one applied in steady flow (section 3.1.2). The difference with the steady channel flow model is that now we are not looking for the zero of the function $v_{ny}(p)$, but simply for the root of $v_{ny}(p) - \dot{h}$. The derivative of $v_{ny}(p)$ is determined (note that this is the same as the derivative of this function translated over \dot{h}). The next pressure value will be equal to

$$p_{new} = p_{old} - \frac{v_{ny}(p_{old}) - \dot{h}}{\delta v / \delta p} \quad (7.7)$$

and we iterate this way on the new value of the pressure, solving \mathbf{u}_{i+1}^{n+1} and \mathbf{v}_{i+1} each time. This iteration will be continued until the transverse velocity of the fluid and the wall differ less than 10^{-9} .

When this condition is satisfied, we move one step in the positive x direction, until we arrive at n_x . In case we imposed constant volume flux, we now pass on to the next instant, and start the solution from x_0 . In case we imposed a constant pressure drop over the channel, the difference with the constant flux comes forward.

Imposed pressure drop

When the pressure drop is imposed, we vary the flux at the entrance of the channel in order to get the desired pressure at the end. We thus search for the amplitude of the entrance velocity profile. This search is done with another Newton iteration.

Newton iteration on the entrance flux

First, we give a volume flux at the entrance of the channel: $\Phi = \sum_j (\mathbf{u}_0^n)$, which will be taken equal to 1. We do the whole calculation above, starting from 'Estimation of p_{i+1} ' to the end of the Newton iteration on the pressure, for the **whole** channel. This gives us a certain value of the pressure at the end of the channel, and thus the pressure drop. We determine the derivative of

that pressure drop as a function of the flux, by repeating the calculation above for $\Phi + \epsilon$ and $\Phi - \epsilon$, taking the difference and divide it by 2ϵ .

The new value of the flux is that obtained by extrapolation of the pressure drop as a function of the volume flux $\Delta p(\Phi)$ to the imposed pressure drop.

$$\Phi_{new} = \Phi_{old} - \frac{\Delta p(\Phi_{old}) - \Delta p_{imp}}{\partial \Delta p / \partial \Phi} \quad (7.8)$$

This iteration is repeated until the difference between the calculated and the imposed pressure drop is less than 10^{-9} .

Summarizing, in case of imposed pressure drop we add a feedback loop in the simulation modifying the entrance flux, after having solved the whole velocity field, at one instant $t = t_n$. The difference between the two methods is visualized in figure 7.1.

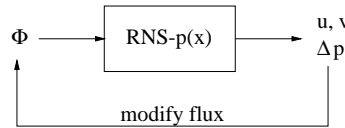


Figure 7.1: Visualization of the solution in case of imposed pressure difference over the channel. The effect, with respect to imposed flux, is an extra loop in which the entrance velocity is modified in order to get the desired pressure drop.

After having solved for the whole channel we pass on to t_{n+1} , and start again from the beginning.

7.1.2 Accuracy and stability

For the accuracy of the unsteady channel flow model we have shown in section 6.1.2 that the Rayleigh problem and harmonic perturbation of fully developed flow are solved properly.

In the solution of the Rayleigh problem we traced the growth of the displacement thickness in time. In figure 6.2 it can be seen that this growth is indeed in accordance with the analytical solution and that the curve relaxes to the steady state solution for channel flow.

For harmonic perturbation of Poiseuille flow we have shown that the phase factor and the amplitude ratio of the velocity and the pressure gradient are in accordance with the analytical solution.

The stability of this simulation is comparable to that of the steady channel flow simulation. This is because we only added the term $\partial u / \partial t$ with respect to that model. Numerically, we defined most terms implicitly, which often has a stabilizing effect (see appendix B). We have not studied the stability of this simulation thoroughly. But we expect the same behaviour as the steady channel flow simulation, with additional conditions for the choice of Δt . The simulation of the Rayleigh problem (see section 6.1.2) has been rerun for several values of Δt . For this problem the code seems to be stable even for $\Delta t = 0.5$.

7.2 Wall motion

The discretisation of the vertical displacement of the mass in our wall motion model is very simple, we write: $\eta^n = \eta(t = t_n)$.

For the approximation of the equation of mechanical equilibrium (6.21) we use the approximation from the Newmark method. This method is a numerical method for solution of mass-spring like systems. In appendix D.2 and in [7] this method is discussed in more detail. Here we will only highlight some important features.

7.2.1 Discrete equations

The Newmark method is a one-step integration method, so we have to decompose the derivative $\partial^2/\partial t^2$ into two derivatives of the first degree. The Newmark approximation of the equation of motion is:

$$\dot{\eta}^{n+1} = \dot{\eta}^n + \frac{1}{2}\Delta t \ddot{\eta}^n + \frac{1}{2}\Delta t \ddot{\eta}^{n+1} \quad (7.9)$$

$$\eta^{n+1} = \eta^n + \Delta t \dot{\eta}^n + \frac{1}{4}\Delta t^2 \ddot{\eta}^n + \frac{1}{4}\Delta t^2 \ddot{\eta}^{n+1} \quad (7.10)$$

In [7] we can see that the error made by these approximations is of order $\Delta t^3 \eta^{(4)}$ in equation (7.9) and the error for η^{n+1} , equation (7.10) is of order $\Delta t^3 \eta^{(3)}$.

Substituting this into the equation of motion at time t_{n+1} , we get:

$$\left(m + \frac{1}{2}\Delta t b + \frac{1}{4}\Delta t^2 k \right) \ddot{\eta}^{n+1} \quad (7.11)$$

$$= \mathbf{f}^{n+1} - b \left(\dot{\eta}^n + \frac{1}{2}\Delta t \ddot{\eta}^n \right) - k \left(\eta^n + \Delta t \dot{\eta}^n + \frac{1}{4}\Delta t^2 \ddot{\eta}^n \right) \quad (7.12)$$

Since we introduced implicit terms in the calculation of the new displacement and velocity, equations (7.9) and (7.10), this system is solved by a prediction-correction method. We explain this method by following the solution step by step.

7.2.2 Solution

We need initial conditions for both displacement and velocity. So in t_0 we define both η^0 and $\dot{\eta}^0$.

In the following the we start from a known state of the mass-spring system at $t = t_n$. And we solve the state at time t_{n+1} .

prediction

First we predict the values of the displacement and velocity of the membrane using the state at instant t_n :

$$\dot{\eta}_*^{n+1} = \dot{\eta}^n + \frac{1}{2}\Delta t \ddot{\eta}^n \quad (7.13)$$

$$\eta_*^{n+1} = \eta^n + \Delta t \dot{\eta}^n + \frac{1}{4}\Delta t^2 \ddot{\eta}^n \quad (7.14)$$

calculation of $\ddot{\eta}^{n+1}$

With the estimated displacement and velocity, we can calculate the acceleration at instant t_{n+1} , using the equation of motion (7.11). The solution is direct, we divide the right hand side by the factor in front of $\ddot{\eta}^{n+1}$.

correction

After that we correct the displacement and the velocity using the the acceleration term just calculated:

$$\dot{\eta}^{n+1} = \dot{\eta}_*^{n+1} + \frac{1}{2}\Delta t \ddot{\eta}^{n+1} \quad (7.15)$$

$$\eta^{n+1} = \eta_*^{n+1} + \frac{1}{4}\Delta t^2 \ddot{\eta}^{n+1} \quad (7.16)$$

Once we have corrected, we can advance in time. The flowchart explaining the Newmark method, applied on a more general problem, is shown in figure E.3.

On the accuracy of the Newmark method, a brief discussion can be found in appendix D. We can conclude that the approximations shown above introduce an error in the periodicity of the solution of the problem. In [7] this error is calculated:

$$\frac{\Delta T}{T} = \frac{\omega^2 \Delta t^2}{12} \quad (7.17)$$

where T is the period of the calculated solution and ω is the angular frequency of the exact solution.

An important feature of the Newmark method is that it is unconditionally stable. The parameters (m , b , k) and the time-step Δt do not intervene in the factor of amplification (see appendix D). This factor has always the value of unity.

For the moment the external force is not yet specified. In the simulation model for the vocal folds we will apply the hydrodynamic force as the driving force on the mass. In the next chapter we will explain how we coupled the unsteady flow model and the model for wall motion exactly.

Chapter 8

Application: vocal folds

In this chapter we present our model for simulation of the flow through and the motion of the vocal folds. In figure 8.1 a schematic drawing of this model is shown. The model is symmetric with respect to the flow channel axis (the dashed line in the figure). The vocal folds are represented by a one-mass-spring system, positioned in an envelope which forms a cosine-shaped constriction in the channel. The position of the wall is then given by:

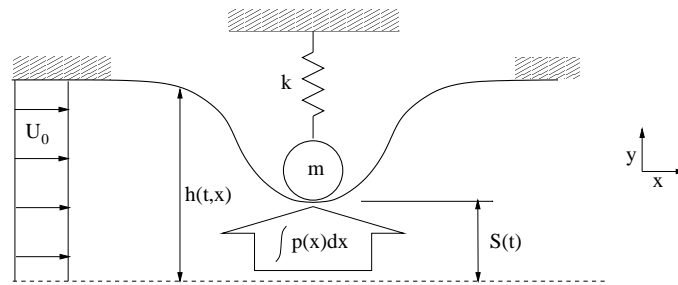


Figure 8.1: The model for the vocal folds.

$$h(t, x) = S(t) \frac{1}{2} (\cos(2\pi x/L_m) - 1) \quad (8.1)$$

where $S(t)$ represents the section of the channel at the position of the mass, L_m is the longitudinal dimension of the vocal folds (upstream-downstream). The channel is straight if $S = 1$, and totally pinched if $S = 0$. Note that one can choose the initial value $S(0)$ freely.

In this model the mechanical behaviour of the vocal folds is described by the simple relation (in reference to (6.21)):

$$\ddot{\eta} + \eta = \alpha F \quad (8.2)$$

which determines the displacement η of the mass, with respect to the initial position, as a function of time. We took $m = k = 1$ and $b = 0$ to keep things simple, but we added a coupling coefficient α for the force F which we can change to regulate the relative importance of F with respect to m and k . The section S evolves in time, according to:

$$S(t) = S(0) + \eta(t) \quad (8.3)$$

Equations (8.1) through (8.3) describe the relation between the displacement of the mass in the mass spring model and the position of the channel wall $h(t, x)$.

We use the hydrodynamic pressure as a coupling between the flow and the wall motion. In principle the relationship between the pressure distribution and the force on the mass can be very complex. Here we chose for the most simple relationship. We integrate the pressure over the glottis and apply this force as source term F in equation (8.2). We apply thus the mean value of the pressure as interacting force.

The behaviour of this simple model of the vocal folds is already rather complicated. Even if we only couple the pressure in this simple way. This is because the pressure is a function of the wall displacement and thus appears active in the simulation of the vocal folds motion.

In the next section we present the exact geometry which was applied to study the model of the vocal folds. Then we study the behaviour of the mean pressure F as a function of $S(t)$ and the behaviour of the mass-spring system in response to F .

8.1 The applied geometry

The geometry of the channel which represents our model of the airway through the vocal folds, is depicted in figure 8.1. For the nondimensionalised height we chose $H = 1$ (of course), for the length of the channel we chose 1 as well (so in real the length L will be equal to $HR e_H$). The cosine shaped constriction is placed in the middle of the channel, between two straight, rigid parts having height 1. The 'vocal fold' has a length of $L_m = 0.2$, so it is situated on the interval $0.4 \leq x \leq 0.6$.

We examined the mean pressure response for the two different flow models: the imposed flux and the imposed pressure difference. These studies are presented in section 8.2 and 8.3, respectively. In each section we first examine the response of the force F to an imposed state of the wall motion ($\eta(t)$ and $\dot{\eta}(t)$). This is done by keeping S constant in time: the static response, and forcing an oscillation of $S(t)$ in the elastic part of the wall: the dynamic response.

After that we show the motion of the vocal folds by really coupling the simulations. Numerically the coupling means that for the functions h^{n+1} and \dot{h}^{n+1} at time t_{n+1} in equation (7.1) we take the wall position and velocity derived from the **predicted** state of the mass-spring system η_*^{n+1} and $\dot{\eta}_*^{n+1}$. With those we solve for the pressure function p_i , of which the mean value we apply as the external force in the mass-spring model.

8.2 Imposed flux

The first case we examine is the imposed flux. The entrance velocity is kept constant in time.

First the static force response is determined by determining the mean pressure for different values of S which are kept constant. In figure 8.2 the force F is depicted as a function of S .

The pressure in the fluid is always negative, because the value at $x = 0$ is chosen zero. The pressure decreases as x increases, forcing a flow in the positive x direction. The mean pressure force decreases dramatically for S approaching 0. If we pinch-off the channel, and impose a flux at the same time, we force the same amount of fluid through a channel becoming smaller. The fluid is accelerated because of flux conservation. For frictionless flow the velocity will accelerate according to

$$U = \frac{U_0}{S} \tag{8.4}$$

where U tends to infinity if S tends to 0, causing a dramatic pressure drop over the vocal folds.

For the dynamic response of the pressure an oscillation of the mass is forced. The section oscillates about $S = 1$ with an amplitude of 0.05. The channel is thus repeatedly pinched and enlarged. In

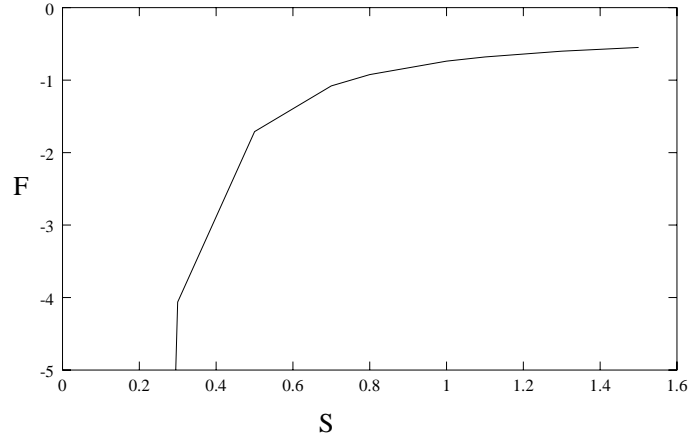


Figure 8.2: The force F as a function of the section of the channel, static response.

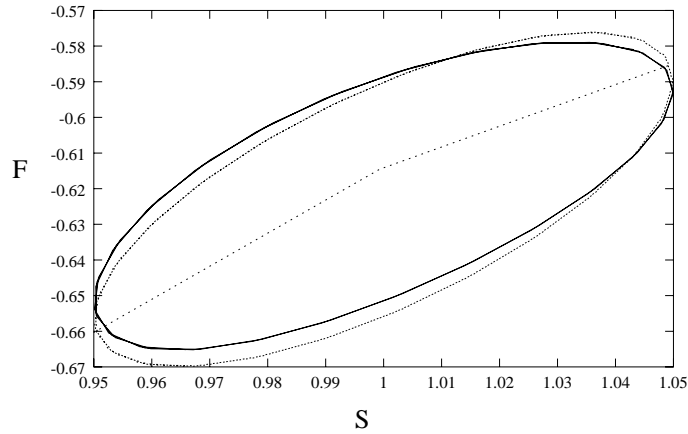


Figure 8.3: The response of the force F as a function of oscillating S . The dotted line across the loops is the static response. The solid loop, the force response to oscillation, runs clockwise. The dashed loop is the pressure response predicted by asymptotic analysis [21].

figure 8.3 the dynamic response of the pressure is shown. The dynamic response of the force forms loops which run in clockwise direction. In other words, the force is different for decreasing and increasing section. From the figure it can be seen that the force is greater (in a negative sense) if the section decreases, than for increasing section. The pressure in the fluid exercises work on the moving mass, and thus transfers energy. The energy is injected into the motion of the mass.

For forced oscillations of very small amplitudes like the one imposed above, we could say the oscillation is a small perturbation in the wall of a straight channel. In that case an asymptotic development can be made in order to solve the flow over the little oscillating bump. In the analysis, done by Smith [21], it is found that the pressure response to the perturbation is a function of the section and the velocity of vibration:

$$F \sim a(S - 1) + b \frac{\partial S}{\partial t} + c \quad (8.5)$$

These coefficients can be solved for, and they are in the order of unity [21]. We verified this behaviour by fitting the coefficients. The coefficients a and c can be fitted from the curve of the static response (figure 8.2): $a = 0.66$, $c = -0.62$. The value of b is guessed to have best fit on sight, which yields: $b = 0.13$. This fitted curve is plotted in figure 8.3, the dotted loop.

A very similar behaviour of the pressure in unsteady channel flow over constrictions or expansions

has been found by various authors, among which Lucero [13], Pedrizzetti [16] and Young & Tsai [25].

The behaviour of the mean pressure conform (8.5) is applied to the mass spring model of the vocal folds, equation (8.2), where we took $\alpha = 0.2$. The way in which the oscillator responds to that is depicted in figure 8.4, from which we can see that the amplitude of oscillation increases. This is

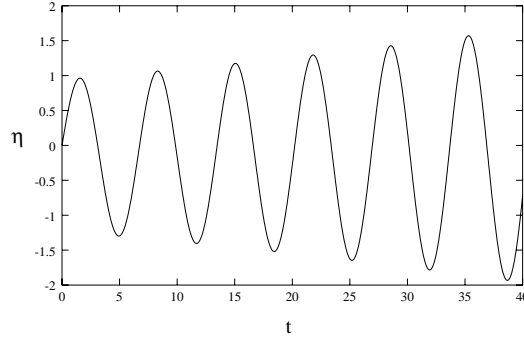


Figure 8.4: The response of the mass spring system to the force F from equation (8.5).

due to the response of the pressure to the displacement of the mass. Substituting equation (8.5) in (8.2), we can interpret the term b from the former as a negative damping term for the oscillator. The fluid exerts work of the wall, via the pressure. The net energy transfer is equal to the area of the force loop in figure 8.3.

The behaviour of the mean pressure for the case that we impose a constant pressure drop over the channel ($0 \leq x \leq 1$), is different from the constant flux model. This case is discussed in the next section.

8.3 Imposed pressure difference

For this case we vary the entrance velocity (flux) in order to obtain the desired pressure difference.

The static pressure response is depicted in figure 8.5 for three different values of the imposed pressure drop ¹: $\Delta p = -4$, -2.9 and -2 . These curves have the same shape, they differ only by

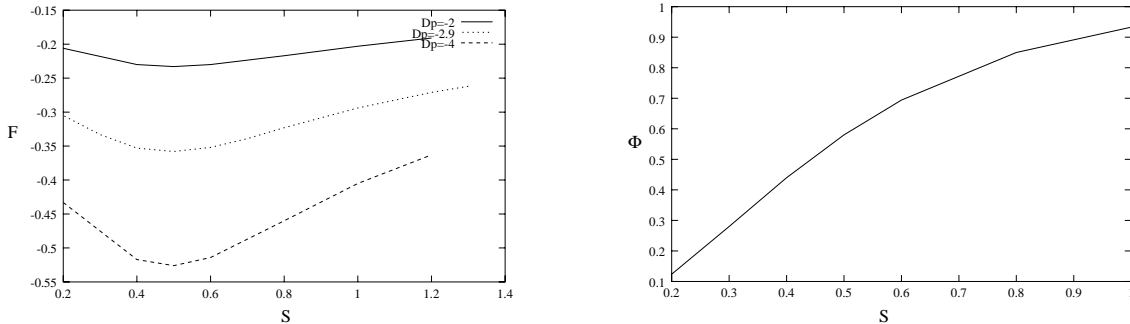


Figure 8.5: The force F as a function of the section of the channel, static response, for three different values of the imposed pressure difference (left), and the dependence of the volume flux on S for the case $\Delta p = -2.9$.

¹These values are arbitrarily chosen, as well as the values later on in the figures 8.6 through 8.8. However, in case of Poiseuille flow we have $\Delta p = -3$ over a straight channel with length 1 (see section 2.1.4). So we have one value above and one below the pressure difference Poiseuille.

a factor in F . The force increases (in a negative sense) when the channel is pinched, until a minimum in the curve is attained for $S = 0.5$. If the channel is pinched further, the force becomes less negative. This is because of a reduction of the volume flux, in order to keep the pressure drop over the channel constant. For $\Delta p = -2.9$ the dependence of the volume flux on the section of the channel is also depicted in figure 8.5. As can be seen from that, the volume flux decreases if the channel is pinched, in order to obtain the demanded pressure drop.

The dynamic pressure response is investigated for three different values of Δp : -1.5, -3.5 and -5.5. For that, we force an oscillation of the section S about the value 0.5 with an amplitude of 0.2. The behaviour of the force to that is displayed in figures 8.6 through 8.8.

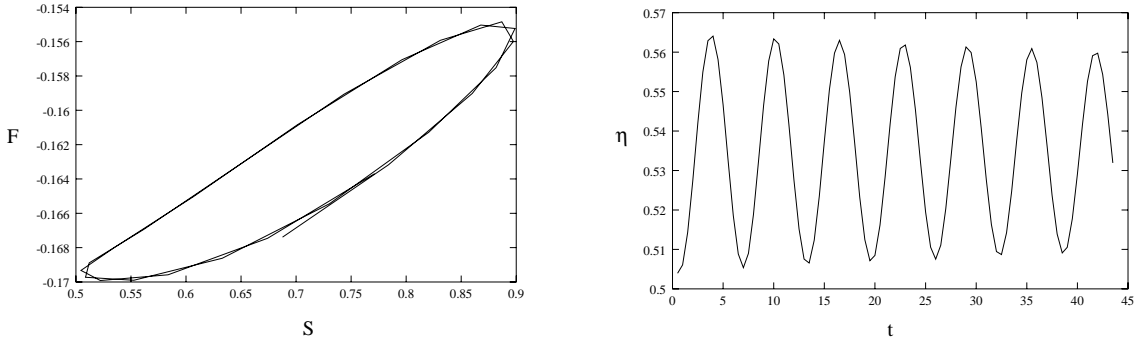


Figure 8.6: The dynamic response of the force F to a forced oscillation of S ; $\Delta p = -1.5$ (left) and the behaviour of the mass-spring model in reaction to this force.

For the pressure drop $\Delta p = -1.5$, the mean pressure shows a hysteresis loop running counterclockwise (figure 8.6). The pressure is less strong when the section decreases, than when it increases. This means that there is a transfer of energy from the membrane to the fluid. The pressure adds a damping term in the vocal fold model. As a consequence for this pressure difference the oscillation will die out. This can be seen in the right figure, where the simulations of the flow and the membrane are actually coupled. The damping term is very weak because the imposed pressure drop is small, causing the force to be small as well.

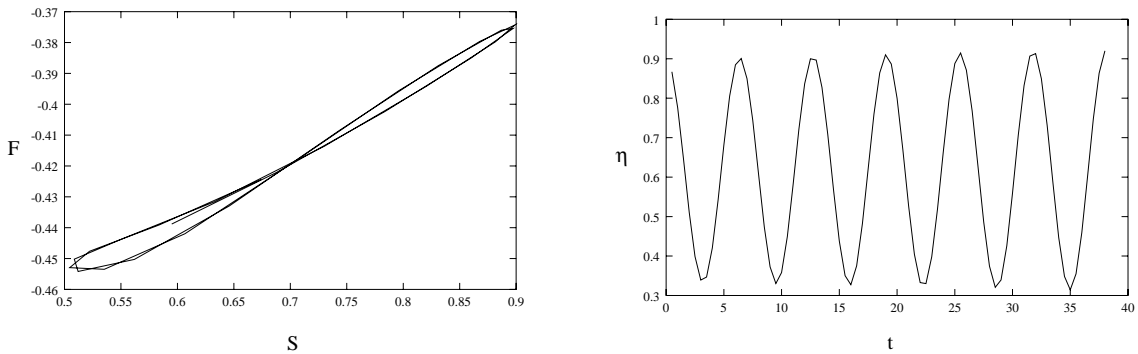


Figure 8.7: The dynamic response of the force F to a forced oscillation of S ; $\Delta p = -3.5$ (left) and the mass-spring oscillation responding to this pressure.

In case the pressure drop is -3.5 the force loop crosses its path halfway. The upper right part runs in a counterclockwise sense, causing a damping in the oscillation. The lower left part, however, runs in the opposite direction amplifying the oscillation. These two terms cancel each other at least partially. Depending on the exact ratio of the two areas, the oscillation will damp out, amplified or even have a constant amplitude. The right figure of 8.7 displays a slightly damped oscillator which is the result of coupling the simulations of the flow and the membrane (run with $\Delta p = -3.5$).

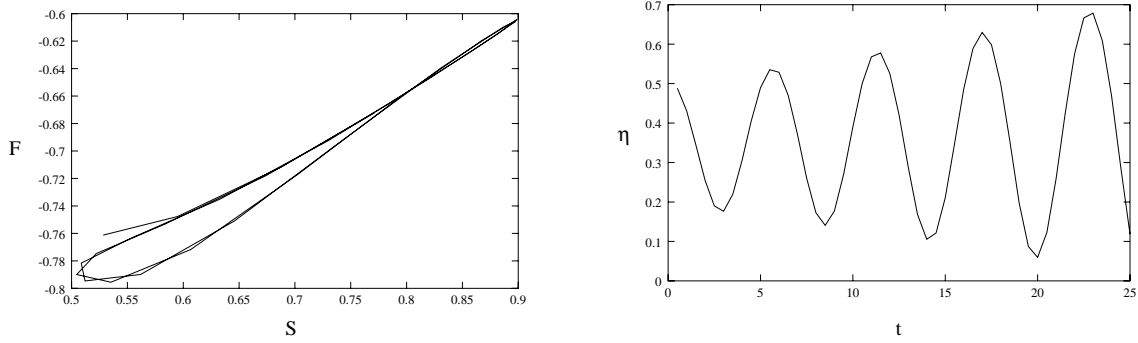


Figure 8.8: The dynamic response of the force F to a forced oscillation of S ; $\Delta p = -5.5$ (left) and the mass-spring oscillation responding to this pressure.

For a pressure drop of value -5.5 gives qualitatively the same force behaviour as the case where the flux in imposed. The biggest loop runs in clockwise direction (see figure 8.8). This gives again a transfer of energy from the fluid to the membrane, of which the oscillation amplifies, as can be seen from the right figure.

As a conclusion we could say one passes from a damped oscillation to an amplified, by increasing the imposed pressure drop.

Chapter 9

Discussion

As we have seen in section 6.1.2 the unsteady flow model gives accurate solutions to the Rayleigh problem and the oscillatory Poiseuille flow. The simulation is most probably fast in comparison with full Navier Stokes simulation, since we use an analogously simplified model of the Navier Stokes equations as for the steady channel flow model. In case we impose the volume flux in our simulation it is per time-step as fast as the steady channel flow simulation. In case we impose a pressure drop, for each instant the flow simulation is rerun several times, in order to find the right flux in accordance with the pressure drop. The amount of time this takes is proportional to the number of iterations on the volume flux needed. Real time simulation of the vibration of the vocal folds will most probably not be possible with this flow model.

The numerical method used for solution of the mass-spring model of the vocal folds is unconditionally stable, an error occurs in the periodicity which is of order $\omega^2 \Delta t^2$.

We have studied the behaviour of the mean pressure F in response to a forced oscillation of the vocal folds in section 8. We have observed that this force shows hysteresis. There is a transfer of energy between the fluid and the vocal folds, via the pressure.

For an imposed volume flux we find a net transfer of energy from the fluid to the vocal folds (see figure 8.3). When this force is implemented on the mass-spring system, it oscillates with an increasing amplitude. We have no physical constraint for the amplitude of oscillation (such as the section S cannot become negative). So, in a coupled simulation of the flow and vocal folds motion, the amplitude of oscillation will increase without a limit (see figure 8.4).

In case we impose the pressure difference over the channel, we observe a transfer of energy in both directions. In figures 8.6, 8.7 and 8.8 we have shown the behaviour of the mean pressure for decreasing pressure differences (which are $\Delta p = -1.5$, -3.5 and -5.5 , respectively). For the weakest pressure drop ($\Delta p = -1.5$) we find a net energy transfer from the vocal folds to the fluid. The oscillation of the vocal folds will be damped out this way. In case $\Delta p = -3.5$, we find energy transfer in both directions of roughly the same order, and if we impose $\Delta p = -5.5$ energy is transferred from the fluid to the vocal folds.

An important aspect of our model is that one mechanical degree of freedom is sufficient for simulation of the vibration of the vocal folds (only one mass and spring). Pelorson et al. [17] and Lous et al. [12] use a quasi steady flow model which requires two mechanical degrees of freedom (two masses and two springs) to explain vocal fold oscillation.

Like in our model, in the two-mass model of Pelorson et al.[17] the pressure is the driving force of oscillation. In this two-mass model the masses can oscillate with a phase difference. This causes the glottis to change from convergent to divergent (i.e. the way it is depicted in figure 1.3) and back. In a divergent channel flow-separation can occur. Pelorson et al. calculate the point of separation, which is a function of time related to the dynamic geometry, and suppose that beyond

this point a jet emerges. Beyond this point they thus apply a constant pressure, which is equal to zero. The force they apply as source for oscillation is the pressure integrated up to the point of separation.

In our model we observe flow-separation in certain cases as well. For example in figure 9.1, we captured the unsteady flow simulation (with imposed volume flux) at a time that $S = 0.5$. We

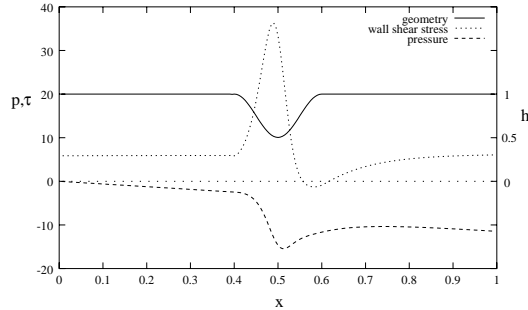


Figure 9.1: The situation of the flow simulation through the glottis at a certain moment. The curves of the geometry (right scale), pressure and the wall shear stress (left scale) are shown. The latter passes through zero which means that separation occurs.

see from the curve of the wall shear stress, that separation occurs in the diverging, downstream side of the vocal folds. In our simulation we observe that the flow re-attaches to the wall, an effect that is not extraordinary but rather different from the model of Pelorson et al. [17]. A possible explanation for this difference is that we apply a rather smooth shape of the vocal folds and a rather weak constriction of the airway, whereas in the model of Pelorson et al. the vocal folds are allowed to close the airway. For the calculation of the force we integrate on the interval $0.4 \leq x \leq 0.6$, even if separation occurs within this interval.

An interesting aspect is that in many two-mass models the vocal folds can collide with each other, closing the airway. In normal speech this is in fact what is happening, the vocal folds open and close periodically. In our model, we do not allow the vocal folds to collide. It seems that phonation can also take place even if the vocal folds are not touching each other, which justifies our assumption.

Chapter 10

General conclusions

In the first part of this report we showed that for steady channel flow, simulation of the RNS-p(x) model has quite accurate results when applied on a particular geometry for which analytical solutions exist. The results of this model, applied on a straight channel geometry with a discontinuous expansion, have been compared with the results of simulation of the complete two dimensional Navier Stokes equations by FLUENT (section 3.3.1). We found a discrepancy in the resulting velocity fields of 3%.

The steady RNS-p(x) channel flow model has been used to simulate the flow through a flue channel in the mouthpiece of a recorder type flute. The results of these simulations display a discrepancy of about 10% in comparison with experimental results.

The unsteady flow model which is based on the same physical assumptions as the steady model, has been applied for simulation of the flow through the glottis, in a coupled simulation of the flow and the vibration of the vocal folds. The vocal folds are described with a single mass-spring model which is numerically solved with an unconditionally stable method.

Vocal fold oscillation is observed in these simulations, even with one mechanical degree of freedom. This in contrast to the models of Pelorson et al. [17] and Lous et al. [12] where a quasi steady flow model is used which requires two mechanical degrees of freedom (two masses and two springs) to explain vocal fold oscillation.

In conclusion we give some suggestions for future work:

- implementation of an adjustable grid in longitudinal direction in the simulation of the flow models, where the density of calculation points can vary over the domain,
- a quantitative comparison of our and other results of vocal folds simulations, containing order of magnitude of the forces, frequencies etc,
- study of the physical validity of re-attachment of flow after separation, and verify whether a constant pressure should be imposed beyond the point of separation or not,
- implementation of a way to constrain the motion of the vocal folds physically,
- generalization of the vocal folds model, to obtain a more realistic behaviour.

Bibliography

- [1] BENDER, C.M.& ORSZAG, S.A., Advanced mathematical methods for scientists and engineers. *McGraw-Hill*, 1978
- [2] BOOGAART, E.W., Onderzoek naar het akoestische gedrag van een blokfluit en de invloed van de geometrie van de kernspleet. *Report R-1462-S, Eindhoven University of technology*, 1998
- [3] COUSTEIX, J., Aerodynamique Couche limite laminaire. *Cepadues-Editions*, 1988
- [4] DRAZIN, P.G.& REID, W.H., Hydrodynamic stability. *Cambridge University Press*, 1981
- [5] An interesting internet site on voice quality from the University of Stuttgart: <http://www.ims.uni-stuttgart.de/phonetik/EGG/>
- [6] FABRE, B. ET AL., Vortex shedding in steady oscillation of a flue organ pipe. *Acustica Acta Acustica* **82**, p. 863-877, 1996
- [7] GÉRADIN, M. & RIXEN, D., Théorie des vibrations Application à la dynamique des structures. *Masson*, 1996
- [8] GERMAIN, P., Mécanique Tome I + II. *Ecole Polytechnique/ Edition Marketing*, 1986
- [9] HOFMANS, G.C.J., Vortex sound in confined flows. *PhD thesis Eindhoven University of technology*, 1998
- [10] ISAACSON, E. & KELLER, H.B., Analysis of numerical methods. *Wiley & Sons*, 1966
- [11] LAGRÉE, P.-Y., An inverse technique to deduce the elasticity of a large artery. *Eur. Phys. J. AP* **9**, p. 153-163, 2000
- [12] LOUS, N.J.C., HOFMANS, G.C.J., VELDHUIS, R.N.J., HIRSCHBERG, A., A symmetrical two-mass vocal-fold model coupled to vocal tract and trachea, with application to prothesis design. *Acustica Acta Acustica* **84**, p. 1135-1150, 1998
- [13] LUCERO, J.C., A theoretical study of the hysteresis phenomenon at vocal fold oscillation onset-offset. *J. Acoust. Soc. Am* **105**, p. 423-431, 1999
- [14] LUO, X.Y., PEDLEY, T.J., The effects of wall inertia on flow in a two-dimensional collapsible channel. *J. Fluid Mech.*, **363**, p. 253-280, 1998
- [15] PEDLEY, T.J., The fluid mechanics of large blood vessels. *Cambridge University Press*, 1980
- [16] PEDRIZZETTI, G., Unsteady tube flow over an expansion. *J. Fluid Mech.* **310**, p. 89-111, 1996
- [17] PELORSON, X., HIRSCHBERG, A., HASSEL, R.R. VAN, WIJNANDS, A.P.J., AUREGAN, Y., Theoretical and experimental study of quasisteady flow separation within the glottis during phonation. *J. Acoust. Soc. Am* **96**, p. 3416-3431, 1994

- [18] PEYRET, R.& TAYLOR, T.D., Computational methods for fluid flow. *Springer-Verlag*, 1983
- [19] SCHLICHTING, H., Boundary-layer theory. *McGraw-Hill*, 1979
- [20] SÉGOUFIN, C., FABRE, B., VERGE, M.P., HIRSHBERG, A., WIJNANDS, A.P.J., Experimental study of the influence of the mouth geometry on sound production in a recorder-like instrument : windway length and chamfers. accepted by *Acustica Acta Acustica*, 2000.
- [21] SMITH, F.T., Flow through constricted or dilated pipes and channels, part 1 and 2. *Q. J. MEch. Appl. Math.*, **29**, pp 343- 364 & 365- 376., 1976
- [22] STORY, B.H., TITZE, I.R., Voice simulation with a body-cover model of the vocal folds. *J. Acoust. Soc. Am* **97**, p. 1249-1260, 1995
- [23] TILLAART, J. v.D., Velocity profile at the flue exit of a recorder:hot wire measurements. *Report R-1491-S, Eindhoven University of technology*, 1999
- [24] WALSH, C., Flutter in one-dimensional collapsible tubes. *J. Fluids Struct.* **9**, p.393-408, 1995
- [25] YOUNG, D.F., TSAI, F.Y., Flow-characteristics in models of arterial stenosis-II. Unsteady flow. *J. Biomechanics* **6**, p.547-559, 1973

Appendix A

The von Kármán equation

The boundary layer problem can be solved using an approximative method, based on the von Kármán equation. The von Kármán equation is obtained by integrating the momentum equation (2.17) over y (from 0 to ∞ , using continuity (2.16) and the definitions of δ_1 and δ_2 , we obtain the famous von Kármán equation (see [19]):

$$\frac{d}{dx} (\delta_2 U^2) + \delta_1 U \frac{dU}{dx} = \frac{\partial u}{\partial y} \Big|_{y=0} \quad (\text{A.1})$$

Further, we define the ratio between the displacement thicknesses and the momentum displacement thickness H_{12} :

$$H_{12} = \frac{\delta_1}{\delta_2} \quad (\text{A.2})$$

this ratio is a function of $\frac{dU}{dx}$ and δ_1 .

In the von Kármán equation we thus encounter three unknown quantities: δ_1 (or δ_2), $U(x)$ and the derivative $\frac{\partial u}{\partial y}$. It is convenient to define a friction coefficient, called f_2 by:

$$\frac{\partial u}{\partial y} \Big|_{y=0} = f_2 \frac{H_{12}}{\delta_1} U \quad (\text{A.3})$$

which is, like H_{12} , a function of $\frac{dU}{dx}$ and δ_1 . Until now, these parameters H_{12} and f_2 are yet unknown. But it is possible to calculate these functions once we have chosen a certain velocity profile $u(y)$, the closure of the problem. Here we will discuss two possible closures: the Falkner Skan method and a polynomial closure.

The Falkner Skan closure

This method gives us numerical values of H_{12} and f_2 , which can be approached by the following functions (see figure A.1):

$$\begin{aligned} H_{12} &= 2.5905 \exp(-0.37098 * \Lambda_1) \\ \text{if } \Lambda_1 > 0.6 \quad H_{12} &= 2.5905 \exp(-0.37098 * 0.6) \\ f_2 &= 0.9396 \left(-\frac{1}{H_{12}} + \frac{4}{H_{12}^2} \right) \end{aligned} \quad (\text{A.4})$$

where we have introduced another parameter Λ_1 , which is defined by:

$$\Lambda_1 = \delta_1^2 \frac{dU}{dx} \quad (\text{A.5})$$

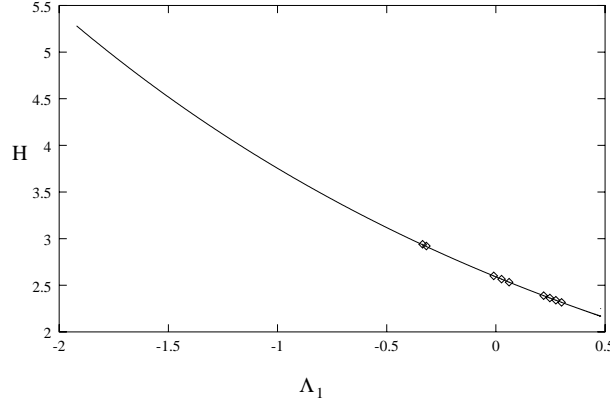


Figure A.1: The ratio H_{12} as a function of Λ_1 according to the Falkner Skan closure. The curve is fitted through the points [SCHLICHTING?].

This leaves us with only two unknown quantities, δ_1 and $U(x)$. By conservation of flux (2.24) we can express $U(x)$ as a function of δ_1 .

We do now have a solvable coupled set of equations, namely the von Kármán equation (A.1), which we can write as:

$$U^2 \frac{d}{dx} \left(\frac{\delta_1}{H_{12}} \right) + \left(1 + \frac{2}{H_{12}} \right) \delta_1 U \frac{dU}{dx} = f_2 \frac{H_{12}}{\delta_1} U \quad (\text{A.6})$$

using (A.4), (A.5) and U as a function of δ_1 , from flux conservation.

These equations have been solved for δ_1 using a program written in **C**, by means of the method of finite differences.

Polynomial closure

The second method closing the set of equations is simpler: the polynomial closure. Here we choose a polynomial for $u(y)$ in terms of y , respecting the boundary conditions ($u(0) = 0$ and $u'(y^* = \delta) = 0$) (For a few examples, see [19, p.206]). From this we can calculate the factor H_{12} , and the derivative du/dy at the wall. Moreover, if the chosen polynomial has no further parameters, these quantities will both be constant for all x . Still using flux conservation we can now integrate the von Kármán equation by hand. This results in the variable x as a function of δ (rather than the other way round):

$$x = c^{-1} \left[\left(\frac{1}{H_{12}} + 1 \right) \frac{\delta}{2} + \frac{2}{\alpha} \left(\frac{3}{2H_{12}} + 1 \right) \ln \left(1 - \frac{\alpha\delta}{2} \right) + \left(\frac{2}{H_{12}} + 1 \right) \frac{\delta}{2 - \alpha\delta} \right] \quad (\text{A.7})$$

where we have defined $\alpha = 2\delta_1/\delta$ and c is the first derivative of the chosen velocity profile at the wall:

$$c = \left. \frac{\partial u}{\partial y} \right|_{y=0} \quad (\text{A.8})$$

From equation (A.7) we can solve δ (and δ_1) using Newton's method, but it's much simpler to calculate x from given values of δ . Since δ is a monotonously increasing function of x , there won't be any problems using this technique. We have applied this solution to two different velocity profiles: a linear profile ($c = 1$, $\alpha = 1$ and $H_{12} = 3$ which have also been done in [23]) and a polynomial of the fourth degree in y ($c = 2$, $\alpha = \frac{3}{5}$ and $H_{12} = 2.554$).

In this method we permit δ_1 to become as thick as $h/2$, with U tending towards infinity (equation 2.23). There are several ways to limit the growth of δ_1 , in order to keep physical significance of

the model. One possibility is to set the upper limit to the value δ_1 has in Poiseuille flow. For the parabolic velocity profile (2.28) we can easily find: $\delta_1 = 1/3$ by using the definition (2.19).

The solutions of the displacement thickness are plotted in figure 2.5, and compared with Blasius', Poiseuille's solutions and the numerical solution of the RNS-p(x) equations.

Appendix B

Numerical methods

In this appendix some basic principles of numerical methods are explained. In section B.1 several methods will be discussed of putting differential equations in a discrete form in order to solve it by one-step integration. We will discuss three straightforward approximations of a second order differential equation and a more complicated approximation: the Newmark approximation.

In section B.2 we discuss a very fast numerical solution of a system of linear equations. This method is called the the method of factorization and it is basically a quick algorithm for inversion of three diagonal matrices.

B.1 Discretisation methods

Consider a function $f(x)$ defined on a range $a \leq x \leq b$, which is discretised by the set $x_0 = a, x_1 \dots x_N = b$. The discrete representation of this function is $f_i \equiv f(x_i)$. Say f is a solution of a differential equation.

In general, the m th derivative of f at $x = x_i$ is approximated by:

$$\frac{d^m f(x_i)}{dx^m} = \sum_{j=J_1}^{j=J_2} a_j f_{i+j} \quad (\text{B.1})$$

where J_1, J_2 are integers and a_j are found by expressing f_{i+j} in terms of f_i by means of Taylor expansion:

$$f_{i+j} = f_i + j\Delta x \frac{df(x_i)}{dx} + \frac{(j\Delta x)^2}{2} \frac{d^2 f(x_i)}{dx^2} + \dots + \frac{(j\Delta x)^k}{k!} \frac{d^k f(x_i)}{dx^k} + R_k \quad (\text{B.2})$$

where Δx is the pace size ($x_{i+1} - x_i$, taken constant here) and R_k is the rest term of order k :

$$R_k = \frac{1}{k} \int_{x_i}^{x_{i+j}} \frac{d^{k+1} f(\xi)}{dx^{k+1}} (x_i + j\Delta x - \xi)^k d\xi \quad (\text{B.3})$$

An example: we approximate the first derivative of f , where we use the two neighbouring points, i.e. we take $J_1 = -1$ and $J_2 = 1$:

$$\frac{df(x_i)}{dx} \cong \frac{(1 - \alpha) f_{i+1} + 2\alpha f_i - (1 + \alpha) f_{i-1}}{2\Delta x} \quad (\text{B.4})$$

with α an arbitrary constant, which depicts the freedom of choice we have for discretisation. Substituting the Taylor expansion determines the error of the approximation:

$$-\frac{\alpha\Delta x}{2} \frac{d^2 f(x_i)}{dx^2} + \frac{\Delta x^2}{6} \frac{d^3 f(x_i)}{dx^3} \quad (\text{B.5})$$

Specifying α gives several standard forms of approximation:

- $\alpha = -1$: forward

$$\frac{df(x_i)}{dx} \approx \frac{f_{i+1} - f_i}{\Delta x} \quad (\text{B.6})$$

with error $\mathcal{O}(\Delta x)$

- $\alpha = 0$: centered

$$\frac{df(x_i)}{dx} \approx \frac{f_{i+1} - f_{i-1}}{2\Delta x} \quad (\text{B.7})$$

with error $\mathcal{O}(\Delta x^2)$

- $\alpha = 1$: backward

$$\frac{df(x_i)}{dx} \approx \frac{f_i - f_{i-1}}{\Delta x} \quad (\text{B.8})$$

with error $\mathcal{O}(\Delta x)$

The choice of indices in discretisation determines not only the error of approximation, but also the stability of the algorithm, as we will see later on.

The second derivative of f can also be expressed in a million ways. The choice of indices in discretisation determine the accuracy and stability of the numerical method.

B.1.1 Straightforward approximations

With a straightforward approximation we mean that the approximation is just a question of choosing the indices of the discrete function. We will illustrate the effects of these choices by numerical solution of the mass spring system.

We solve the differential equation of a undamped mass-spring system.

$$\frac{d^2 \eta}{dt^2} = -\omega^2 \eta \quad (\text{B.9})$$

With the initial conditions:

$$\begin{aligned} \eta(0) &= \eta_0 \\ \frac{d\eta}{dt}(0) &= \dot{\eta}_0 \end{aligned} \quad (\text{B.10})$$

In order to be able to solve this numerically, by means of simple integration, we have to split the equation B.9 into two equations of the first degree:

$$\begin{aligned}\frac{d\eta}{dt} &= \dot{\eta} \\ \frac{d\dot{\eta}}{dt} &= -\omega^2\eta\end{aligned}\tag{B.11}$$

with of course the same initial conditions.

We solve these equations with three different numeric schedules; a so called explicit, implicit and a partially implicit schedule.

We have two ordinary (but coupled) differential equations of the first degree, two unknowns (η and $\dot{\eta}$) and two conditions (B.11). So we can solve it.

We have to discretise the two unknowns and our variable t . We use the index i which runs from 1 to N to indicate the pace in time:

$$\begin{aligned}\eta_i &= \eta(t = t_i) \quad 1 \leq i \leq N \\ \dot{\eta}_i &= \frac{d\eta}{dt}(t = t_i)\end{aligned}\tag{B.12}$$

Three different approximations to the second derivative of η are given below, with their influence on the accuracy and stability of the solution.

Explicit schedule

The most natural way to insert our discretised system into the equations would be, what is called the explicit schedule. We apply the 'forward' approximation twice:

$$\begin{aligned}\frac{\eta_{i+1} - \eta_i}{\Delta t} &= \dot{\eta}_i \\ \frac{\dot{\eta}_{i+1} - \dot{\eta}_i}{\Delta t} &= -\omega^2\eta_i\end{aligned}\tag{B.13}$$

This schedule does not work, it is unstable. We will see why when we calculate the difference between the exact and the discretised differential equations, with the help of Taylor series.

Accuracy and stability

First, we substitute the first equation of (B.13) into the other. We obtain:

$$\frac{\eta_{i+2} - 2\eta_{i+1} + \eta_i}{\Delta t^2} + \omega^2\eta_i = 0\tag{B.14}$$

In fact it is not exactly equal to zero, because η_i is not the exact solution to the problem. In order to find the discrepancy we examine the Taylor expansion of the discrete solution. We develop the individual terms in a Taylor series about ($t = t_i$) up to order Δt^3 :

$$\begin{aligned}\eta_{i+2} &= \eta\Big|_{t_i} + 2\Delta t \frac{d\eta}{dt}\Big|_{t_i} + 2\Delta t^2 \frac{d^2\eta}{dt^2}\Big|_{t_i} + \frac{4}{3}\Delta t^3 \frac{d^3\eta}{dt^3}\Big|_{t_i} + \mathcal{O}(\Delta t^4) \\ \eta_{i+1} &= \eta\Big|_{t_i} + \Delta t \frac{d\eta}{dt}\Big|_{t_i} + \frac{1}{2}\Delta t^2 \frac{d^2\eta}{dt^2}\Big|_{t_i} + \frac{1}{6}\Delta t^3 \frac{d^3\eta}{dt^3}\Big|_{t_i} + \mathcal{O}(\Delta t^4)\end{aligned}\tag{B.15}$$

From this we can calculate the difference between the exact and the discrete second derivative:

$$\frac{\eta_{i+2} - 2\eta_{i+1} + \eta_i}{\Delta t^2} = \frac{d^2\eta}{dt^2}\Big|_{t_i} + \Delta t \frac{d^3\eta}{dt^3}\Big|_{t_i} + \mathcal{O}(\Delta t^2) \quad (\text{B.16})$$

where $\eta_i = \eta\Big|_{t_i}$, because we begin from a known value.

Substituting this into equation (B.14), using the original differential equation (B.9) to write the second derivative as $-\omega^2\eta$, we get:

$$(B.14) = \frac{d^2\eta}{dt^2} - \omega^2\Delta t \frac{d\eta}{dt} + \omega^2\eta + \mathcal{O}(\Delta t^2) \quad (\text{B.17})$$

In which we recognize the differential equation of a 'negatively' damped oscillator (see figure B.1). This approximation introduces a oscillation source. The approximation of the undamped oscillator is not accurate. The negative damping coefficient means that the amplitude of oscillation always will increase. No matter which Δt or ω we choose, the oscillator will be unstable. We can show this by another simple method, determining the stability of numeric approximations: the von Neumann method.

Stability: von Neumann's method

We start from initial, known situation at $t = t_0$, which we call η_0 . The method states that every step forward in time introduces an error in the form of a complex factor z :

$$\eta_n = z^n \eta_0 \quad (\text{B.18})$$

When this behaviour is substituted into a discrete approximation of the differential equation, we can solve for the factor z . The method is said to be stable if $\|z\| \leq 1$. The module of z is called the amplification factor.

When we apply this on the explicit approximation, we get:

$$z^2 - 2z + 1 = -\omega^2\Delta t^2 \quad (\text{B.19})$$

For determination of stability we regard only the module of z .

We solve for z , which gives:

$$z = 1 \pm i\omega\Delta t \quad (\text{B.20})$$

of which the module is always greater than 1, whatever ω or Δt might be. The explicit schedule is **unconditionally unstable**.

Implicit schedule

Here we change the discretised equations slightly. To be precise: we change the indices of the right member of both equations of (B.13). We apply the 'backward' or implicit approximation:

$$\begin{aligned} \frac{\eta_{i+1} - \eta_i}{\Delta t} &= \dot{\eta}_{i+1} \\ \frac{\dot{\eta}_{i+1} - \dot{\eta}_i}{\Delta t} &= -\omega^2\eta_{i+1} \end{aligned} \quad (\text{B.21})$$

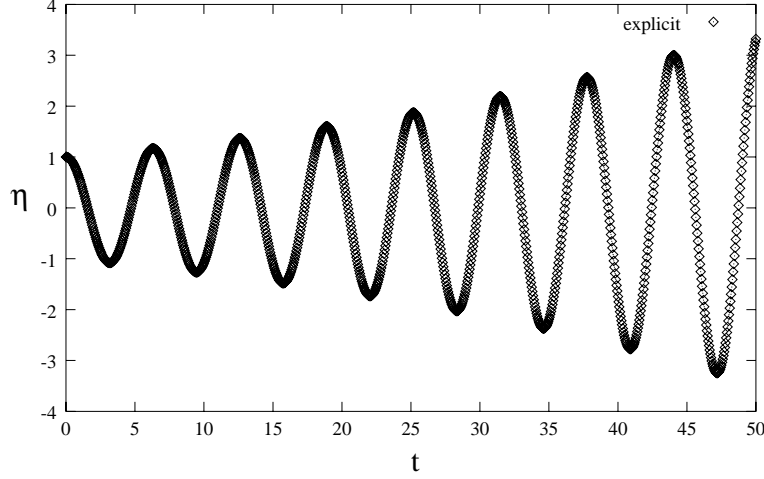


Figure B.1: The result of the explicit schedule.

When we substitute the first equation into the second one, we obtain:

$$\frac{\eta_{i+1} - 2\eta_i + \eta_{i-1}}{\Delta t^2} + \omega^2 \eta_{i+1} = 0 \quad (\text{B.22})$$

Not surprisingly, again this is not exactly correct. We express η_{i-1} in a Taylor series about ($t = t_i$):

$$\eta_{i-1} = \eta \Big|_{t_i} - \Delta t \frac{d\eta}{dt} \Big|_{t_i} + \frac{1}{2} \Delta t^2 \frac{d^2\eta}{dt^2} \Big|_{t_i} - \frac{1}{6} \Delta t^3 \frac{d^3\eta}{dt^3} \Big|_{t_i} + \mathcal{O}(\Delta t^4) \quad (\text{B.23})$$

If we use this, together with (B.15), to trace the error between the exact and discretised derivatives, we see the term with Δt (which appears in eq. (B.17)) disappear (in fact all odd-powered terms disappear). When we take a larger number of terms in the Taylor development, we obtain:

$$\frac{\eta_{i+1} - 2\eta_i + \eta_{i-1}}{\Delta t^2} = \frac{d^2\eta}{dt^2} \Big|_{t_i} + \frac{1}{12} \Delta t^2 \frac{\partial^4\eta}{\partial t^4} \Big|_{t_i} + \mathcal{O}(\Delta t^4) \quad (\text{B.24})$$

We substitute this into equation (B.22), and we write out the Taylor series for $\omega^2 \eta_{i+1}$. Using (B.9) again, this gives:

$$(B.22) = \frac{\partial^2\eta}{\partial t^2} + \omega^2 \Delta t \frac{\partial\eta}{\partial t} + \omega^2 \eta + \mathcal{O}(\Delta t^2) \quad (\text{B.25})$$

Notice the $+$ sign in front of the second term in the right member. This schedule solves in fact the differential equation of a damped oscillator (see figure B.2).

Applying von Neumann's method in order to determine the stability, gives:

$$(1 + \omega^2 \Delta t^2) z^2 - z + 1 = 0 \quad (\text{B.26})$$

which has solutions:

$$z = \frac{1 \pm i\sqrt{3 + 4\omega^2 \Delta t^2}}{2(1 + \omega^2 \Delta t^2)} \quad (\text{B.27})$$

The squared norm of this complex number is:

$$|z|^2 = \frac{1}{1 + \omega^2 \Delta t^2} \quad (\text{B.28})$$

Since $\omega^2 \Delta t^2$ is always positive, the implicit approximation is **unconditionally stable**, but it is damped out.

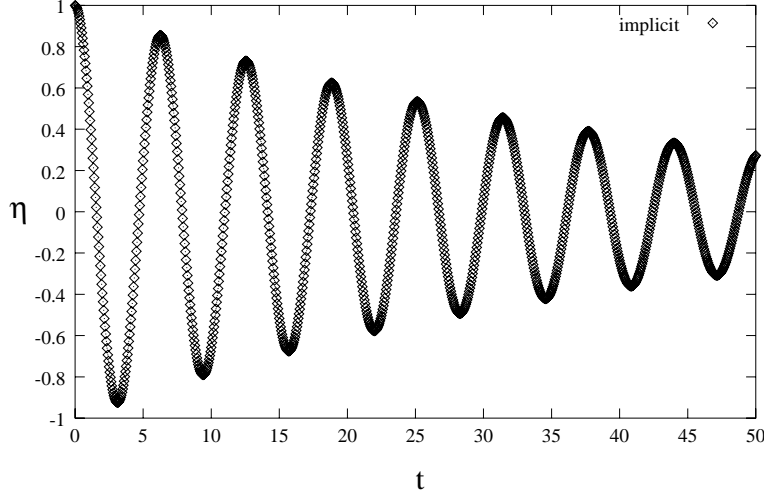


Figure B.2: The result of the implicit schedule.

Partly implicit schedule

In reference to the explicit schedule, we now only change the index of the right member of the second equation in (B.13):

$$\begin{aligned} \frac{\eta_{i+1} - \eta_i}{\Delta t} &= \dot{\eta}_i \\ \frac{\dot{\eta}_{i+1} - \dot{\eta}_i}{\Delta t} &= -\omega^2 \eta_{i+1} \end{aligned} \quad (\text{B.29})$$

This gives the combined schedule:

$$\frac{\eta_{i+2} - 2\eta_{i+1} + \eta_i}{\Delta t^2} + \omega^2 \eta_{i+1} = 0 \quad (\text{B.30})$$

Using the Taylor expansions again, we obtain the differential equation:

$$(B.30) = \frac{\partial^2 \eta}{\partial t^2} + \omega^2 \left(1 + \frac{\omega^2 \Delta t^2}{12} \right) \eta + \mathcal{O}(\Delta t^3) \quad (\text{B.31})$$

This schedule solves the differential equation of an oscillator with a slightly perturbed frequency (in order Δt^2). If we also write out the perturbation of order Δt^3 we obtain the result:

$$(B.30) = \frac{\partial^2 \eta}{\partial t^2} + \frac{\omega^4}{40} \Delta t^3 \frac{\partial \eta}{\partial t} + \omega^2 \left(1 + \frac{\omega^2 \Delta t^2}{12} \right) \eta + \mathcal{O}(\Delta t^4) \quad (\text{B.32})$$

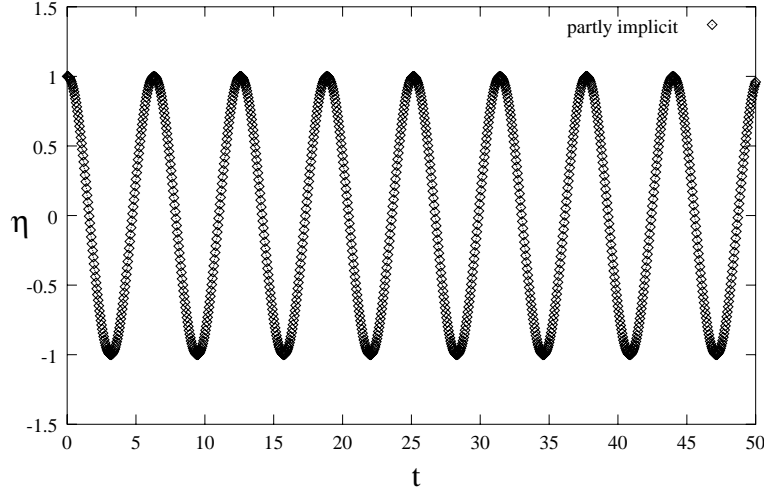


Figure B.3: The result of the partly implicit schedule.

Again, a damping term has appeared in the equation, but now in third order of Δt .

The von Neumann method gives the equation:

$$z^2 - 2z + 1 = -\omega^2 \Delta t^2 z \quad (\text{B.33})$$

which has two roots:

$$z = 1 - \frac{\omega^2 \Delta t^2}{2} \pm \frac{\omega^2 \Delta t^2}{2} \sqrt{\omega^2 \Delta t^2 - 4} \quad (\text{B.34})$$

there are three different cases to be examined (note that $\omega \Delta t$ is positive):

- $\omega \Delta t < 2$: both roots are complex. In this case the module is:

$$\|z\| = 1 \quad (\text{B.35})$$

and thus stable

- $\omega \Delta t = 2$. In this case the module of the roots is:

$$\|z\| = \left| 1 - \frac{\omega^2 \Delta t^2}{2} \right| = 1 \quad (\text{B.36})$$

again stable

- $\omega \Delta t > 2$: both roots are real, they are:

$$z = 1 - \frac{\omega^2 \Delta t^2}{2} \pm \frac{\omega^2 \Delta t^2}{2} \sqrt{\omega^2 \Delta t^2 - 4} \quad (\text{B.37})$$

the module of root '+' is smaller than 1 since $\sqrt{x^2 - 4} < x$ for $x > 2$. But the root '-' is less than -1 for $\omega \Delta t > 2$, and thus unstable.

We conclude that this schedule is **stable** under assumption that $\omega \Delta t < 2$. In figure B.4 the effect of choosing Δt beyond the stability condition is shown, the solution is unstable.

A somewhat more complex and more general method of discretisation is the so-called Newmark's method. This method is explained below. This method uses parameters which allow to choose the accuracy of approximation. The advantage of this is that we can obtain very accurate and very stable numerical solutions with it. The Newmark method is also described in [7, Ch7]

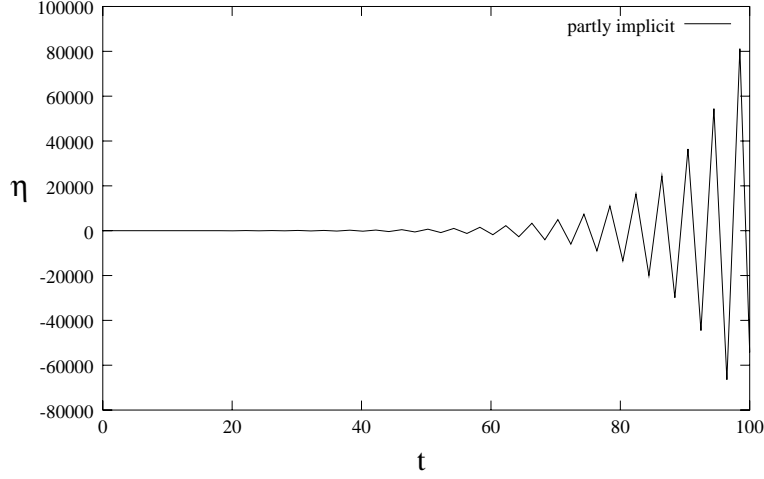


Figure B.4: The solution of the partly implicit schedule, with $\omega = 1$ and $\Delta t = 2.01$.

B.1.2 The Newmark approximation

For the solution of the equation of movement, we calculate the state of the system at time t_{n+1} as a function of the known state in the previous step t_n . This state is the vector $(\eta, \dot{\eta})_n$. We develop the new state of the system in terms of the previous, known state, by a Taylor series conform equations (B.2) and (B.3) from appendix B. We can write this development in the following form:

$$\dot{\eta}_{n+1} = \dot{\eta}_n + \int_{t_n}^{t_{n+1}} \ddot{\eta}(\tau) d\tau \quad (\text{B.38})$$

$$\eta_{n+1} = \eta_n + \Delta t \dot{\eta}_n + \int_{t_n}^{t_{n+1}} (t_{n+1} - \tau) \ddot{\eta}(\tau) d\tau \quad (\text{B.39})$$

which is thus the exact solution. The normal straightforward explicit method in B.1.1 takes 0 for the two integrals and neglects a lot of information. Newmark's method has its significance in approximation of these two integrals, by writing out $\ddot{\eta}(\tau)$ in terms of the acceleration at time t_n and t_{n+1} .

In order to do that, we develop $\ddot{\eta}_{n+1}$ in a Taylor series at time τ in the interval $[t_n, t_{n+1}]$:

$$\ddot{\eta}_n = \ddot{\eta}(\tau) + \eta^{(3)}(\tau) (t_n - \tau) + \eta^{(4)}(\tau) \frac{(t_n - \tau)^2}{2} + \dots \quad (\text{B.40})$$

$$\ddot{\eta}_{n+1} = \ddot{\eta}(\tau) + \eta^{(3)}(\tau) (t_{n+1} - \tau) + \eta^{(4)}(\tau) \frac{(t_{n+1} - \tau)^2}{2} + \dots \quad (\text{B.41})$$

We multiply these equations by $(1 - \gamma)$ and by γ , respectively. Adding the two gives for $\ddot{\eta}(\tau)$ the formula:

$$\ddot{\eta}(\tau) = (1 - \gamma)\ddot{\eta}_n + \gamma\ddot{\eta}_{n+1} + \eta^{(3)}(\tau) (\tau - \Delta t\gamma - t_n) + \mathcal{O}(\Delta t^2 \eta^{(4)}) \quad (\text{B.42})$$

We repeat this, but now we multiply by $(1 - 2\beta)$ and by 2β , respectively:

$$\ddot{\eta}(\tau) = (1 - 2\beta)\ddot{\eta}_n + 2\beta\ddot{\eta}_{n+1} + \eta^{(3)}(\tau) (\tau - 2\Delta t\beta - t_n) + \mathcal{O}(\Delta t^2 \eta^{(4)}) \quad (\text{B.43})$$

Next, we substitute (B.42) in (B.38) and (B.43) in the equation for η_{n+1} (B.39). This gives for the integrals:

$$\int_{t_n}^{t_{n+1}} \ddot{\eta}(\tau) d\tau = (1 - \gamma) \Delta t \ddot{\eta}_n + \gamma \Delta t \ddot{\eta}_{n+1} + r_\gamma \quad (\text{B.44})$$

$$\int_{t_n}^{t_{n+1}} (t_{n+1} - \tau) \ddot{\eta}(\tau) d\tau = \left(\frac{1}{2} - \beta \right) \Delta t^2 \ddot{\eta}_n + \beta \Delta t^2 \ddot{\eta}_{n+1} + r_\beta \quad (\text{B.45})$$

where the errors are as follows:

$$r_\gamma = \left(\gamma - \frac{1}{2} \right) \Delta t^2 \eta^{(3)}(\tau') + \mathcal{O}(\Delta t^3 \eta^{(4)}) \quad (\text{B.46})$$

$$r_\beta = \left(\beta - \frac{1}{6} \right) \Delta t^3 \eta^{(3)}(\tau') + \mathcal{O}(\Delta t^4 \eta^{(4)}) \quad (\text{B.47})$$

with $t_n < \tau' < t_{n+1}$.

The constants γ and β are parameters which are free to choose. As a function of these two parameters we produce different approximations of $\ddot{\eta}(\tau)$.

Substitution of (B.44) and (B.45) in the formulas (B.38) respectively (B.39), gives the approximations of Newmark's method:

$$\dot{\eta}_{n+1} = \dot{\eta}_n + (1 - \gamma) \Delta t \ddot{\eta}_n + \gamma \Delta t \ddot{\eta}_{n+1} \quad (\text{B.48})$$

$$\eta_{n+1} = \eta_n + \Delta t \dot{\eta}_n + \left(\frac{1}{2} - \beta \right) \Delta t^2 \ddot{\eta}_n + \beta \Delta t^2 \ddot{\eta}_{n+1} \quad (\text{B.49})$$

The solution of this system is not straightforward, since in the position and the velocity of the equation above the acceleration is included implicitly (at time t_{n+1}). We solve this system by a prediction-correction method which is explained in chapter D.2.

B.2 Solving a system of linear equations

A very quick way of solving a system of linear equations is the method of factorization. We give a set of linear equations, written in the form:

$$\mathbf{A} \mathbf{f} = \mathbf{b} \quad (\text{B.50})$$

where \mathbf{A} is a tridiagonal matrix $N \times N$, \mathbf{f} is a vector of unknowns and \mathbf{b} is a given vector.

It is a recursive method of 'sweeping' the tridiagonal matrix. The system of equations can be written in the form:

$$\begin{aligned} A_{i,i-1} f_{i-1} + A_{i,i} f_i + A_{i,i+1} f_{i+1} &= c_i \quad 1 \leq i \leq N-1 \\ f_0 &= F_0 \quad f_N = F_N \end{aligned} \quad (\text{B.51})$$

the latter are known constants. More conveniently, we will denote the terms in the upper diagonal with u_i , the main diagonal with m_i and the lower with l_i . Keeping the index of the current row, this puts the equation in the form:

$$l_i f_{i-1} + m_i f_i + u_i f_{i+1} = c_i \quad 1 \leq i \leq N-1 \quad (\text{B.52})$$

For this system a recurrence relation exists:

$$f_i = X_i f_{i+1} + Y_i \quad i = 1, \dots, N-1 \quad (\text{B.53})$$

The coefficients X_i and Y_i can be found by substituting (B.53), applied on i_1 , in equation (B.52) and solve it for f_i :

$$m_i f_i = c_i - u_i f_{i+1} - l_i (X_{i-1} f_i + Y_{i-1}) \quad (\text{B.54})$$

Putting this equation in the form of (B.53) we recognize the coefficients:

$$X_i = \frac{-u_i}{m_i + l_i X_{i-1}} \quad Y_i = \frac{c_i - l_i Y_{i-1}}{m_i + l_i X_{i-1}} \quad i = 1, \dots, N - 1 \quad (\text{B.55})$$

The coefficients X_0 and Y_0 can be determined as follows. We solve equation (B.52) with $i = 1$ for f_1 , in the form of (B.53):

$$f_1 = -\frac{u_1}{m_1} f_2 + \frac{c_1 - l_1 F_0}{m_1} \quad (\text{B.56})$$

Comparing this to (B.55), with $i = 1$, we can identify:

$$X_0 = 0 \quad Y_0 = F_0 \quad (\text{B.57})$$

The method is applied by first calculating X_i and Y_i for $i = 1, \dots, N - 1$ with (B.55). Then we take (B.53) to solve f_i from $N - 1$ down to 1.

For further reading, [18] and [10] are interesting books on numerical methods.

Appendix C

Stability of RNS-p(x) simulation

In this section we present an experimental study of the stability of the simulation programs for steady channel and jet flow.

The stability of the channel flow simulation program is studied by varying the pace dx and dy and regarding the results. The study is carried out on a specific part of the flue channel, namely the diverging part at the end of the channel. In the divergence the flow separates from the wall and causes back-flow. This is an effect which provokes unwanted oscillations and divergence of the solution.

For the nondimensionalised variable x , the equation of the channel wall is written as follows:

$$\begin{aligned} H &= 1 - \alpha Re x & \text{for } 0 \leq x \leq \frac{1}{2\alpha Re} \\ H &= \frac{1}{2} + \beta \alpha Re x & \text{for } x \geq \frac{1}{2\alpha Re} \end{aligned} \quad (\text{C.1})$$

Here the length of the channel L has the value $70/hRe_h$, with $h = 1\text{mm}$ because we regard only half the channel. In the equation above is α the angle of convergence and β the ratio of divergence and convergence. For the real flue channel as depicted in figure 2.1 these parameters are: $\alpha = 0.00357$ and $\beta = 35$. In the study presented below, the factor β has been varied also.

C.0.1 Channel flow

We will change the step-size of both variables for the case $\beta = 10$ (nothing special; just an intermediate value), and see what happens. We will set the longitudinal step-size to $dx = 0.001$ and calculate the shear stress curve for different dy displayed figure C.1. From this figure we can see that the curves calculated for values of dy up to one hundredth are well on top of each other. For higher values instabilities occur.

Now, we will vary dx for a given value of dy , which is set to 0.005. The results are shown in figure C.2. Here the calculations are consistent for $dx \lesssim 0.001$. It is clear that the critical values of dx and dy , above which instabilities occur, depend on β . The greater this parameter, the more points we need in calculation.

This is illustrated by figure C.3, where for each β we used a rough grid of calculation and a grid with a hundred times as many points (ten times in both directions). For $\beta = 2$ both wall shear stress curves are practically the same. But for larger β this similarity diminishes.

Now, we shall try to find the roughest grid which allows us to calculate the wall shear stress curve in the diverging part of the actual flue channel ($\beta = 35$). In figure C.4 we display this search. We

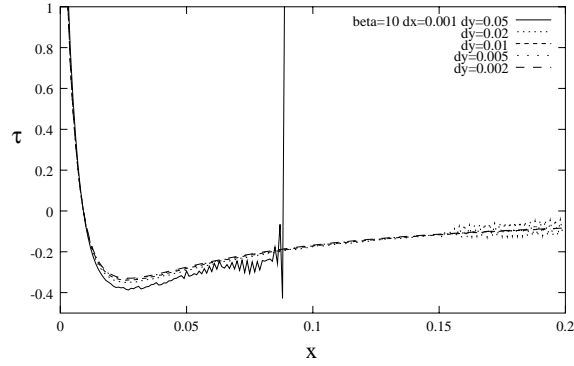


Figure C.1: The wall shear stress as a function of x , for different steps in transversal direction.

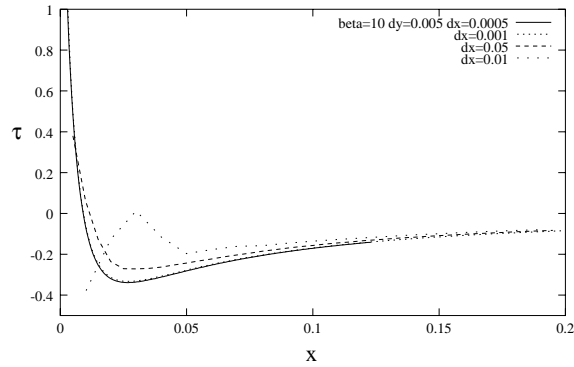


Figure C.2: The wall shear stress as a function of x , for different steps in longitudinal direction.

start from a very fine grid and first increase the step-size dx . We see that for $dx \leq 0.0002$ the curves are very close to one another, so we take $dx = 0.0002$. Now, we increase dy for fixed dx and we can see the wall shear stress function begins to oscillate when $dy = 0.02$, the solution becomes divergent.

Taking $dx = 0.0002$ and $dy = 0.02$ we have approximately the roughest grid in which we can calculate the shear stress curve smoothly. For the Reynolds number chosen ($Re = 853.2$) the flue channel has a nondimensionalised length of $L \simeq 1.7$. This means that we have to have 850 points in longitudinal direction. Usually in such a case the best thing to do in order to decrease the time needed for calculation is to separate the different parts of the channel (the converging and the diverging part). For the converging section we can apply a rougher grid, because the slower things change the less points we have to use (see figure C.3). Nevertheless, the program which solves the reduced Navier Stokes equations is fast enough to use the finest needed grid throughout the whole channel.

In figure C.5 the wall shear stress curve, calculated with the new grid, is displayed. The curve is smooth now, and we can determine the calculated point of separation of both methods. We can do this using the output files of the programs, interpolating the point of separation between the calculated points in front and behind. This gives $x^* = 70.3\text{mm}$ for method 1. and $x^* = 70.6\text{mm}$ for method 2..

C.0.2 Plane jet

The stability of the jet flow simulation has been studied by varying the step-sizes and numbers of points in the domain and observe its influence on several quantities. In section 2.2.1 it is

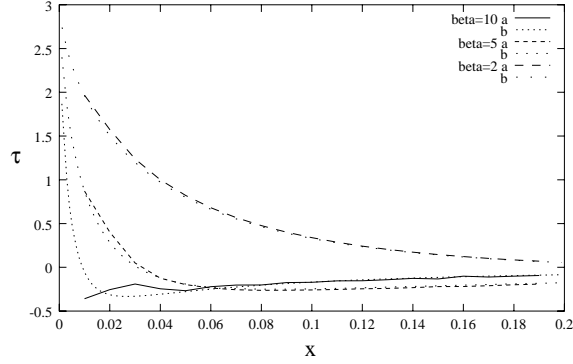


Figure C.3: The wall shear stress as a function of x , for different values of β . For each β two curves are calculated: one with $dx = 0.01$ and $dy = 0.05$ which bears the letter 'a', and the others with $dx = 0.001$ and $dy = 0.005$, indicated with 'b'.

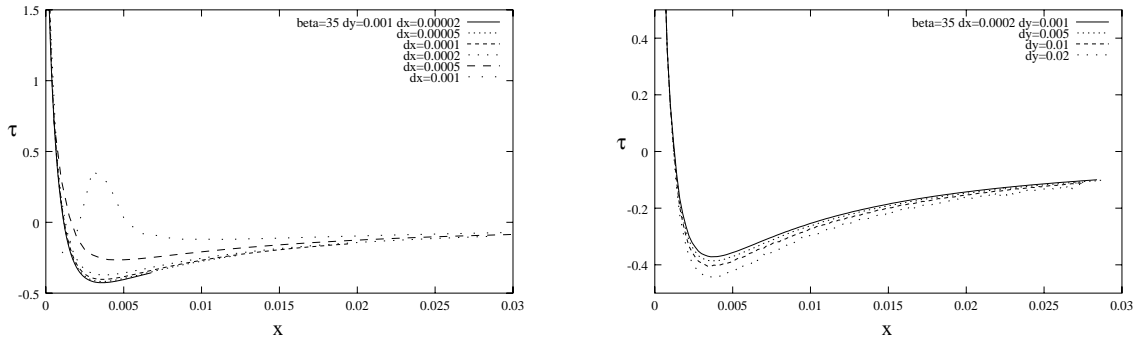


Figure C.4: The wall shear stress as a function of x , for $\beta = 35$ and different step-sizes in both x (left) and y (right) direction.

shown that in the model of jet flow the momentum flux is conserved and also that the quantity $u(du/dx)^{-1}$ decreases as $-3x$. We will follow these quantities in our search.

For all the calculations in this section, we started with arbitrary velocity profiles coming from the channel simulation. The profiles are shown in figure C.6.

We begin with an investigation of the transverse domain. By varying the number of points n_y , keeping the rest constant ($dx = 0.01$, $n_x = 200$ and $dy = 0.1$). In figure C.7 the influence of variation of n_y on the momentum flux and the velocity profiles is shown. Looking at the longitudinal velocity profiles in that figure we can say that if the transverse domain is smaller than the profile itself, the solution is no longer accurate.

Next take $n_y = 250$, $dy = 0.1$ and increase the step-size dx . In figure C.8 we can see its influence on the momentum flux and the quantity $u(du/dx)^{-1}$.

From these figures it can be seen that the momentum flux becomes less accurate and it even oscillates for $dx = 0.1$. The quantity $u(du/dx)^{-1}$ is even more sensitive for dx . The value oscillates about the correct solution for $dx = 0.05$, and becomes divergent for larger dx .

Let's see what increasing the transverse domain for the worst case above ($dx = 0.1$) will change. In figure C.9 again the momentum flux and $u(du/dx)^{-1}$ are shown. From that we can see a taking a twice as big transverse domain has improved the results downstream, but for small x the solution is not very accurate. The upstream parts of the two curves are the same, independent of the choice of n_y , whereas further downstream they differ. In figure C.10 the longitudinal velocity profile of these two cases are shown.

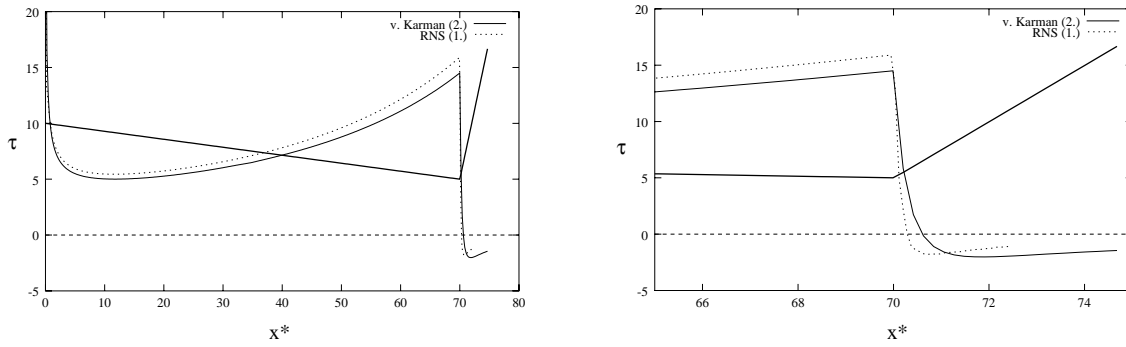


Figure C.5: The wall shear stress as a function of x^* . The curve 'RNS' is calculated with the new grid. In the right figure we zoomed in on the separation point.

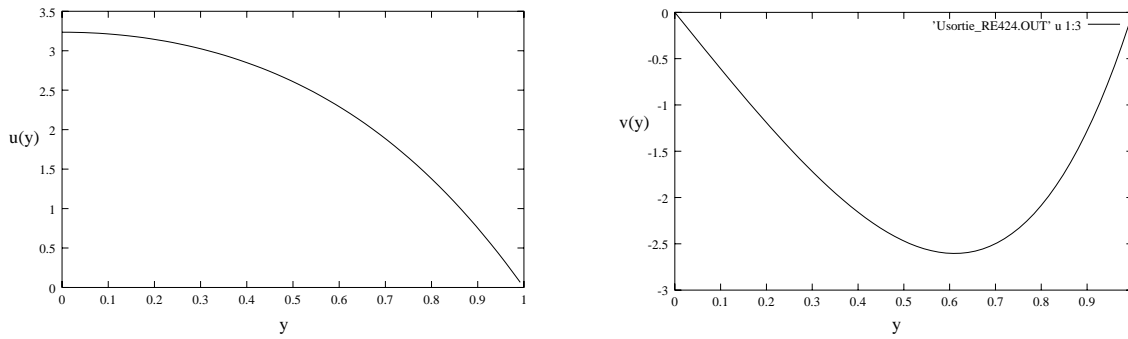


Figure C.6: The longitudinal (left) and transverse (right) velocity profiles, taken as entry for the jet simulation

At $y = 0$ we observe oscillations. Here the effect of taking different transverse domains is very clear. Forcing the profile to fit in that domain causes the solution to get less accurate.

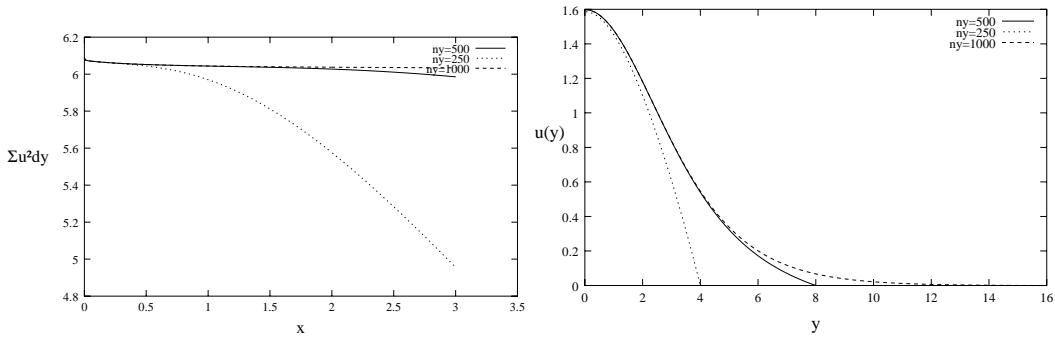


Figure C.7: The momentum flux (left) as a function of x and the profile $u(y)$ at $x = 2$ for different n_y .

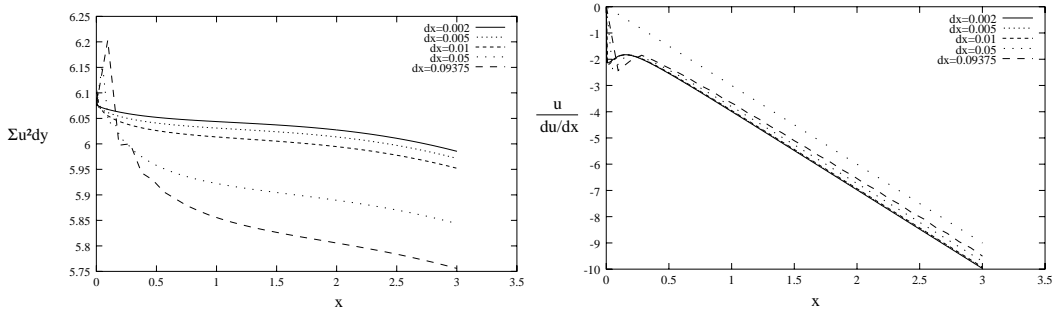


Figure C.8: The momentum flux (left) and $u(du/dx)^{-1}$ as a function of x for different dx .

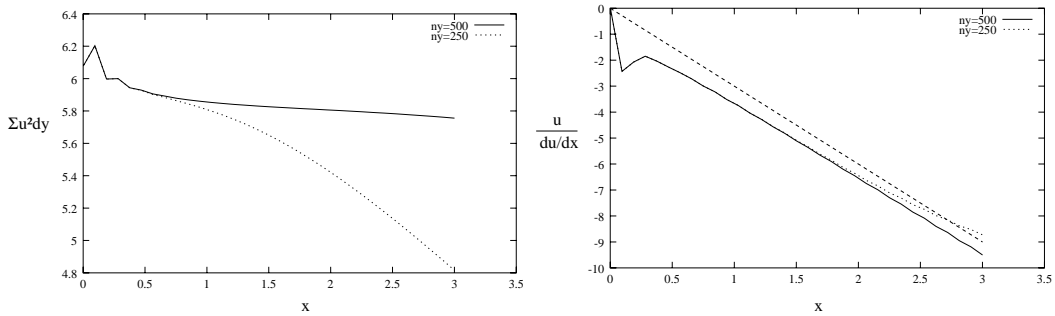


Figure C.9: The momentum flux (left) and $u(du/dx)^{-1}$ as a function of x for two different n_y . Here $dx = 0.1$

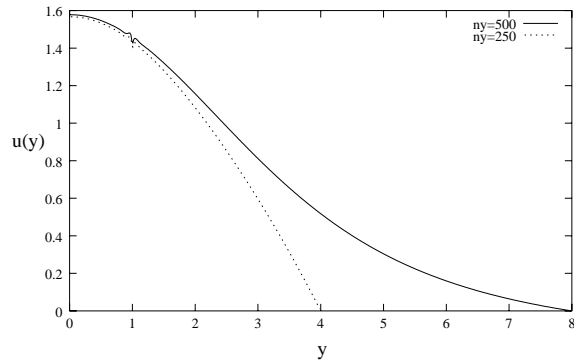


Figure C.10: The profile $u(y)$ at $x = 20 (=n_x \times dx)$ for two different values of n_y .

Appendix D

Solution of a membrane model

In this chapter we present the general model of the membrane motion. The model we use in this report for the vocal folds is a simple, particular case of this model. In the first section we present the equation of motion.

In section D.2 we present the numerical solution of this problem: the Newmark method. This method has a special approximation of the equation of motion and has the advantage that it is unconditionally stable.

D.1 The membrane model

For the elastic part of the wall we apply a membrane. Since we only regard the fluid in 2 dimensions, this membrane will be a one dimensional membrane. This membrane has a mass density of m , a longitudinal tension of S and it is suspended in a rigid frame with springs of strength k and dampers with damping constant c (see figure D.1). We shall assume small deformations only in vertical direction. The displacement of the membrane η is a function of the longitudinal coordinate

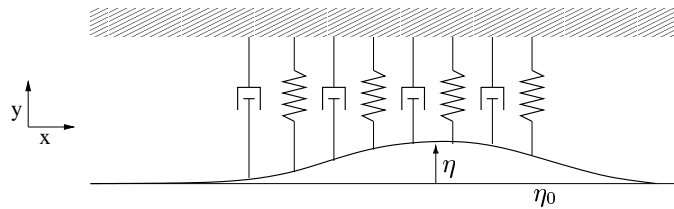


Figure D.1: The model for the motion of the membrane.

x , and is defined in the positive y direction.

Writing the mechanical equilibrium gives:

$$m \frac{\partial^2}{\partial t^2} \eta(t, x) + b \frac{\partial}{\partial t} \eta(t, x) + k \eta(t, x) - S \frac{\partial^2}{\partial x^2} \eta(t, x) = F(t, x) \quad (\text{D.1})$$

where F is an external force applied on the membrane in the positive y direction.

In the model of the membrane we do not nondimensionalise the terms, because we like to have the liberty to choose its mechanical behaviour at will, i.e. choose the parameters m , b , k and S .

The membrane is suspended between its two ends at $x = 0$ and $x = L_m$. Thus the boundary conditions of this problem are:

$$\eta(t, 0) = \eta(t, L_m) = 0 \quad (\text{D.2})$$

which represent two fixed points in space. We permit the membrane to turn about these points, for this instant.

Since we have second order differential equation with respect to time as well, we need two initial conditions:

$$\eta(0, x) = \eta_0 \quad (\text{D.3})$$

$$\frac{\partial}{\partial t}\eta(0, x) = \dot{\eta}_0 \quad (\text{D.4})$$

We permit a lot of liberty to decide the boundary and initial conditions.

D.1.1 Solutions

The solutions are as well known as its problem. We will highlight some of them for simple verification with the simulation. In all cases we will assume the absence of external forces.

Free membrane: $b = k = 0$

Here we will show the solution of the differential equation of a membrane which has no springs nor dampers attached to it. The equation of motion is the wave equation:

$$m \frac{\partial^2}{\partial t^2} \eta(t, x) = S \frac{\partial^2}{\partial x^2} \eta(t, x) \quad (\text{D.5})$$

with the boundary and initial conditions conform the previous section. The general solution is:

$$\eta(t, x) = A e^{i(kx - \omega t)} + B e^{i(kx + \omega t)} \quad (\text{D.6})$$

where $S/m = k^2/\omega^2$. Taking the boundary condition into account, we obtain the solution:

$$\eta(t, x) = \eta_0 \sin(k_n x) e^{i\omega_n t + \phi} \quad (\text{D.7})$$

with $k_n = n\pi/L_m$ and ω related to it conform the expression above, the phase factor ϕ is determined by the initial conditions.

In figure D.2 an example is shown. It displays the movement of an elastic membrane, held between two fixed points at $x = 0$ and $x = 10$. We took $m = S = 1$ and half a period and a full period of a sine function as initial condition. The former case shows an oscillation of the membrane with $\omega = \pi/10$, and oscillates twice as fast.

Chain of uncoupled springs

The other solution we examine is the simple mass-spring equation. In this case we assume absence of longitudinal tension. We leave out the damping as well. In absence of the tension there is no coupling in longitudinal direction, so each point moves separately according to the equation of mechanical equilibrium:

$$m \frac{\partial^2}{\partial t^2} \eta(t) + k \eta(t) = 0 \quad (\text{D.8})$$

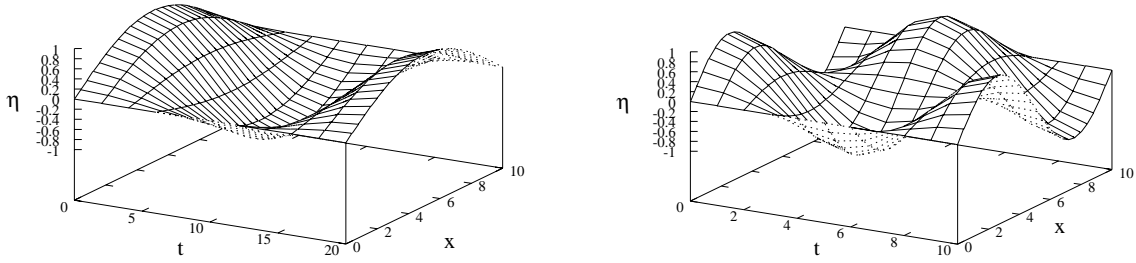


Figure D.2: The displacement of the membrane as a function of t and x , for two different initial conditions: half a period (left) and a whole period between the fixed ends. Here $m = S = 1$ is chosen.

with initial condition (D.3). The solutions of this equation is:

$$\eta(t) = \eta_0 \cos(\omega t) + \frac{\dot{\eta}_0}{\omega} \sin(\omega t) \quad (\text{D.9})$$

where $\omega = \sqrt{k/m}$, the famous harmonic oscillator.

Now we add the damping term b . The solution is then.

$$\eta(t) = \eta_0 \exp\left(\frac{-b \pm \sqrt{b^2 - 4km}}{2m} t\right) \quad (\text{D.10})$$

the damped mass-spring system. The critical damping factor is the one for which the exponent passes from real to complex, has value $b = 2\sqrt{mk}$.

In figure D.3 an example of a non-damped and critically damped oscillator is given.

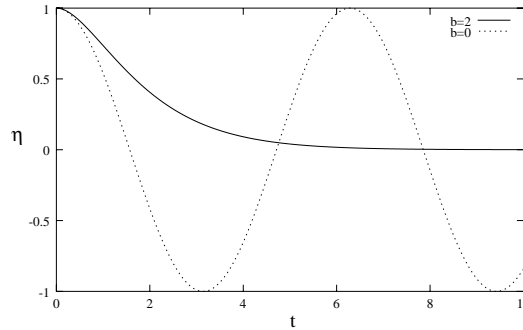


Figure D.3: The displacement of the undamped and critically damped mass spring system. For both cases $m = k = 1$ is chosen.

D.2 Numerical method

D.2.1 Discretisation

simple: $\eta_j^n = \eta(t = t_n, x = x_j)$ which we solve for every pace in time. For the discretisation of the equation of mechanical equilibrium, we have chosen the so-called Newmark's method. This method is a one step integration method, like the other methods. The method is generalised with the aid of parameters, which permits to 'place' the approximation of the derivatives. It is explained briefly in appendix B.

D.2.2 Newmark's method

For solution of the equation of motion (D.1) we substitute $\eta(x)$ in Newmark's discretisation method. The second derivative with respect to x will be centered in j :

$$\frac{\partial^2}{\partial x^2} \eta(t = t_n, x) \rightarrow \frac{\eta_{j+1}^n - 2\eta_j^n + \eta_{j-1}^n}{\Delta x^2} \quad (\text{D.11})$$

When we put the x dependence into vector notation, the equation of motion writes:

$$\mathbf{M}\ddot{\boldsymbol{\eta}} + \mathbf{C}\dot{\boldsymbol{\eta}} + \mathbf{K}\boldsymbol{\eta} = \mathbf{F} \quad (\text{D.12})$$

where all coefficients are written as matrices. The matrices \mathbf{M} , \mathbf{C} and \mathbf{K} are diagonal matrices containing respectively the mass density, the damping coefficient and the spring constant on the diagonals. The matrix \mathbf{S} is a tridiagonal matrix representing (D.11), with $-2S/\Delta x^2$ on the principal diagonal and $S/\Delta x^2$ on the two diagonals just above and below the principal.

D.2.3 Solution

As explained in appendix B the Newmark approximations of the displacement and the velocity can be written as:

$$\dot{\eta}^{n+1} = \dot{\eta}^n + (1 - \gamma)\Delta t\ddot{\eta}^n + \gamma\Delta t\ddot{\eta}^{n+1} \quad (\text{D.13})$$

$$\eta^{n+1} = \eta^n + \Delta t\dot{\eta}^n + \left(\frac{1}{2} - \beta\right)\Delta t^2\ddot{\eta}^n + \beta\Delta t^2\ddot{\eta}^{n+1} \quad (\text{D.14})$$

Substituting these approximations into the equation of motion (D.12), and writing this out at the instant $t = t_{n+1}$:

$$\begin{aligned} & (\mathbf{M} + \gamma\Delta t\mathbf{C} + \beta\Delta t^2(\mathbf{K} - \mathbf{S}))\ddot{\boldsymbol{\eta}}^{n+1} = \\ & \mathbf{f}^{n+1} - \mathbf{C}(\dot{\boldsymbol{\eta}}^n + (1 - \gamma)\Delta t\ddot{\boldsymbol{\eta}}^n) - (\mathbf{K} - \mathbf{S})\left(\boldsymbol{\eta}^n + \Delta t\dot{\boldsymbol{\eta}}^n + \left(\frac{1}{2} - \beta\right)\Delta t^2\ddot{\boldsymbol{\eta}}^n\right) \end{aligned} \quad (\text{D.15})$$

Which is the convenient form with all known terms on the right hand side, all unknown on the left hand side. Except for the external force. This force is implicitly defined and has to be known at fore-hand.

The solution of Newmark's method is somewhat different from other one-step integration methods, because of the added corrective terms in the approximations of the displacement and the velocity. A method of prediction and correction will be used which will be explained in the following.

Departing from a known state of the system at time t_n the solution goes as follows.

prediction

First we predict the values of the displacement and velocity of the membrane using the state at instant t_n :

$$\dot{\eta}_*^{n+1} = \dot{\eta}^n + (1 - \gamma)\Delta t\ddot{\eta}^n \quad (\text{D.16})$$

$$\eta_*^{n+1} = \eta^n + \Delta t\dot{\eta}^n + \left(\frac{1}{2} - \beta\right)\Delta t^2\ddot{\eta}^n \quad (\text{D.17})$$

calculation of $\ddot{\eta}^{n+1}$

With the estimated displacement and velocity, we can calculate the acceleration at instant t_{n+1} , using equation (D.15). This equation is of the form which we can solve by inverting the matrix appearing in front of $\ddot{\eta}^{n+1}$ by the method of factorization.

correction

After that we correct the displacement and the velocity using the the acceleration term just calculated:

$$\dot{\eta}^{n+1} = \dot{\eta}_*^{n+1} + \gamma \Delta t \ddot{\eta}^{n+1} \quad (\text{D.18})$$

$$\eta^{n+1} = \eta_*^{n+1} + \beta \Delta t^2 \ddot{\eta}^{n+1} \quad (\text{D.19})$$

Once we have corrected, we can advance in time. The flowchart explaining this method graphically, is shown in figure E.3

To see how well this method works we investigate a bit the accuracy and stability of Newmark's method.

D.2.4 Accuracy

In [7, Ch7] an elaborate discussion of the accuracy and stability is given. We will not repeat this here.

We give a rather qualitative derivation of the error in the periodicity made in case the parameters as chosen $\gamma = 0.5$ and $\beta = 0.25$. With the results of the harmonic oscillator we can derive this error of periodicity. If the harmonic oscillator with period T is solved, the solution of Newmark's method has period $T + \Delta T$. The frequency has the relation $\omega = 2\pi/T$ with the period. So, the solution will be an oscillation with frequency

$$\omega_c = \frac{2\pi}{T} \left(\frac{1}{1 + \Delta T} \right) \quad (\text{D.20})$$

where the index c indicates it is the solution of the calculation. The error gives in first order approximation:

$$\omega_c = \omega \left(1 - \frac{\Delta T}{T} \right) \quad (\text{D.21})$$

where ω is the exact frequency (the one we should have). The solution is thus of the form:

$$\eta(t) = \cos(\omega_c t) = \cos\left(\omega t \left(1 - \frac{\Delta T}{T}\right)\right) \quad (\text{D.22})$$

We will visualize the error in order to verify. We subtract the analytical solution from the numeric solution:

$$\cos(\omega_c t) - \cos(\omega t) = \cos\left(\omega t - \frac{\Delta T}{T} \omega t\right) - \cos(\omega t) \quad (\text{D.23})$$

In order to bring the error forward we apply trigonometric rules for cosine:

$$\cos\left(\frac{a-b}{2}\right) = \cos\frac{a}{2} \cos\frac{b}{2} + \sin\frac{a}{2} \sin\frac{b}{2} \quad (\text{D.24})$$

$$\cos\left(\frac{a+b}{2}\right) = \cos\frac{a}{2} \cos\frac{b}{2} - \sin\frac{a}{2} \sin\frac{b}{2} \quad (\text{D.25})$$

Subtracting the latter from the former gives

$$\cos\left(\frac{a-b}{2}\right) - \cos\left(\frac{a+b}{2}\right) = 2 \sin\frac{a}{2} \sin\frac{b}{2} \quad (\text{D.26})$$

In reference to (D.23) we identify

$$a = 2\omega t \left(1 - \frac{\Delta T}{T}\right) b = \frac{\Delta T}{T} \omega t \quad (\text{D.27})$$

Now, the difference between the analytical and numerical solutions can be written as

$$2 \sin\left(\frac{2 - \Delta T/T}{2} \omega t\right) \sin\left(\frac{\Delta T \omega t}{2T}\right) \quad (\text{D.28})$$

the first sine oscillates very rapidly, whereas the second varies slowly. The error in periodicity produces an envelope with amplitude 2 of the rapidly varying function. The frequency of the envelope is

$$\frac{\Delta T \omega}{2T} = \frac{\omega^3 \Delta t^2}{24} \quad (\text{D.29})$$

The error is plotted in figure D.4 and D.5. From the first two figures it can be seen that for higher ω the frequency of the envelope function is less accurately represented by formula (D.29), because we neglected the higher order terms in the determination of this frequency. Those terms become more important for higher frequencies.

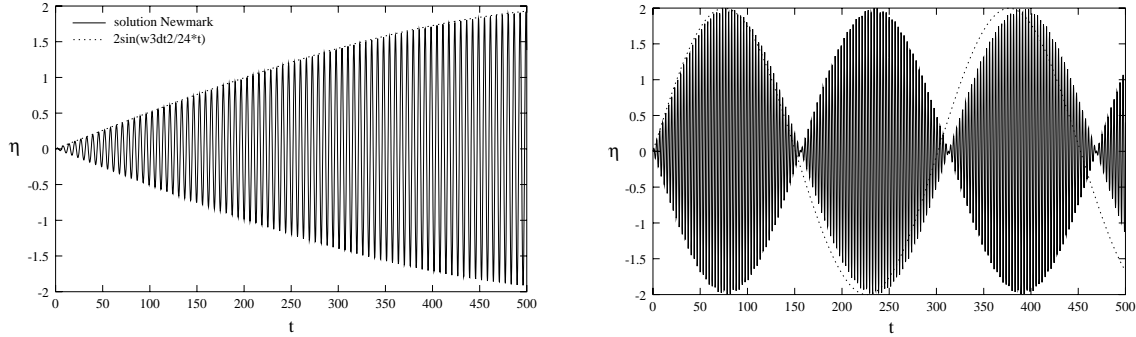


Figure D.4: The error in periodicity from the Newmark method, solving the equation (D.8) with $m = k = 1$ (left) and $k = 4$ (right), both have $\Delta t = 0.25$. The frequency of the envelope function represents the error conform (D.28). Neglect of higher order terms in the error causes the misfit in the right figure, where those terms are more important while the frequency is greater.

By decreasing the time step-size, the error is more precisely determined. And the error in periodicity has decreased with factor 4 ($\sim \Delta t^2$).

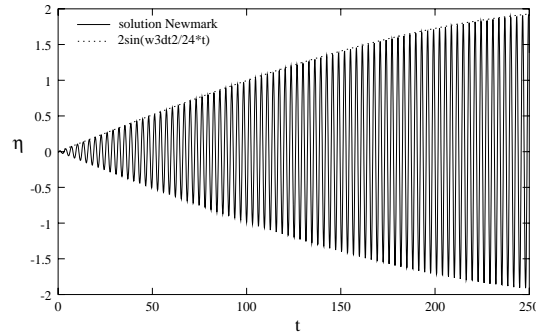


Figure D.5: The error in the periodicity conform (D.28) for the case $m = 1$, $k = 4$, for $\Delta t = 0.125$.

D.2.5 Stability

On the stability of the damped and undamped mass-spring system an elaborate discussion can be found in [7]. As a function of the two parameters γ and β the accuracy and stability is studied by the method of von Neumann. The conclusion is that for the case $\gamma = 1/2$ and $\beta = 1/4$ the method is unconditionally stable. There is, however, an error in the periodicity, which is derived in the previous section:

$$\frac{\Delta T}{T} = \frac{\omega^2 \Delta t^2}{12} + \mathcal{O}(\Delta t^3) \quad (\text{D.30})$$

where T is the period of oscillation. Since the whole numeric approximation formulas contain a lot of terms, a thorough analytical study of stability will be rather complicated. In appendix B.1.2 we discuss the error in the periodicity in the solution via Newmark's method applied on the mass-spring system.

Appendix E

Flowcharts

In this section the flowcharts of the steady channel flow simulation, the steady jet simulation and the Newmark method for the membrane simulation are presented.

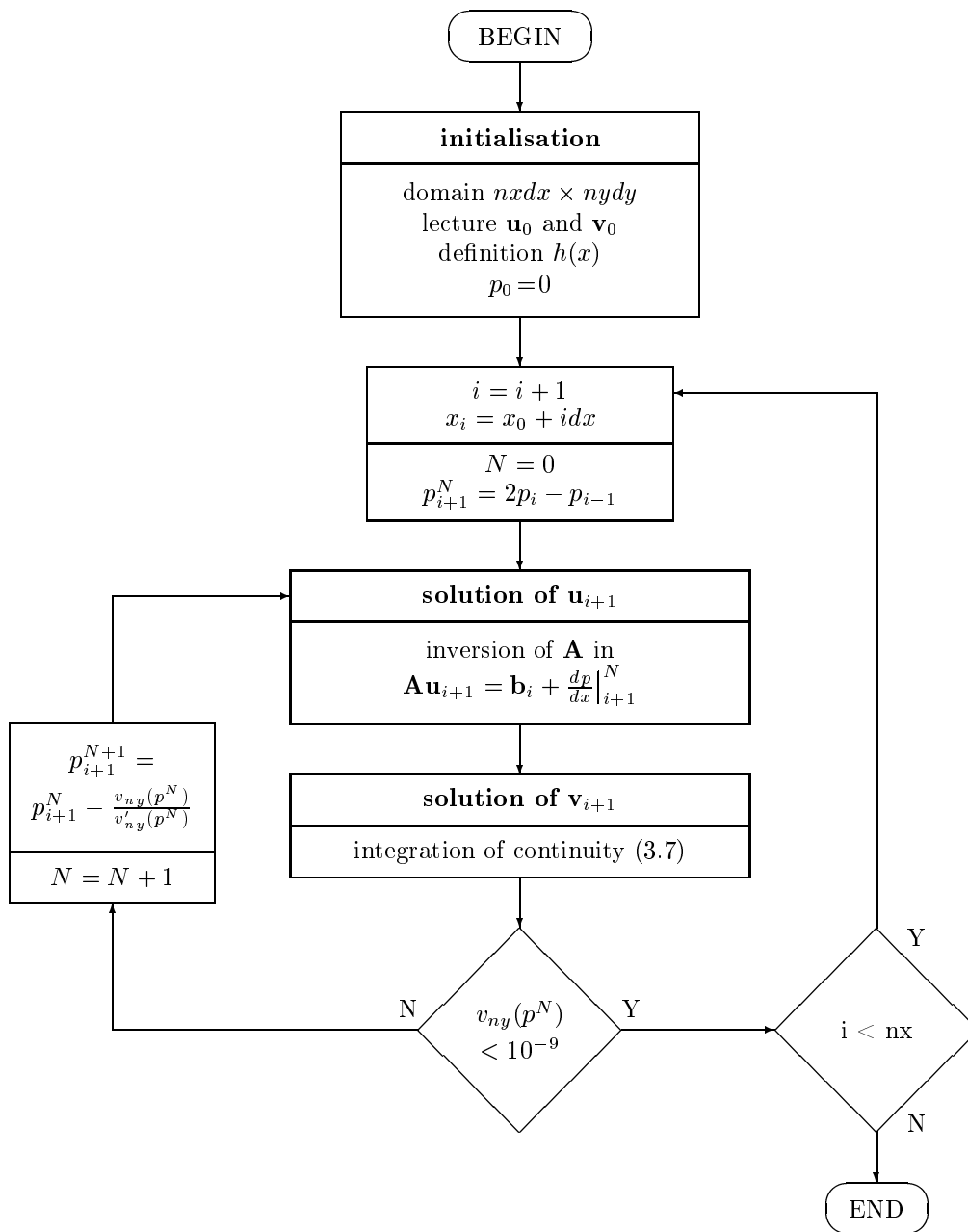


Figure E.1: The flowchart of the steady channel flow simulation.

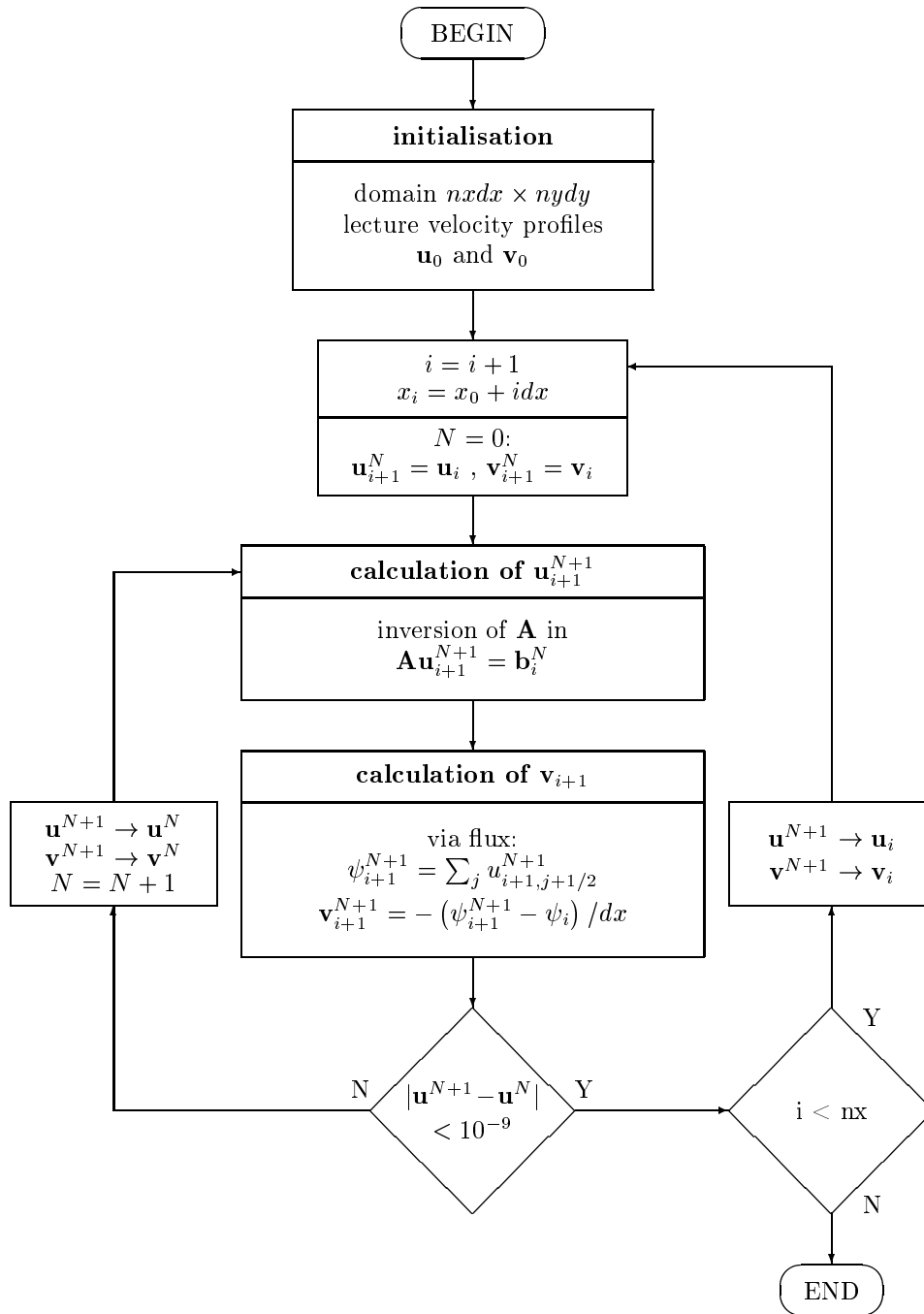


Figure E.2: The flowchart of the steady jet flow simulation.

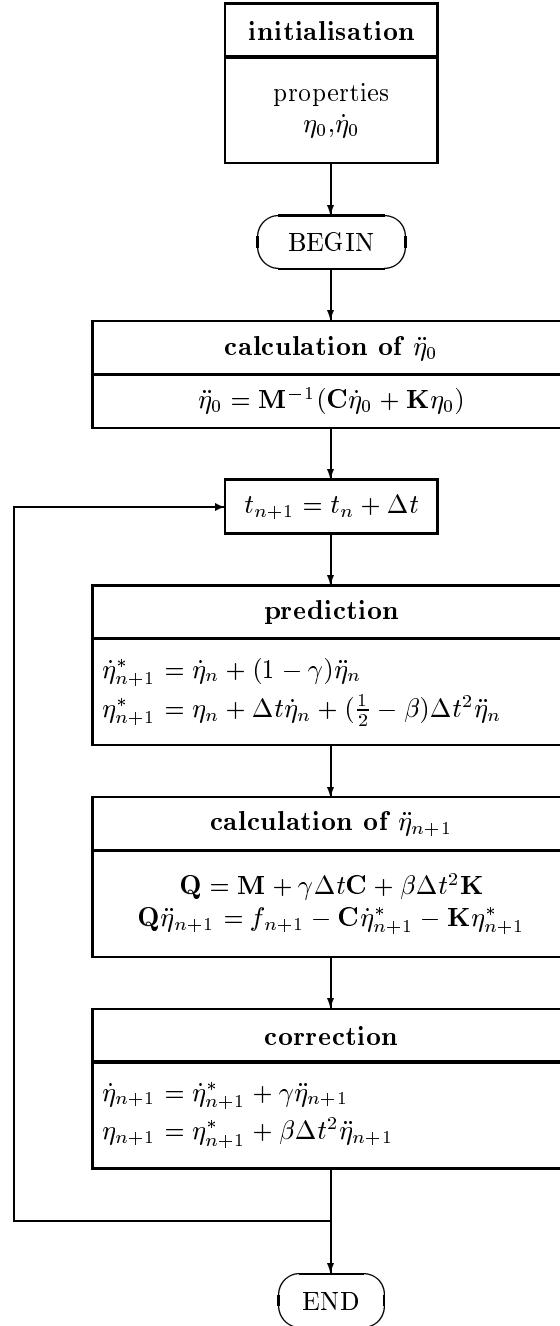


Figure E.3: The flowchart of the Newmark method for simulation of the membrane.